Title
Gamma-ray Mapping

Author
Pavlovsky, Ryan Thomas

Publication Date
2017

Peer reviewed|Thesis/dissertation

Gamma-ray Mapping

by

Ryan Thomas Pavlovsky

A dissertation submitted in partial satisfaction of the

requirements for the degree of

Doctor of Philosophy

in

Engineering - Nuclear Engineering

in the

Graduate Division

of the

University of California, Berkeley

Committee in charge:

Kai Vetter, Chair
Eric Norman
Jasmina Vujic
Robert Jacobsen

Summer 2017

Gamma-ray Mapping

Abstract

Gamma-ray Mapping

by

Ryan Thomas Pavlovsky

Doctor of Philosophy in Engineering - Nuclear Engineering

University of California, Berkeley

Kai Vetter, Chair

Advanced radiation detector sensors and detector systems have promoted the idea of Gamma-Ray Mapping, the fusion of maps generated by contextual sensors with radiation data. Gamma-Ray Mapping seeks to discover sources or distributions of radioactive isotopes in the mapped measurement environment. As this suggests, there are two components to a Gamma-Ray Mapping system: the map generation and Gamma-Ray imagers. This concept has been motivated heavily by the availability of advanced gamma-ray detectors as well as commercial sensors such as Global Positioning System (GPS), Light Imaging, Detection and Ranging (LIDAR), Inertial Measurement Unit (IMU), etc., which can facilitate Simultaneous Localization and Mapping (SLAM).

The role of Compton Imagers for Gamma-Ray Mapping has been explored for some time [3][20][12]. These systems have good angular resolution, however they suffer from imaging ambiguities in the Compton cones and require an ensemble of gamma-ray events to reconstruct the source location. Electron Track Compton Imagers (ETCI) seek to break the symmetry of Compton cones and eventually approach event-by-event gamma-ray momentum computation. Additionally, these detectors provide the possibility of new imaging modalities that rely only on electron tracks to recover the angular location and energy of a source [19]. ETCI has been shown to be conceptually possible [60] in high resolution 10.5 μm Super Novae Acceleration Probe (SNAP) Charge Coupled Device (CCD) silicon detectors. However, there are many practical issues with the implementation of CCD detectors as Compton imagers, namely that time resolution in these devices is conservatively the Frame Read Time (FRT). In typical SNAP devices the FRT can be $\sim$ 1 s/MPxl. The lack of time resolution limits the use of CCD electron trackers in Compton imagers as well as in other radiation detector system uses.

In order to circumvent the limit established by the FRT, CCD-strip was proposed. CCD-strip devices conceptually provide time resolution on the order of the electron drift time in n-type CCD detectors by application of strip segmentation to the CCD backside. Time stamps would be correlated through the coarse strip spatial coding and the high resolution electron tracks in the CCD pixel plane. Backside strips imply that double-sided, micrometer

alignment would be required for CCD-strip fabrication. Significant effort was required in the coordination of the CCD fabrication facility Teledyne DALSA and strip detector fabrication facility SINTEF. A small batch of CCD-strip devices were fabricated and tested in the Lawrence Berkeley National Laboratory (LBNL) engineering test stand for screening purposes. The bulk of this work's contribution is in the construction and demonstration of the newly fabricated devices in a custom test stand. The DALSA control wafers were the first of this batch to produce electron tracks, and the device was characterized in our testbed. The custom cryostat and measurement stand allowed us to reduce the leakage current in CCD-Strip by a factor of 1000. The reduction removed voltage transients with equivalent charge of about 3-5 MeV at the output of the preamplifiers. Ultimately the output baseline had an Equivalent Noise Charge (ENC) of 400 keV-RMS per strip. The magnitude of the ENC is large enough that strip operation is yet to be demonstrated.

Benchmarked simulations for the improvement of electron tracking and imaging algorithms are also presented. From these simulations follows an investigation of the nuclear scattering effect in electron trackers. Nuclear scattering is an important design consideration for electron trackers as it scrambles the Compton kinematic information without producing ionization, or signal, in electron trackers. From an examination of the nuclear scatter limit, diamond was identified as a very interesting detector material for electron tracking. Diamond is a material that minimizes nuclear scattering while maintaining photon efficiency. This boosts the amount of ionization signal obtained from the initial portion of the electron track. Electron-nuclear scattering is a large source of kinematic information loss in ETCI systems.

Beyond complex detectors, augmentation of monolithic sensors with contextual sensors to provide SLAM has been investigated for Gamma-Ray Mapping. Given the many types of instruments which may be of interest, we constructed Localization and Mapping Platform (LAMP), a data collection and demonstration platform for detectors and contextual sensors. Here we used Google Cartographer as a SLAM solution. SLAM provides the 6 Degrees of Freedom (DOF) trajectory of a system, while simultaneously generating 3D models. These allow for ranging of gamma-ray emitters and the correction of detector responses to provide better association of flux with physical objects. We demonstrated handheld and Unmanned Aerial System (UAS) measurements as configurations for making these measurements. LAMP, in handheld and flight configurations, provides a portable, robust indoor and outdoor 3D SLAM solution for Gamma-Ray Mapping. LAMP was fitted with commercial radiation detectors as a proof of concept. The radiation and scene data can be fused by utilization of the SLAM output poses, trajectory and 3D model with simple backprojection. The 3D backprojection scheme demonstrated incorporates simulated detector angular responses for better resolution of hotspots than just backprojection alone. LAMP has demonstrated that there is utility in coupling contextual sensors to augment simple commercial detectors. Implementations that use commercial radiation detectors are important to Gamma-Ray Mapping in that they represent the low end of the cost versus complexity for mapping. We also demonstrate uses where GPS is either insufficient in function or accuracy. LAMP will serve in the future as a demonstration platform for many kinds of detectors.

The development of ETCI and LAMP systems continues to expand the Gamma-Ray Mapping application space. The developments in complex Gamma-Ray Imagers, coupled with contextual platforms, consider the necessary components for Gamma-Ray Mapping. This work has presents progress toward understanding the applicability and information that ETCI systems provide, and we note that there is substantial work to be done toward the goal of mapping with ETCI devices. The LAMP demonstration platform is crucial to comparing technologies and understanding the complex problems that Gamma-Ray Mapping poses. These parallel developments both share a part in enabling Gamma-Ray Mapping.

To Lana and my family.

Contents

Acronyms

ADC Analog to Digital Converter

AI Artificial Intelligence

APD Avalanche Photodiode

API Application Programming Interface

ARC Astronomical Research Cameras

BEGe Broad Energy Germanium

CCD Charge Coupled Device

CCDs Charge Coupled Devices

CCI Compact Compton Imager

CDS Correlated Double Sampling

CME Coronal Mass Ejection

CMOS Complementary Metal-Oxide Semiconductor

COA Certificates of Waiver or Authorization

COMPTEL The Imaging COMPton TELescope

COSI Compton Spectrometer and Imager

CSA Charge Sensitive Preamplifier

CSDA Constant Slowing-Down Approximation

DALSA Teledyne DALSA

DOE Department of Energy

DOF Degrees of Freedom

DSP Digital Signal Processor

EMI Electromagnetic Interference

ENC Equivalent Noise Charge

ESD Electrostatic Discharge

ETCI Electron Track Compton Imagers

FAA Federal Aviation Administration

FDNPPA Fukushima Dai-ichi Nuclear Power Plant Accident

FEM Finite Element

FIFO First In First Out

FPGA Field Programmable Gate Array

FRT Frame Read Time

FWHM Full Width Half Max

GBP Gain-Bandwidth Product

GEANT4 Generation of Events ANd Tracks

GPS Global Positioning System

GRIPS Gamma-Ray Imaging Polarimetry/Spectroscopy for Solar Flares

HEMI High Efficiency Multimodal Imager

HPGe High Purity Germanium

HSB Heat Spreader Bar

ICP Iterative Closest Point

IFB Interface Board

IMU Inertial Measurement Unit

INS Inertial Navigation System

IP Intellectual Property

IR Infrared

JAEA Japan Atomic Energy Agency

JFET Junction Field Effect Transistor

LAMP Localization and Mapping Platform

LBNL Lawrence Berkeley National Laboratory

LIDAR Light Imaging, Detection and Ranging

MCNP Monte Carlo N-Particle

METI Japanese Ministry of Economy, Trade and Industry

MLEM Maximum-Likelihood Expectation Maximization

NCT Nuclear Compton Telescope

NEXT Neutrino Experiment with Xenon TPC

NNSA National Nuclear Security Administration

NORM Naturally Occurring Radioactive Material

PFB Picture Frame Board

RMS Root Mean Square

ROS Robot Operating System

SCFM Standard Cubic Feet Per Minute

SEM Scanning Electron Microscopy

SINTEF SINTEF Research

SIT Static Induction Transistor

SLAM Simultaneous Localization and Mapping

SNAP Super Novae Acceleration Probe

SOIPIX SOI Pixel Detector Project

SOI Silicon On Insulator

UART Universal Asynchronous Receiver/Transmitter

UAS Unmanned Aerial System

VCI Volumetric Compton Imager

WHO World Health Organization

Chapter 1

Introduction

Radiation detectors have many uses in scientific, industrial and security applications. Non-proliferation, source search, consequence management, nuclear power disaster contamination mapping, medical imaging, astrophysics and many others fall into the context where one might desire radioisotope mapping. The measurements at the heart of these applications vary in implementation, however they all seek to deduce information about radioisotopes in spatial and/or time dimensions. These data can either be the binary detection of a specific radioisotope or map a distribution of a specific radioisotope. Therefore it is convenient to choose radiation detectors that are sensitive to particles that could be observed from standoff distances of greater than 1 m or so, but still have highly specific and reasonable information rates in the measurement. Gamma-Rays, or photons emitted from certain nuclear level transitions in radioisotopes, provide a highly specific monoenergetic stimulus to gamma-ray detectors. The stimulus provokes a signature by which gamma-ray emitting isotopes can be identified and quantified. Radiation detectors that can identify and quantify gamma-ray emitters are called spectrometers. One or many nuclear level transitions may be used for identification. These detected emissions from the nuclear level transitions are always convolved with the detector response, resulting from the interaction physics. Detector responses are more complicated than just the collection of measured monoenergetic emissions. For example, Figure 1.1 shows the response of a high resolution gamma-ray spectrometer. Here the spectrometer is used to identify two isotopes of the same chemical species from a radiological release. The presence of ^{134}Cs is highly specific to Uranium based reactor operation, while ^{137}Cs can be related to Uranium based reactor releases or nuclear weapons. In this way, the presence or absence of these isotopes can help to understand the origin of radioactive releases. The idea, that the origin of radioisotope releases can be discovered by their presence or absence, is critical in the field of nuclear forensics.

The presence of gamma-ray emitters can be attributed to anthropogenic, cosmogenic and primordial origins. In most cases, radioisotopes that are cosmogenic and primordial in origin establish a limit of sensitivity or detectability for measurements which do not explicitly intend to measure them. Collectively known as Naturally Occurring Radioactive Material (NORM), these radioisotopes and their daughters are sometimes referred to as

background radiation[1]. Background radiation can vary based on weather, geologic location and the materials in the measurement scenario. Figure 1.2 and Figure 1.3 provide examples of NORM and man-made radioisotopes from an air sampler. Here the gamma-ray signatures are fairly complicated, even in a high performance gamma-ray spectrometer. The magnitude of count rate variations can be quite large over 1 hr intervals. Figure 1.3 shows factors of 15 for ^{214}Bi from the maximum count rate to the minimum. The variations observed here from a stationary detector are partially explained by local weather and climate patterns. The complexity of the scenario is quite expansive, even in this relatively simple case.

Gamma-Ray Mapping seeks to either find discrete sized sources or distributions of sources over the measurement backgrounds. Design of radiation detector systems for these purposes considers the application, the measurement background, the limits in detector and electronic performance and the limits of physical information provided by gamma-rays.

For meter scale mapping the most common tool of choice is similar to surveys like Figure 1.4. Figure 1.4 shows a map of the interior of a home affected by the Fukushima Dai-ichi Nuclear Power Plant Accident (FDNPPA) in Namie, Japan. The survey was the first re-entry of this home since the disaster, 4.75 years later. Mapping is achieved by a two person team with Geiger and NaI dose rate probes with the dose rates noted at each location. The aggregation of the data is left somewhat to the experimentalist as one must infer hotspots from integrated flux measurements at discrete points.

The method shown by Figure 1.4 logistically simple, however it requires a trained operator for the proper use of an instrument, data must be taken and aggregated by hand and can require the operator to be the first line-of-defense in the inspection of any newly surveyed area. Especially in the case where doses may not be known, first re-entry by humans to collect measurements presents a risk and information tradeoff. Ideally a system for Gamma-Ray Mapping would remove common error modes in data collection, be more robust in usage, provide realtime feedback and allow data to be collected without risking operator safety.

1.1 Imaging Technologies

Gamma-Ray imagers are specialized radiation detectors designed to exploit gamma-ray interaction physics to provide localization capabilities for Gamma-Ray Mapping. The detectors that implement gamma-ray imagers differ considerably. Proximity imagers are often the simplest gamma-ray imagers providing localization from distance-based source intensity modulation. Detectors employed are monolithic or pixelated, and additional modulation from the detector orientation and positioning can be included in specific cases. Many examples of proximity imagers exist and fundamentally work on similar principles to the modulations observed in Figure 1.4. Prominent results of Proximity Imaging are the Department of Energy (DOE)/National Nuclear Security Administration (NNSA)-JAEA's emergency re-

[1]In the general context, the term background is often extended to refer to isotopes which are part of a measurement that does not seek to measure them.

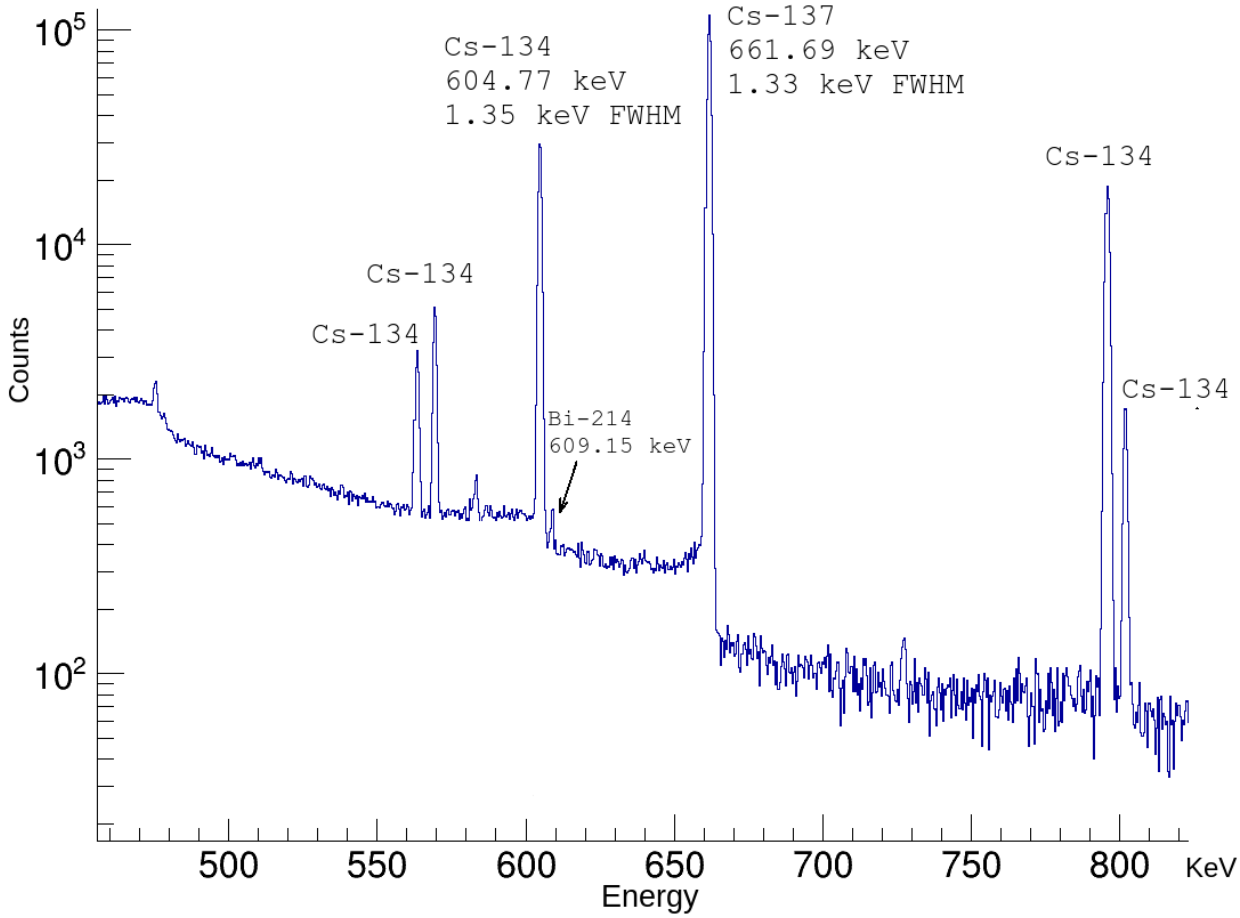

Figure 1.1: Nondestructive assay for identification of isotopes by their gamma-ray signatures with a 15 % High Purity Germanium (HPGe). The isotopes in this sample are embedded in soil due to their chemical properties. In particular the ^{137}Cs and ^{134}Cs lines are important for nuclear forensics as ^{134}Cs is produced in significant quantities in reactors but not directly by fission as per tables provided by England [13]. Sample collected from Namie, Japan in December 2015 inside the exclusion zone 4.75 yrs after the FDNPPA. The isotopes seen here were part of the radioactive releases.

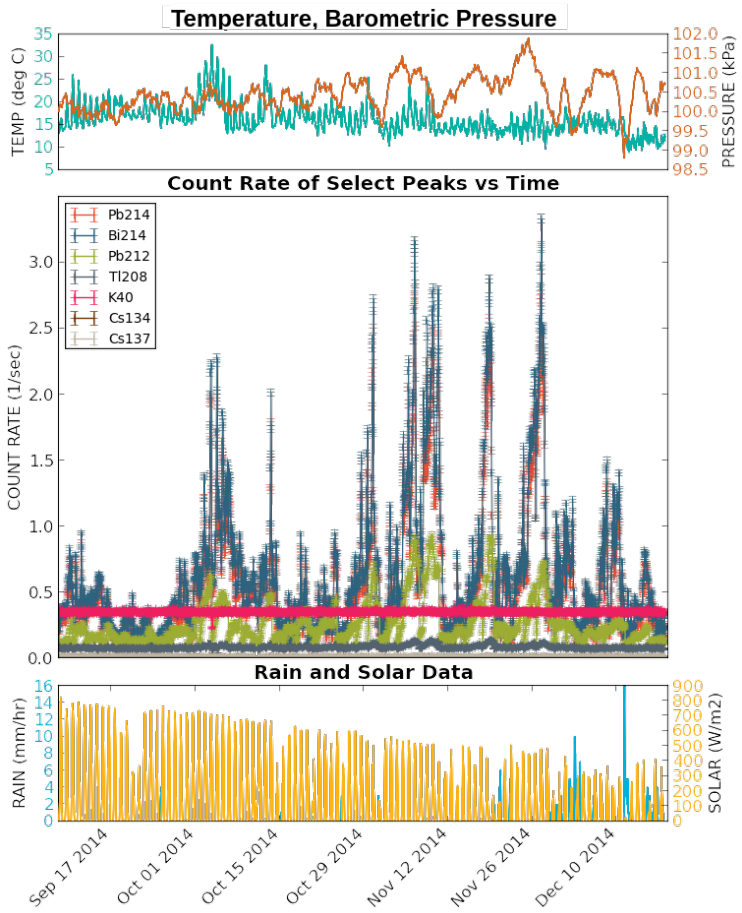

Figure 1.2: Naturally Occurring Radioactive Material (NORM) from the Near Realtime Air Sampler versus time. The variations observed are related to Radon and Thoron decay chains. Data were collected with a mechanically cooled, thin window, N-type Broad Energy Germanium (BEGe) detector. Radioisotopes are collected by air sampling at 21 Standard Cubic Feet Per Minute (SCFM) onto an 4" FPAE-102 HEPA filter about 2 inches from the detector thin window. Temperature, barometric pressure, differential rain at 1 hr increments and solar flux are reported. Weather data correspond to the axis labels which share the line color.

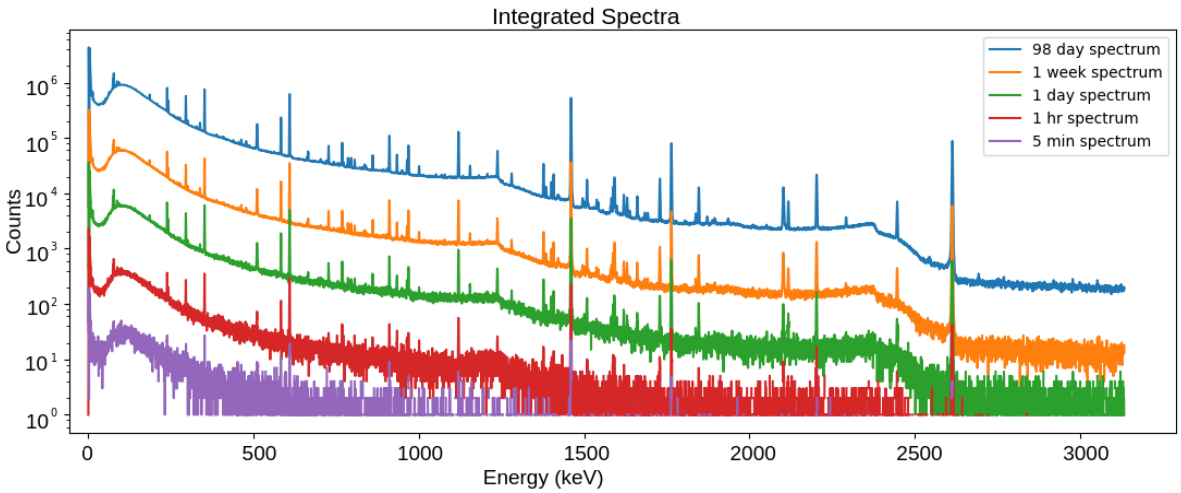

Figure 1.3: Raw air monitor spectra from Figure 1.2 over selected time intervals. One or many peaks correspond to one of the different Naturally Occurring Radioactive Material (NORM)/man-made isotopes that establish backgrounds for many gamma-ray measurements.

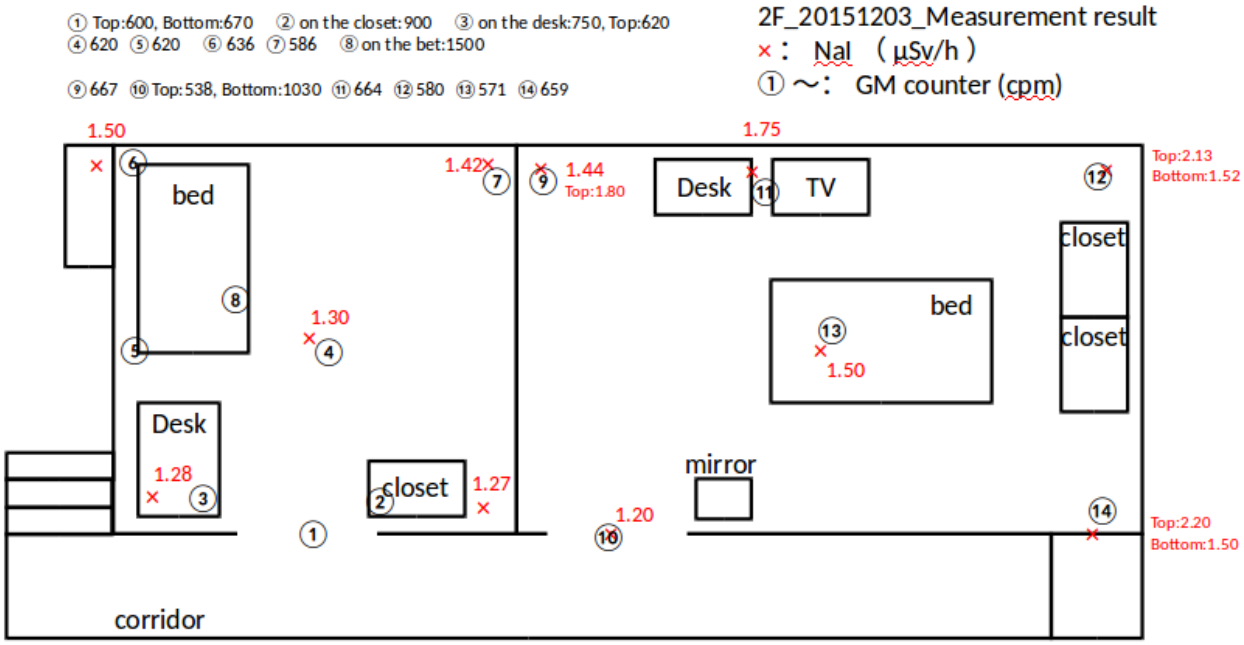

Figure 1.4: Japan Atomic Energy Agency (JAEA) map of a home within the Fukushima exclusion zone. After the Fukushima Dai-ichi reactors volatilized the radioactive inventory, mapping is required to allow residents to return. The map above is an example of the current tool of choice for investigating potentially contaminated areas indoors. Simple measurements are made with both a NaI dosimeter and Geiger counter. The selection of measurement areas is done by walk-throughs with a dose-rate meter. Areas that are of interest are counted for longer periods of time, and sample swipes are taken.

sponse maps of radioactive contamination from the Fukushima Dai-ichi Nuclear Power Plant Disaster [52]. This example is discussed at length in Chapter 5.

Another type of gamma-ray imager is the Compton Imager. Detectors capable of Compton Imaging must supply at least one or many of: position, energy or time resolution. Measurements must provide some or all of these data to pair Compton scatter and absorption events from the same photon. COMPTEL [12] was an example of a Compton Imager based on monolithic scintillators to map the distribution of ^{26}Al in the galaxy. ^{26}Al is important to ongoing nucleosynthesis and is of importance to cosmology. Segmented detectors have also been used as Compton Imagers. For example, Si and HPGe orthogonal strip semiconductor detectors have been used as gamma-ray imagers, providing spatial coding of about 0.5-10 mm on a single crystal. At least two interactions from the same photon are required for operation in Compton mode. Of the two interactions one should be a scattering event and one should fully absorb. Time coincidences and energy pairing allows for the generation of Compton cones identification of events from a single photon. Compton cones are possible incident gamma-ray directions, which result from Compton scatter kinematics and kinematic ambiguity. With an ensemble of cones, measurements provide the angular source position by coherent summing in a discrete angular space. The large volume, high energy resolution and spatial coding make orthogonal strip detectors suited for many Compton Imaging applications. For example Nuclear Compton Telescope (NCT) [29] and Gamma-Ray Imaging Polarimetry/Spectroscopy for Solar Flares (GRIPS) [48] were produced to detect and image astrophysical gamma-ray emissions. Specifically NCT would like to gain more knowledge about gamma-ray bursts, black holes and nucleosynthesis through Gamma-Ray Imaging. NCT has been upgrade substantially and continues as the Compton Spectrometer and Imager (COSI) [8]. GRIPS was proposed to understand solar flares and Coronal Mass Ejection (CME). In security applications there have been Compact Compton Imager (CCI) [59] and Volumetric Compton Imager (VCI) [3] which have been used as 2D imager and 3D volumetric imager systems. CCI and VCI have the goal of discovering and localizing illicit nuclear material.

1.2 Challenges

Semiconductor orthogonal strip detectors improved the information density from the monolithic sensors used previously for Compton Imaging, however much of the Compton scattering information has yet to be recovered. Observation of Compton electrons from gamma-ray scatters in 10 μm high spatial resolution Super Novae Acceleration Probe (SNAP) Charge Coupled Device (CCD) led to the first feasibility measurements of Electron Track Compton Imagers (ETCI) in solid state detectors [60]. The Compton vertex information captured in the Compton electron can provide increased signal-to-noise for Compton event ensembles, open new imaging modalities and lead to direct computation of gamma-ray momenta on an event-by-event basis. ETCI is of interest for high angular resolution Compton systems, however there are many practical problems with the demonstration of [60]. One fundamental

problem is a result of the readout architecture of high spatial resolution CCD detectors. The readout scheme provides high spatial density but trades in time resolution. Time resolution is roughly the Frame Read Time (FRT). The FRT is on the order of seconds for most SNAP devices and scales with the pixel area. Active pixel schemes for readout of electron tracks have been proposed, however they are limited in depletion layer thicknesses and achievable pixel sizes. Small pixel pitch with high signal to noise per pixel is desirable, so that electron track trajectories can be well resolved. Shrinking the pixel size while maintaining signal to noise is an open area of investigation for many active pixel schemes. Additionally information density on fine pixel pitch devices is also a problem, where the data that can be transferred, reduced or processed is limited by density of electronics.

Aside from ETCI practicality issues, there are Compton electron information limits that imply Compton Imaging limits. The measurement of the Compton electron energy and initial trajectory are of great importance for ETCI. The former is concerned with the Compton electron containment probability and energy resolution of a detector. The limit of information that can be collected about the initial electron trajectory is much more difficult to determine. Signal for the Compton electron trajectory depends on the material, device properties and the electrode configuration. Due to the coupled nature of this problem a concerted effort would be required. Preliminary simulations could guide detector fabrication and design. However, achieving detectors with the desired performance characteristics is not trivial, and sometimes the limits of performance are not known until after fabrication and operation.

The significant challenges in Gamma-Ray Imaging based on advanced ETCI sensors is complementary to the simpler Proximity Imaging approach. Investigation of simple monolithic detectors are of interest with recent developments and availability of contextual sensors such as GPS, LIDAR, IMU, etc. and SLAM engines that rely on them. Techniques and developments from SLAM algorithms could provide proximity Gamma-Ray Mapping of radiation sources with monolithic radiation detection sensors. Gamma-Ray Mapping has previously been performed with Compton Imagers VCI and High Efficiency Multimodal Imager (HEMI) [20] that used SLAM solutions suited for indoor environments. Given the large investment in high performance detector development, it is natural to consider the scaling of complexity and cost of simple detectors coupled with contextual sensors.

1.3 Proposed Solutions

This work presents developments in advanced sensors for ETCI toward high resolution Compton Imaging systems. Electron tracking provides a rich physics for Compton interactions and opens up new imaging modalities. CCD-strip (Chapter 4) is proposed as a possible avenue toward the goal of ETCI imagers, seeking to add time resolution to SNAP CCD detectors while maintaining excellent spatial resolution at 10.5 μm in silicon. Also in Chapter 4 we present the simulation benchmarks of a CCD electron tracker and provide the nuclear scattering limit as a design parameter for future ETCI systems. We conclude the chapter with a

discussion of active pixel devices that could provide timing information for electron tracking and discuss the challenges that those devices face.

In contrast to the high resolution Compton Imaging systems that ETCI promises, we present the Localization and Mapping Platform (LAMP), a lightweight and flexible contextual sensor and detector demonstration platform for 3D gamma-ray proximity mapping. We discuss the limits of GPS in mapping, introduce the concept of mobile SLAM, show results from handheld measurements indoors and outdoors as well as provide preliminary results from proximity mapping via an UAS. We discuss the method used for 3D backprojection and the effect of detector angular responses on the two proximity mapping cases. Finally, we conclude with the future challenges that are posed by data sufficiency in Gamma-Ray Mapping and note the role of UAS as autonomous mapping platforms in the future.

Chapter 2

Radiation Detection Fundamentals

Despite the large scope of radiation detection, almost all detectors rely on the electronic excitation of the sensitive medium to measure information about incident radiation[1]. The properties of radiation detectors vary considerably, and the useful interpretations of information encoded is dependent on the instrumentation used to collect it. The information collected depends both on the type of detector and the electronics used for the front end instrumentation. Here we present some general features of traditional gamma-ray semiconductor detectors, conceptual features of the instrumentation front end electronics and limits in performance for a few specific cases.

2.1 Some Properties of Semiconductor Detectors

Semiconductors provide interesting properties for radiation detection because of their well defined electrical structure in the crystalline state, their relatively high densities and the ability to achieve relatively large volumes. The regular crystalline structure and the Pauli exclusion principle define discrete electrical states in the material [28]. The density of states increases with energy, leading to a virtual continuum of states. This continuum is referred to as an energy band. These bands form for both electrons and holes. For electrically pure materials the bands are isolated from each other, at a minimum, by the bandgap. The bandgap represents the minimum amount of energy to promote an electron or hole to the opposing band.

Typically semiconductor detectors are implemented on high resistivity bulk volumes with a rectifying and ohmic contact. Despite the high resistivity of the bulk, there is still some amount of dopant in the volume which establishes the type of the material as a donor or acceptor of electrons. A contact of the opposite type can be applied to form a PN rectifying junction. Additionally, another contact is applied to establish an ohmic or non-blocking contact. The depletion width with no applied bias is driven by charge conservation of the dopants present. Specifically, an intrinsic depletion region is present at the rectifying

[1]The exception being related to detectors which are sensitive to phonons, vibrational quanta.

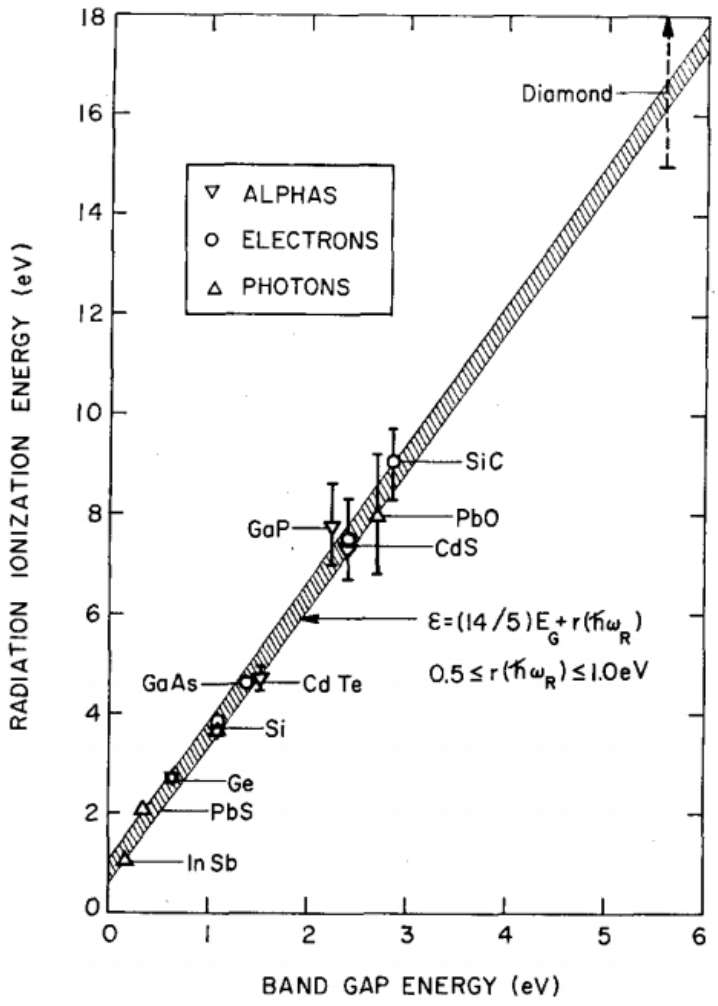

Figure 2.1: The electron-hole pair creation to bandgap energy for many different materials is very consistent with a constant ratio, roughly of about 3 times the bandgap. Figure from [36].

contact, with a width determined by the dopant concentrations on each side of the PN junction. The depletion region can be grown in the device by applying reverse bias so that all free carriers are swept out of the volume, and the static space charge of the dopants is uncovered. Uncovered space charge and applied bias establish field in the device.

Interactions by charged particles in the depleted volume can liberate electron and hole pairs. The readout of charge carriers is explored extensively in Section 2.2. The energy required to generate electron-hole pairs is limited by the phase-space of the wave functions in the crystalline volume and are therefore larger than the bandgap. A series of electron-hole pair creation energies can be seen in Figure 2.1. The figure shows that energy is partitioned for many semiconductors as a fixed ratio of approximately 2:1 for vibrational to charge excitations. This is observed in the slope of the line, where it is helpful to remember

that the bandgap is the minimum energy required for ionization and the electron-hole pair creation energy is essentially the energy required to overcome the bandgap and momentum balances that the lattice phase-space imposes. The momentum transferred to the lattice in e-h pair generation results in phonons. Thus the ratio of the bandgap to the e-h creation energy approximately represents the fraction of energy delivered directly for ionization. The sampling process for creating e-h pairs follows a Poisson distribution. The number of e-h pairs N_{e-h} is proportional to an energy deposited in the lattice E_{dep} by

$$N_{eh} = E_{dep}/\epsilon, \tag{2.1}$$

where ϵ is the e-h creation energy for that material. The e-h pair creation energy may, in general, be a weak function of temperature.

The observed variance of the number of e-h pairs is not exactly $\sigma_{N_{eh}} = \sqrt{N_{eh}}$ as a pure Poisson process would dictate. Energy deposition in the lattice samples other excitation processes which generate other information carriers such as vibrational quanta (phonons), which are not charged. For this reason, the observed variance on the e-h pairs for semiconductors is smaller than the Poisson variance[2]. The Fano factor has been defined as

$$F = \frac{\sigma_{observed}}{\sigma_{N_{eh}}}, \tag{2.2}$$

which is an a posteriori model to describe the experimentally observed variance. Given that the phonon and e-h creation processes are both Poisson sampling processes, one might expect that the Fano factor is independent of energy for semiconductors. For semiconductor detectors this is typically less than one[3].

The modified variance $\sigma_{Fano} = \sqrt{F\epsilon E_{dep}}$ defines what is referred to as the statistical limit in the charge spread of a monoenergetic charge deposition. The resulting distribution about the monoenergetic deposition approaches a Gaussian distribution for large numbers of events. The ability to resolve monoenergetic depositions introduces the concept of energy resolution, and is conventionally discussed as the Full Width Half Max (FWHM) of the Gaussian distribution. One can show that the statistical-Fano limit FWHM is given by

$$W_{Fano} = 2.355\sqrt{F\epsilon E_{dep}}. \tag{2.3}$$

[2]If one knew the total number of information generating channels and the creation energies for each the variance could be directly calculated. Please see the excellent discussion by [36].

[3]This discussion has been focused on semiconductors. If one uses Equation 2.2 to compute Fano factors for scintillators the result is greater than one. [57] provides an in depth discussion, essentially the effect is related to the non-proportionality of the light yield for electron deposition in those lattices and the electron track.

2.2 Signal Formation

Charge liberated by an external stimulus in a reverse biased semiconductor drifts toward the electrodes due to the established electric field. The signal from a drifting charge is due to induction from both electrons and holes. Ideally the signal generated is only dependent upon the geometry of the electric fields and electrode configuration. Shockley-Ramo's theorem [46] states that the induction from a point charge q on an electrode is

$$\delta Q = q(\phi_n - \phi_{n-1}) \tag{2.4}$$

when a charge has moved in a weighting potential ϕ along spatial coordinates coded by n and the previous position n-1. The weighting field ϕ is unique for unique electrodes and can be obtained by raising the electrode of interest to unit potential and ac-grounding all others. The weighting potential is independent of the uncovered lattice space charge and applied bias, as derived by Ramo for electrostatic fields. The weighting potential relates the sensitivity of an electrode to a point charge q at each spatial dimension in the volume. The electric field $\vec{E}$ controls the drift motion through the weighting potential of the point charge

$$\vec{v} = \boldsymbol{\mu} \cdot \vec{E}, \tag{2.5}$$

where $\boldsymbol{\mu}$ is the mobility tensor of the crystal, $\vec{E}$ is the applied electric field, and $\vec{v}$ is the velocity of the point charge. The motion between n and n-1 implies induced current, where the delta in time is given as $dt = t_n - t_{n-1}$ from the distance between n and n-1 and the velocity $\vec{v}_{n-1,n}$. The induced current is then related to both the electric field and weighting field characteristics. If the induced charge were measured ideally, these would describe the signal produced. The instrumentation to measure the induction is sometimes limited in ways that are discussed in Section 2.2.

The instrumentation to measure the induced/collected charge is typically a Charge Sensitive Preamplifier (CSA) which ideally converts the input charge to a voltage signal. Detectors and instrumentation also have fundamental limits on the measurement of the input charge, so processing of the output voltage signal may be necessary to achieve maximal signal to noise.

Simulation of segmented electrode configurations is important to understanding the ideal performance of a radiation detector and the signal that is generated. Figure 2.2 presents a Finite Element (FEM) solution of the charge drift and induction process for charge deposition in a silicon CCD-strip detector. The details of CCD-strip are fully explored in Chapter 4, however the schematic cross-section and important coupling parameters are shown in Figure 2.3. Charge induction is modeled for the time sensitive strip electrodes, while the implant metal for CCD pixels are modeled as a monolithic electrode. This approximation holds for generation of strip signals due to the implants' relatively small pitch compared to the depletion thickness. Additionally, the strips are perpendicular to the implants for the pixel plane. Important parameters for the strip electrodes are the strip pitch, the distance between strip centers, and the gap, the separation distance between electrodes. The upper

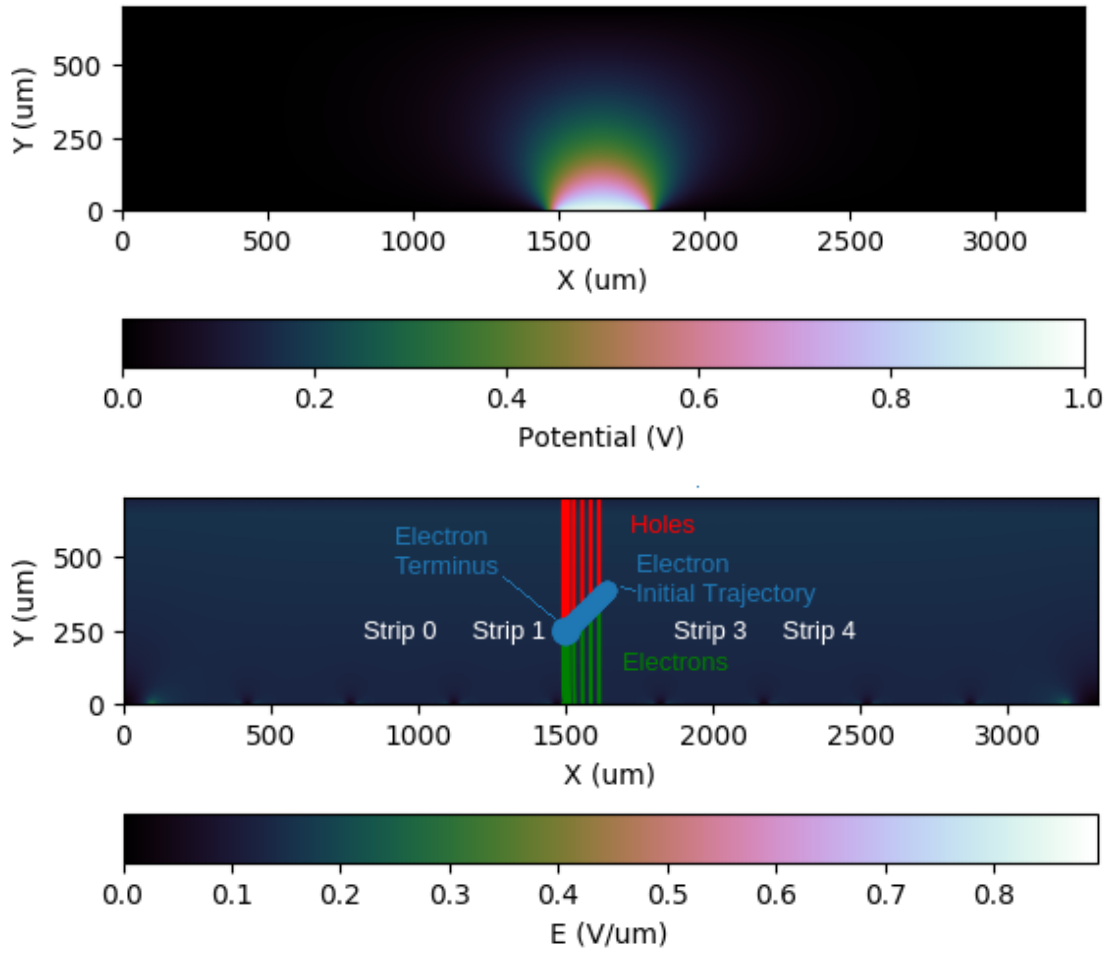

Figure 2.2: (Upper) Simulated weighting field in a CCD-strip device with a pitch of 35 10.5 μm pixels and a depth of 650 μm. (Lower) Electric field and a model electron track of approximately 300 keV-Si. Drift lines are shown for both carriers. The ratio of energy in the initial segment of the track to the deposition in the terminus is 1:4.

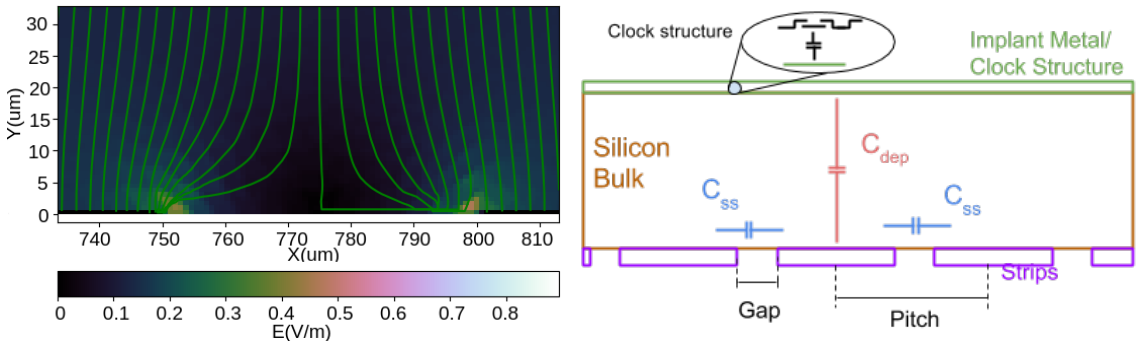

Figure 2.3: (Left) Simulated electron trajectories on strip side of CCD-strip device shown in green splitting the gap between electrodes. The space between electrodes can be weak in field and thus have a curved trajectory around the gap. (Right) Geometry of CCD-strip for Figure 2.2 and this figure. Additionally, we introduce the concept of strip-strip capacitance C_{ss} and depletion capacitance C_{dep} for Figure 2.5.

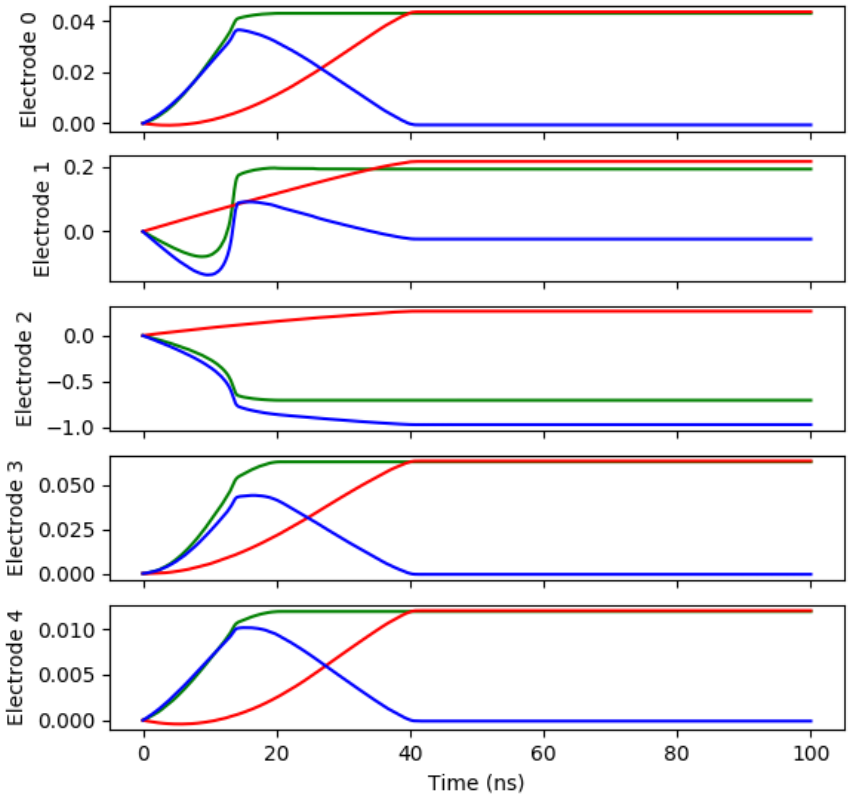

Figure 2.4: Induced charge signals on the inner 5 electrodes from the electron track in Figure 2.2. Green, red and blue traces are for the induced electron, hole and net signals on the electrode of interest. The y-axis is in normalized charge. Notice that charge only integrates on electrode 2 while charge is induced on the rest of the electrodes.

panel in Figure 2.2 is a weighting potential result for the central electrode plotted in volts. The relative magnitude of the potential versus position in the bulk is the important feature of this plot. The weighting potential is strongest near the sensitive electrode. Additionally, in the lower panel: a simulated deposition of charge that is consistent with a toy relativistic electron injection in the middle of the volume. The charge injection represents the features one would expect from gamma-ray interactions: a variable but low charge deposition density along the initial portion of the electron track and a high density terminus. The shape of the electron track can change dramatically with energy; the modeled track represents a 300 keV electron in a silicon device. The track can be oriented in different directions but the example shown is in the plane perpendicular to the strip electrodes. Charge drift paths are represented as red and green lines for holes and electrons respectively, though only a sample is plotted. Figure 2.3 shows a zoomed picture of electron drift lines around the gap between two metal electrodes. In the right panel there is a schematic of the volume simulated with the inter-strip and depletion capacitance labeled. Figure 2.4 shows the induced charge for the electron track presented in the lower plot of Figure 2.2. Green, red and blue lines correspond to the induced electron, hole and net signal on the electrode of interest. The results were produced from the author's Signal Formation framework which uses open-source FEM Elmer to perform abstracted field simulations and charge induction. Another product of this framework is that inter-electrode capacitances can be calculated. For a constant gap, of about 12 percent of the strip pitch, for the capacitances defined in Figure 2.3 can be computed. Figure 2.5 presents this calculation plotted against dimensionless axes w_{dep}/p and C_{s-s}/C_{dep}. These represent the depletion width to pitch ratio and the strip-strip capacitance versus the depletion capacitance of the detector.

The results from the Signal Formation framework are important in that it these represent the ideal case for signal generation on a metal electrode. The ideal signal generation is degraded by physical characteristics of real detectors such as field distortions at the detector periphery, weak field areas, weak strip isolation, trapping as well as others effects. The solution and cause for these effects is outside of the scope of this work, however the next section investigates the impact of instrumentation as a possible source of fidelity loss in segmented front ends.

Charge Sensitive Preamplifier (CSA)

The CSA is a charge integrator whose output is a voltage signal that is proportional to the input charge. A CSA is typically the first stage of amplification in a semiconductor system. The characteristics of the CSA are especially important to multichannel or spatially coded semiconductor detector systems. Characteristics of the CSA or 'front end' are examined while building complexity to the multichannel configurations.

Figure 2.6 is a schematic representation of a single channel, ideal charge amplifier with input capacitance to ground of C_{in}. The input capacitance is not desired but unavoidable and thus sometimes referred to as parasitic capacitance to ground. This CSA has a gain of $g_Q \equiv v_{out}/Q_{in}$, by definition. Note that the input capacitance is external to the charge

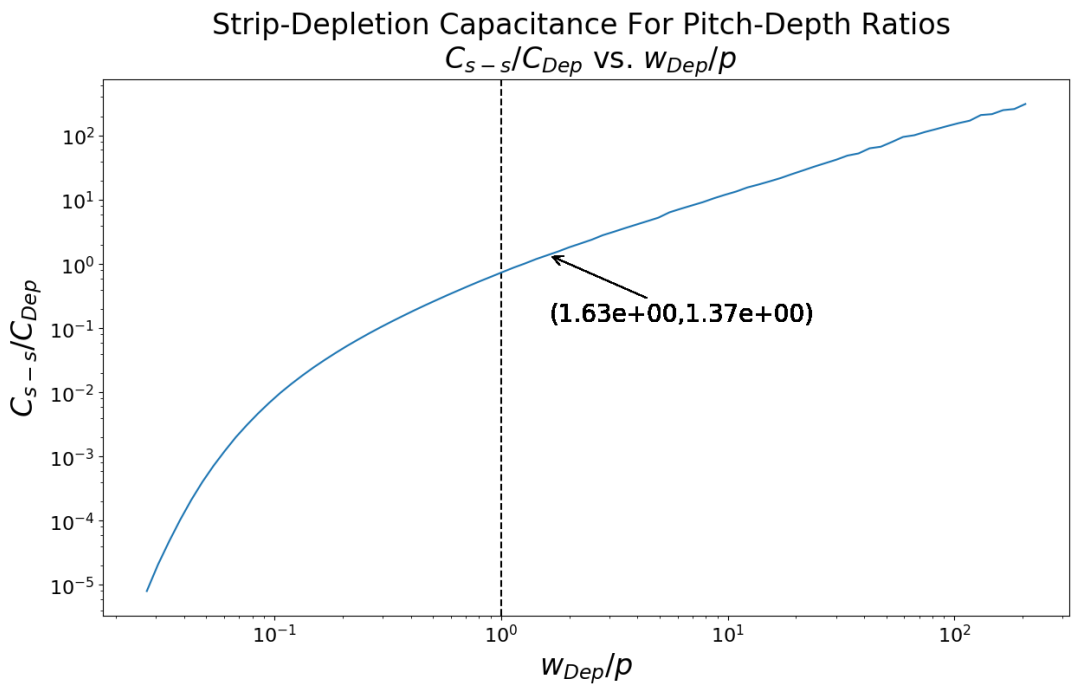

Figure 2.5: Strip to depletion capacitance ratios vs pitch to depletion depth. This calculation employed field simulations for planar strip detectors for a fixed gap to pitch ratio of 0.12. The dashed line indicates where the strip pitch is equal to the depletion depth. To the far right of this line one sees the small pixel effect, where the strip-strip capacitance dominates. To the far left of the dashed line the detector approaches a planar electrode approximation, where the depletion depth is very small compared to the electrode size. The arrow shows where CCD-strip (discussed in Chapter 4) lies on this plot.

amplifier and that the gain ideally does not depend on C_{in}. The insensitivity to input capacitance could occur if the input impedance of this amplifier is very small so that charge division would not occur between the input capacitance and the input of the amplifier. Low input impedance to ground at the amplifier input is analogous to the virtual ground concept, as charge would be absorbed if the impedance to ground was very close to or at zero.

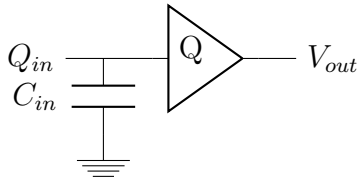

Figure 2.6: Schematic charge sensitive amplifier. The output voltage V_{out} has an AC component v_{out} which is proportional to the input charge Q_{in}. The amplifier schematic symbol enclosing Q implies that this is a charge amplifier with buffered voltage output. C_{in} is the total input capacitance to ground.

A possible preamplifier might be implemented as a continuous reset charge sensitive preamplifier, Figure 2.7. The output voltage of this stage V_{out} has an AC component v_{out} which is proportional through the gain g_Q to the deposited charge Q_{in}. The gain A of the amplifier is the frequency dependent open loop gain which may have high DC gain that falls off at higher frequencies.

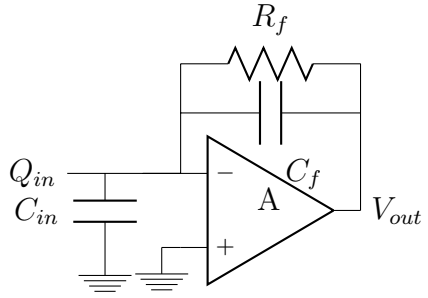

Figure 2.7: A finite gain continuous reset charge sensitive amplifier.

The gain Figure 2.7 for infinite open loop gain A is $g_Q = 1/C_f$. An impulse of charge Q_{in} would integrate entirely on the feedback capacitance. This impulse is slowly dissipated through the feedback resistor. The reset is achieved with a time constant set by $\tau_d = R_f C_f$, $v_{out}(t) = \frac{Q_{in}}{C_f} e^{-t/\tau_d}$. The result assumes the collection time for the charge is much less than τ_d.

So far, assumptions have been made about characteristics of preamp that are not appropriate for real systems. Suppose that Figure 2.7 has finite gain. To compute the charge gain, it is necessary to find the fraction of charge that is integrated on the feedback capacitance. The op amp action on the input means that $v_{out} = -Av_-$, implying that $Q_f = C_f(v_{out} - v_-) = -(A+1)C_f v_-$, provided that the charge input pulse is much shorter than τ_d, and the op amp inputs are ideal. Now computation of the gain: $g_Q = \frac{v_{out}}{Q_f} = \frac{A}{A+1}\frac{1}{C_f}$. The input model of the amplifier be rephrased by observing that $-Q_f/v_- = C_f(A+1)$ represents a property of the amplifier input node v_- when negative feedback is applied through C_f. This property of the input is known as the dynamic capacitance

$$C_i \equiv C_f(A+1). \tag{2.6}$$

The dynamic capacitance of the input represents another model for the input of a CSA, represented by Figure 2.8. This is not a physical capacitance but rather a compact statement of how a CSA responds to input charge.

Equation 2.6 and Figure 2.8 imply that the input charge is shared between C_i and C_{in} due to finite gain. As described in Figure 2.6, low input impedance is desirable. However, maximization of g_Q helps to improve the signal to noise on the relatively small amount of charge integrated on the input. Finite gain amplifiers imply that g_Q and input impedance are in competition, the best balance considers the optimum signal to noise when the front end is fully instrumented. One can verify that the input impedance and dynamic capacitance

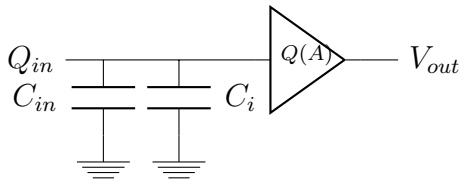

Figure 2.8: Schematic charge sensitive amplifier with finite gain, input impedance. The output voltage is proportional to the input charge Q_{in}.

are related by observing that for negative feedback $Z_{in} = \frac{Z_f}{1-A}$, where Z_{in} represents the frequency dependent input impedance and Z_f represents the effective impedance of the parallel feedback components R_f and C_f. At intermediate angular frequencies, ω, the feedback impedance is dominated by the capacitance contribution: $Z_f = 1/(j\omega C_f)||R_f \approx (j\omega C_f)^{-1}$. The dynamic capacitance is approximately the reciprocal of the input impedance for $A \gg 1$. In explicit terms, for $A \gg 1$ compare the magnitude of $|Z_{in}| \sim (\omega C_f A)^{-1} \sim (\omega C_i)^{-1}$ and the $g_Q \sim C_f^{-1}$ to find that the input impedance and charge gain are proportional. The charge gain cannot be maximized for real amplifiers without incurring a finite input impedance.

The assumption of $A \gg 1$ is limited, consideration of $A(\omega)$ is more correct. Internal gain $A(\omega)$ of a simple amplifier follows $A(\omega) = A_0/\sqrt{1 + (\frac{\omega}{\omega_0})^2}$ where ω_0 is defined as the dominant pole corner frequency [26]. Unity gain frequency is observed at $\omega_1 \approx A_0\omega_0$ and is known as the Gain-Bandwidth Product (GBP). Noting that the gain drops linearly with frequency, with 90^o phase shift from the dominant pole, we can express the gain as $A(\omega > \omega_0) \approx \omega_1/(-j\omega)$. The input impedance is then

$$Z_{in} \equiv \frac{Z_f}{1-A} \approx (\omega_1 C_f)^{-1}, \tag{2.7}$$

which is real for frequencies above the amplifier corner frequency, ω_0, and below the GBP, ω_1. This conclusion reaffirms the charge gain and input impedance tradeoff for a typical amplifier response. Here we also learn that the impedance is real and thus resisitive.

Many front ends of interest use multiple preamps in order to encode spatial information across the detector. For this scenario consider Figure 2.9, where two preamps are instrumented on a front end, coupled by a parasitic capacitance C_{ss}. The two preamps have different input impedances/dynamic capacitances with charge $Q_{in,0}$ initially on each amplifier input. This setup will be referred to as common mode charge injection. At equilibrium, on a time scale much less than τ_d of the amplifiers, charge will have been induced through the C_{ss} capacitance if the two dynamic capacitances are unequal. Unequal input impedance incurs a charge error δ_Q that is seen as an error in the integral charge that will be buffered as v_{o1}. For different ratios of C_{ss} and C_{d2} the percent error in the charge that integrates on C_{d1} is presented in Figure 2.9. Bands are listed for a range of energy resolutions that might be of interest for semiconductors in the 200 keV to 1 MeV band.

Figure 2.9 is a conservative estimate of the charge error introduced. For example suppose that for one amplifier $Q_{in,0} = 0$. At equilibrium, the charge error would be much greater.

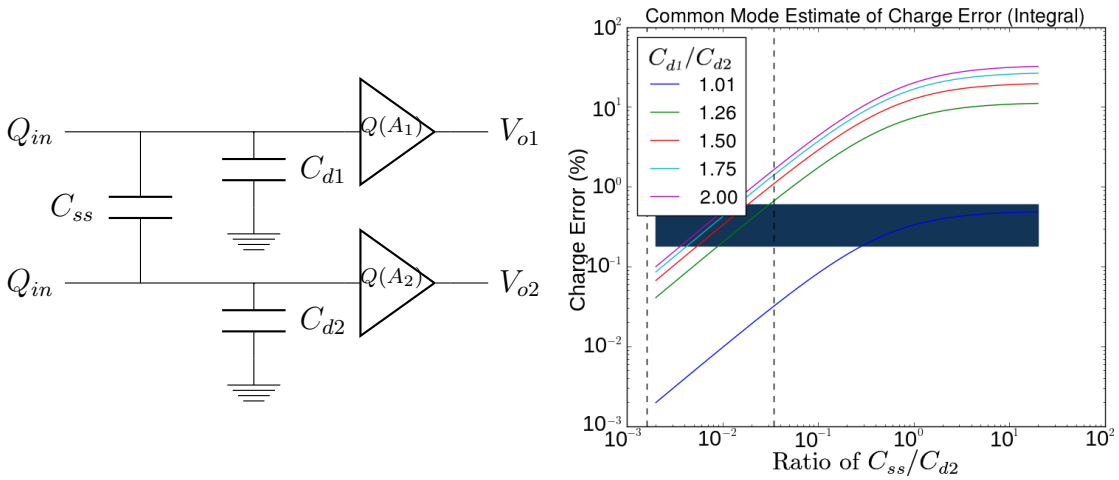

Figure 2.9: (Left) A front end with multiple amplifiers coupled by parasitic capacitance C_{ss}. The injection of charge onto both inputs is referred to as the common mode charge injection scenario, it is conservative to the charge errors estimated. (Right) Estimates of the impact of finite open loop gain in a coupled front end. The charge errors shown are present on the typical integration periods of detector systems. Initially Q_{in} exists on each input, however C_{ss} coupling implies that charge will be transferred to achieve equilibrium. The blue band defines the region of charge error that would impact high performance semiconductor detector systems. As the plot shows minimizing the input impedance relative to the coupling capacitance greatly reduces the effect, however the charge gains g_{Q_i} also fall.

Because of the dynamics of these effects, the charge induced through C_{ss} is restored on a timeline corresponding to τ_d of each amp. The charge error is restored over time, however the timescale is outside the typical charge integration period, which is defined by signal to noise tradeoffs.

The internal gain of an amplifier, more specifically the GBP, is important to capturing the detector signal with high fidelity. Amplifiers that do not significantly distort the charge induction over time exceed the signal bandwidth. The signal bandwidth of detector signals can be approximated through the expected rise time of pulses. It is a useful to approximate this risetime as a step voltage in time with $t_{rise} \equiv t_{90\%} - t_{10\%}$. A common rule of thumb for a square wave with finite risetime t_{rise} is

$$B \approx 0.35/t_{rise}. \tag{2.8}$$

Risetimes vary within detectors, however we are typically interested in charge drift times of about 1-1000ns, implying bandwidths of 350 MHz to 0.35MHz. Charge drift times are used as the estimate because they are not convolved with the amplifier response. The implied bandwidths are not the only frequency bands of interest, however detector front ends should exceed these bandwidths in GBP to avoid instrumentation limited readouts, especially when fidelity is required in the signal risetime. As has been demonstrated for high charge gain, the

input impedance demands that the GBP be high. Multichannel systems offer these problems in compounded complexity.

Front end limited risetimes can be calculated assuming a step input in charge. Since the input impedance is real over the bandwidth of interest, the input capacitance C_{in} discharges through the amplifier input

$$\tau_i \approx Z_{in}C_{in} = (\omega_1 C_f)^{-1}C_{in}, \tag{2.9}$$

Equation 2.9 is another manifestation of the charge gain and input impedance issue for finite GBP amplifiers.

In Figure 2.8 we noted that the charge is divided between C_{in} and C_i. One could express this as the charge that integrates on C_i as $Q_s = Q_{in}(1 + C_{in}/C_i)^{-1}$ which reduces the signal by a constant fraction if $C_i \sim C_{in}$. Combining this with the RC time constant on the input allows the summation of effects due to the amplifier on collected charge

$$Q(t) = Q_{in}(1 + C_{in}/C_i)^{-1}(1 - e^{-t/\tau_i}), \tag{2.10}$$

This case does not investigate the detector characteristics, which would include the drift, induction and collection of a charge cloud on the buffered signal v_{out}.

Here we conclude our cursory discussion of CSAs and the coupled parameters that limit performance in single and multichannel systems. Understanding the limits are important to the utility of the buffered charge amplitude and to the time dependent induction information. Both of these are always convolved with the preamp response. High fidelity systems require consideration of the limits that preamps may impose, especially in the case of multichannel systems, where coupling of channels may provide nonideal information.

In the next section we discuss conventional pulse processing for the extraction of energy information from the preamp output.

2.3 Noise, Signal Shaping, and Energy Resolution

Motivation for signal shaping can be found in assessment of the noise model, including the detector and CSA preamplifier (Figure 2.10). As shown in the figure, two types of noise contributions are modeled. The two sources cover the possibility space for noise components: those that are in series with the input to ground and those which are parallel to the input. Series and parallel noise are also known by the names voltage noise, e_i, and current noise, i_n respectively.

By inspection one can notice that the voltage gain of the amplifier is $\frac{C_{in}}{C_f}$ and the current gain is $\frac{1}{j\omega C_f}$. Supposing that the two noise sources are uncorrelated we can sum them in quadrature for the equivalent voltage noise on the output

$$v_{n0}^2 = e_n^2|\frac{C_{in}}{C_f}|^2 + i_n^2|\frac{1}{j\omega C_f}|^2, \tag{2.11}$$

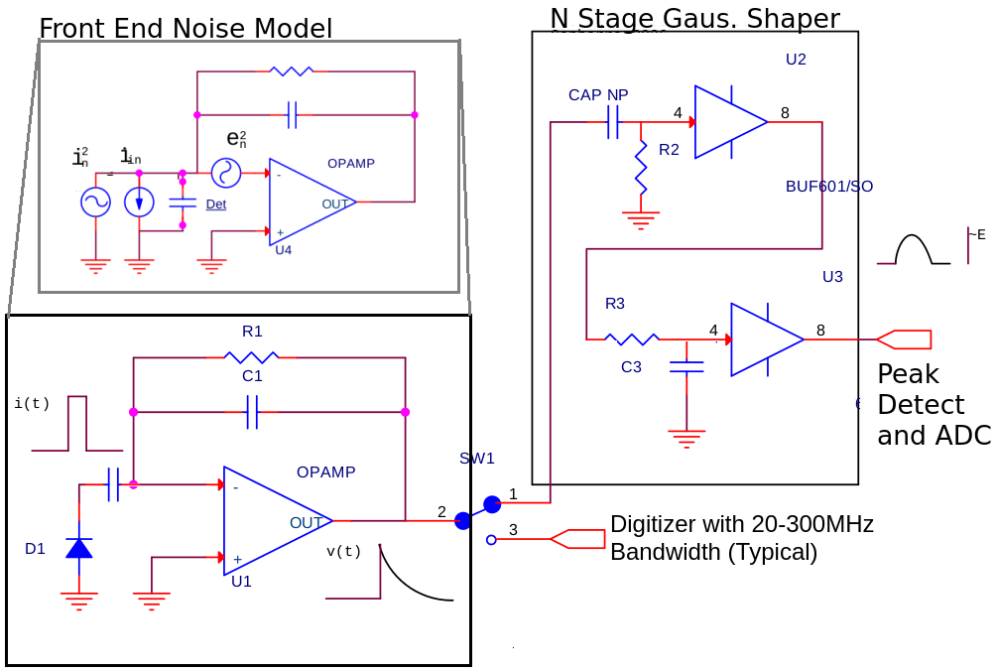

Figure 2.10: (2-1 switch configuration) Schematic of analog signal chain for a CR-RC Gaussian shaper.(2-3 switch configuration) Schematic of digital signal chain where the preamplifier pulses are directly digitized.

However, this needs reference to the input. Output noise can be referred to the input by an equivalent current noise

$$i_{neq}^2 = e_n^2 \omega^2 C_{in}^2 + i_n^2, \tag{2.12}$$

at the input. To proceed, we must investigate the contribution of different noise sources to the current and voltage noise at the input. Here we refer to [50] for a derivation of the spectral noise densities related to specific sources of noise on the front end. Spectral noise densities describe the noise power over specific frequency bands. The two functions of particular interest are those that are flat in power with frequency, or white noise, and those that exhibit noise power proportional to 1/f, where f is linear frequency and 1/f is the so called "1/f" noise.

The signal bandwidth of the front end defined by Equation 2.8 is only constrained at the upper limit. White and 1/f noise generators provide the low end constraint to the bandwidth in ideal systems due to increasing contribution over the signal amplitude. Constraining the system bandwidth, conceptually, could improve a number of measurements such as arrival time, signal charge or other more complicated information. A simple band limiter is a differentiator and integrator for attenuation at frequencies above and below the time constants for each. Such a band limiter for pulse processing is colloquially referred to as a shaper. Pulse processing or shaping typically serve the purpose of charge or interaction time estimation.

The tradeoff in noise and signal quality can be calculated using the system transfer function composed of the preamp and a simple shaper (CR-RC). The appropriate transfer system transfer function is obtained by convolving the appropriate stage gains. For a CR-RC shaper one can derive the voltage-voltage transfer function in the simple analysis for a differentiator and integrator

$$H_{CR}(s) = \frac{1}{s\tau_{CR} + 1} \tag{2.13}$$

$$H_{RC}(s) = \frac{s\tau_{RC}}{s\tau_{RC} + 1} \tag{2.14}$$

$$H_{tot}(s) = H_{RC}(s)H_{CR}(s), \tag{2.15}$$

where H is the stage transfer function in frequency space $s \equiv j\omega$ and the subscripts denote the stage. If one assumes[4] that $\tau_{RC} = \tau_{CR}$ and uses the gain of the preamp then one arrives at the transfer function for the entire system

$$T(s) = \frac{1}{sC}\frac{G_v}{s\tau + 1}\frac{s\tau}{s\tau + 1}, \tag{2.16}$$

where T is the total transfer function of the preamp and shaper and where G_v is a constant added for gain of the shaped signal - the (CR-RC) of the shaper has at minimum -6dB amplitude attenuation at τ_{RC}. Additional gain is provided in the shaper to keep the shaped signal in the input range of subsequent stages.

The noise contribution can now be estimated by applying the system transfer functions to the front end noise components. Typically this is expressed as equivalent voltage noise on the output of the shaper, RMS noise, or ENC at the input of the preamp. To compute the total noise power we can evaluate the RMS noise from the power integral

$$v_{tot}^2 = \frac{1}{2\pi}\int_0^\infty i_{neq}^2 |T(j\omega)|^2 d\omega, \tag{2.17}$$

where v_{tot} represents the output RMS voltage. For brevity we compute three integrals for e_{white}^2, $e_{1/f}^2$ and for i_{white}^2. Note that these integrals compute the scaling for series white noise,

[4]This defines a system bandwidth.

series 1/f noise and parallel white noise.[5] The integrals evaluate to

$$\begin{aligned} v^2_{white,series} &= \frac{e^2_{white}C^2_{in}}{2\pi}\int_0^\infty |T(j\omega)|^2\omega^2 d\omega \\ &= \frac{e^2_{white}C^2_{in}}{2\pi}\frac{\pi G^2_v}{4C^2_{in}\tau} \\ &= \frac{G^2_v}{8}\frac{e^2_{white}}{\tau} \end{aligned} \tag{2.18}$$

$$\begin{aligned} v^2_{1/f,series} &= A_f C^2_{in}\int_0^\infty |T(j\omega)|^2\omega d\omega \\ &= A_f C^2_{in}\frac{G^2_v}{2C^2_{in}} \\ &= \frac{A_f G^2_v}{2} \end{aligned} \tag{2.19}$$

$$\begin{aligned} v^2_{white,par} &= \frac{i^2_n}{2\pi}\int_0^\infty |T(j\omega)|^2 d\omega \\ &= \frac{i^2_n}{2\pi}\frac{\pi G^2_v\tau}{4C^2_{in}} \\ &= \frac{G^2_v}{8C^2_{in}} i^2_n\tau \end{aligned} \tag{2.20}$$

$$v^2_{tot} = \frac{G^2_v}{8}\left(\frac{e^2_{white}}{\tau} + 4A_f + i^2_n\tau\frac{1}{C^2_{in}}\right), \tag{2.21}$$

where v_{tot} represents the total noise at the output of the preamplifier and shaper due to the noise model in Figure 2.10. A_f is introduced in the 1/f series noise contribution and is the noise coefficient for 1/f noise in the CSA input stage. The total system gain is $G_{tot} = \frac{G_v}{C_{in}}$. The Equivalent Noise Charge (ENC) is the noise at the input and is calculated by removing the system gain

$$ENC^2 = Q^2_n = \frac{1}{G^2_{tot}} v^2_{tot}, \tag{2.22}$$

which is most often expressed in RMS electrons or FWHM energy for specific materials. Equation 2.22 is dubbed as the electronic noise contribution for detectors, although it contains many parameters not specifically related to the readout instrumentation. A complete discussion of the individual components e_{white}, A_f and i_n is given in [45].

[5] We assume that the 1/f noise from the detector crystal is negligible compared to the flicker noise from the input stage of the preamp electronics. This is done by assumption since it's magnitude may be related to crystal quality [45].

Two conclusions precipitate from Equation 2.22: there may exist an optimal shaping time where ENC is minimized with respect to τ, and that small total input capacitance C_{in} is desirable when considering noise only. The first conclusion results from competition between the magnitude of series and parallel white noise. Parallel noise depends on $\sqrt{\tau}$ and series noise depends on $\frac{1}{\sqrt{\tau}}$. One can also observe that the contribution of the series 1/f noise is constant with respect to shaping time.

Physical Noise Generators

The discussion about noise contributions has been constrained to the frequency dependence of noise sources around the front end, but has not addressed the issue of what physical sources may contribute to the noise profile. The full description is in the expansion of Equation 2.22 [50]

$$Q_n^2 = \frac{e^2}{8}\big[(2eI_d + \frac{4kT}{R_p} + i_{na}^2)\tau + (4kTR_s + e_{na}^2)\frac{C_{in}^2}{\tau} + 4A_f C_{in}^2\big], \tag{2.23}$$

where i_{na}, e_{na} and A_f are properties of the amplifier, R_p is shunt resistance across the detector, R_s is series impedance, and I_d is the magnitude of the leakage current.

From Equation 2.23 we observe that the series white noise can be sourced from Johnson noise/thermal noise of series resistances. Power dissipating processes cause fluctuations in carrier velocity that generate the white, frequency independent noise and is present regardless of whether current is flowing. Amplifier inputs also have white voltage noise on their inputs which contribute the series white noise.

Parallel white (shot) noise can manifest as noise due to total leakage current fluctuations through the bulk and along the detector surfaces [26]. Unlike Johnson noise this kind of noise does not depend on temperature but simply the magnitude of the leakage (which often depends strongly on temperature). Shunt impedances can also play a role as Johnson noise sources.

Series 1/f noise is typically correlated with crystal or semiconductor material quality [45]. In general, this noise can be attributable to the input of the amplifier. For transistors, the models for 1/f noise can be more complicated however they are mostly related to the carrier trapping/detrapping and mobility fluctuations. The relationship for front ends can depend on the operational mode of the circuit [51].

Energy Resolution of Semiconductors

The Fano limit of energy resolution in semiconductors was previously presented and can now be used to address the issue of energy resolution in semiconductor detectors in combination with the recognition of the electronic noise contribution. Provided that these sources are independent, they sum in quadrature to obtain the FWHM of a monoenergetic energy

deposition [37]

$$W_{mono}^2 = W_{Fano}^2 + W_{elec}^2 + W_{collection}^2, \tag{2.24}$$

where W_{mono} represents the monoenergetic FWHM, W_{elec} represents the 'electronic noise' and $W_{collection}$ represents broadening due to charge collection effects. The last of those listed, $W_{collection}$ has not been discussed at length but relates to the charge collection, trapping and detrapping of charge signal. Reference [37] provides an in depth discussion of collection effects. The magnitude of charge collection effects vary based on the detector material used, but is typically smaller than the other contributions and is most noticeable on the low energy side of peaks of a high resolution energy spectrum. The charge collection effect is most noticable on the low energy tail of a monoenergetic charge deposition because some depositions drift longer in the material, thus losing more charge due to trapping [37].

Equation 2.24 naively claims the signal to noise tradeoff is completely captured in the electronic noise contribution, except in extreme cases of collection losses. This is true given that the risetime of pulses is not comparable with the shaping time. For detectors that have fixed shaping time, or in general fixed bandwidth, the electronic contribution is fixed. For high resolution spectrometers, the collection component weakly depends on energy. Thus the energy dependence of resolution is captured by the Fano contribution. In general, the percent resolution of detectors decreases with increasing energy.

Figure 2.11 presents a result of a single electrode, high energy resolution HPGe spectrometer attached to a digital pulse processing shaper system with a trapezoidal filter at several shaping times. Equation 2.24 was fit to the data and the individual components of the fit corresponding to series, parallel and 1/f noise are plotted. Inset on Figure 2.11 is the estimate of the components at the optimal shaping time of 1500 ns. The shaper was implemented on a LabZY nanoMCA, an "Open FPGA" radiation detector signal processing toolbox and development platform [56].

Energy resolution is an important parameter describing detector performance, but is perhaps not the only parameter of interest. In general, the information captured in signals are impacted by the front end characteristics, as discussed in this chapter. Additionally, we presented how information is generated in signal formation, some simple amplifier characteristics and noise contributions that impact performance in single channel and multielectrode systems. We have introduced some of the detector front end characteristics that will be relevant to the development of the CCD-strip system discussed in Chapter 4.

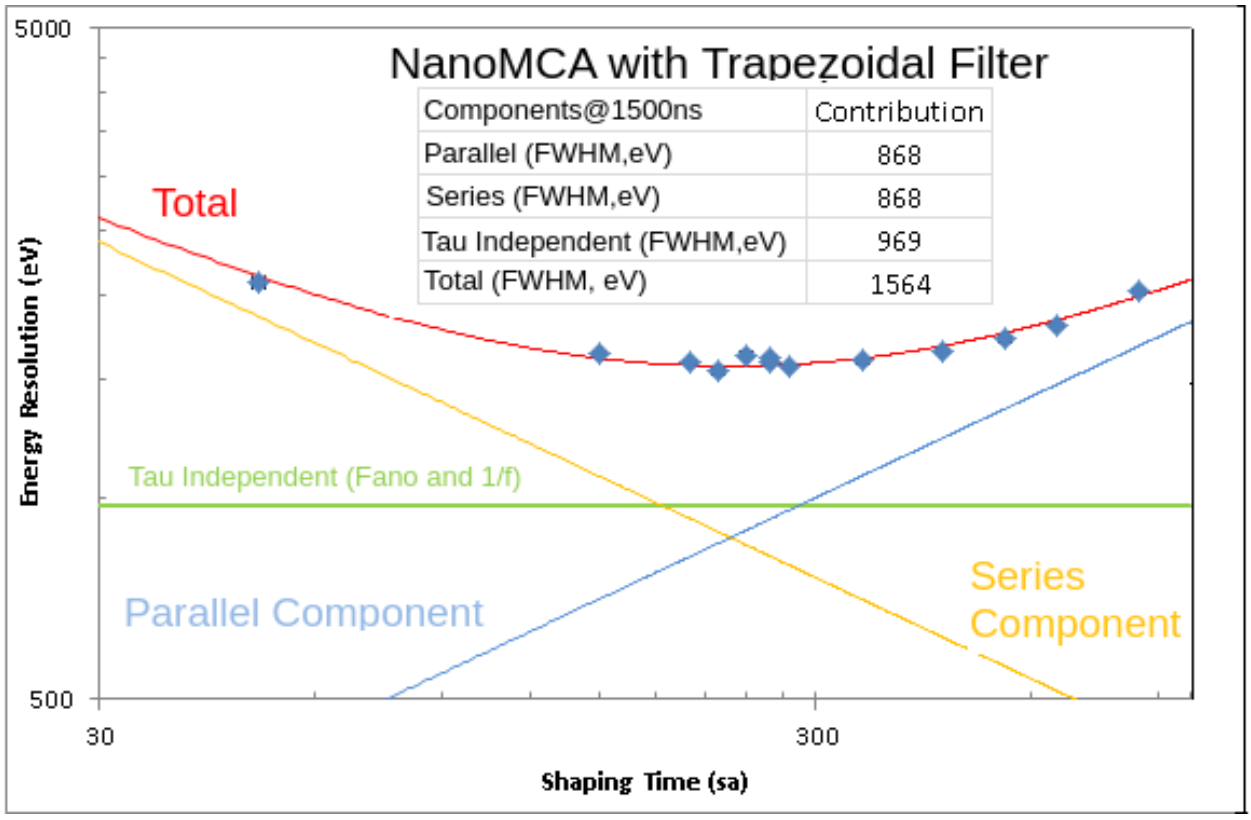

Figure 2.11: Shaping time optimization of a 10% HPGe radiation coaxial detector for the ^{137}Cs photopeak at 661.7keV. Here we can see the voltage noise in yellow, current noise in blue and 1/f noise as the remainder. The red line is a fit if equation Equation 2.22. Inset is the contribution of different components from Equation 2.21 at the optimal shaping time of 1500 ns. This analysis was performed with an 80 MHz digitizer running a trapezoidal filter for energy determination. Real-time signal processing was implemented on a LabZY NanoMCA [56], an "Open FPGA" radiation detection signal processing toolbox and development platform.

Chapter 3

Gamma-ray Imaging

Gamma-Ray Imaging seeks to invert incident gamma-ray flux on a radiation detector to discover the location and distribution of radiation sources; fundamentally, Gamma-Ray Imaging is the link to radiation physics which allows Gamma-Ray Mapping to be possible. Specifically, Gamma-Ray Imaging provides the ability to associate or characterize objects with their radioisotope signatures. Here we assume that the object can be inspected through gamma-ray detection. Sources of interest can either be gamma-ray emitters or inferred by specific gamma-ray emissions. Gamma-Ray detectors possess a wide variety of performance characteristics; fundamentally Gamma-Ray Imaging requires that detectors have one or a combination of position, energy or time resolution. The use of physical information encoded in data collected is the root of gamma-ray imaging. Physical information is consumed by algorithms making use of signal modulation or kinematics of the gamma-ray interactions for localization.

Applications for Gamma-Ray Imaging are varied, and have been briefly introduced in Chapter 1. This chapter is focused on two methodologies for Gamma-Ray Imaging: proximity and Compton Imaging. Proximity imaging based detector systems can offer reduced complexity and can lower performance requirements on radiation detectors used. For example, proximity imaging systems can rely on monolithic, relatively low energy resolution radiation detectors. However, Compton Imaging has strict requirements for radiation detectors: they must be able to resolve individual Compton scattering interactions from single photons. As to be discussed, the Compton mode is limited to high performance detectors. Increased complexity improves detector metrics, such as time, spatial and/or energy resolution. These afford better use of the physics information encoded in gamma-ray interactions. The Compton Imaging mode relies on rich gamma-ray data, conceptually offering more contrast or specificity for complex measurement scenarios. The proximity and Compton Imaging mode represent simple to complex systems as well as systems that rely on signal modulation to those that use photon kinematics.

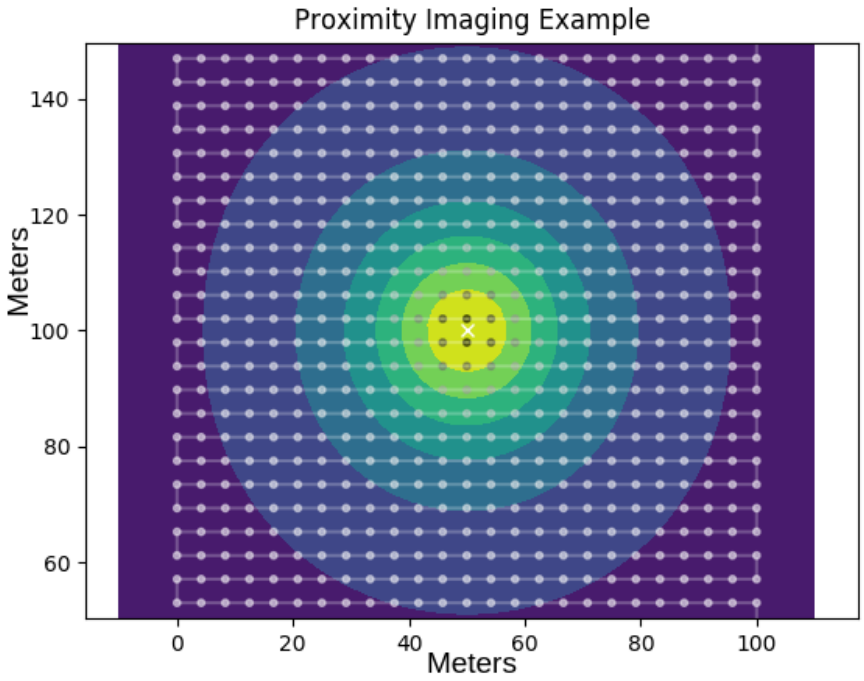

Figure 3.1: A simulated source measurement where a raster pattern is used to sample a source located at (50,100) m as denoted by the white "X". The distance of closest approach is about 8 m. The graph shows positions and trajectory in white to black for the relative intensity of the source strength at each location. In this simulation, the trajectory, data represents only the $1/R^2$ component of the source modulation. Each position in the trajectory data is backprojected onto a grid which is displayed as the colormap from blue to yellow in relative intensity. Both the trajectory data and the backprojection data provide localization, however the impulse response of backprojection is much broader (Figure 3.2).

3.1 Proximity Imaging

Proximity Imaging is a modality of Gamma-Ray Imaging which uses distance modulation to infer source location. Proximity Imaging schemes rely on the assumptions that gamma-rays are emitted isotropically from their source and that the flux of the emitter is not significantly distorted from interactions in intervening materials. Despite these assumptions being violated on many different levels, proximity imaging is often a technique for localization or rough mapping to provide an idea of where sources/distributions are located relative to other objects. Fundamentally, proximity imaging requires a set of measurements where the source-detector distance is varied. Absolute and/or relative positioning become important, neither of which are discussed in this section, however the details of this are discussed at great length in Chapter 5.

Assuming that some relative or absolute positioning is given, a simple example is presented in Figure 3.1. Here a point source is located in the center of a plane. A proximity detector system travels the raster pattern in white, and the count rate of the system C_i

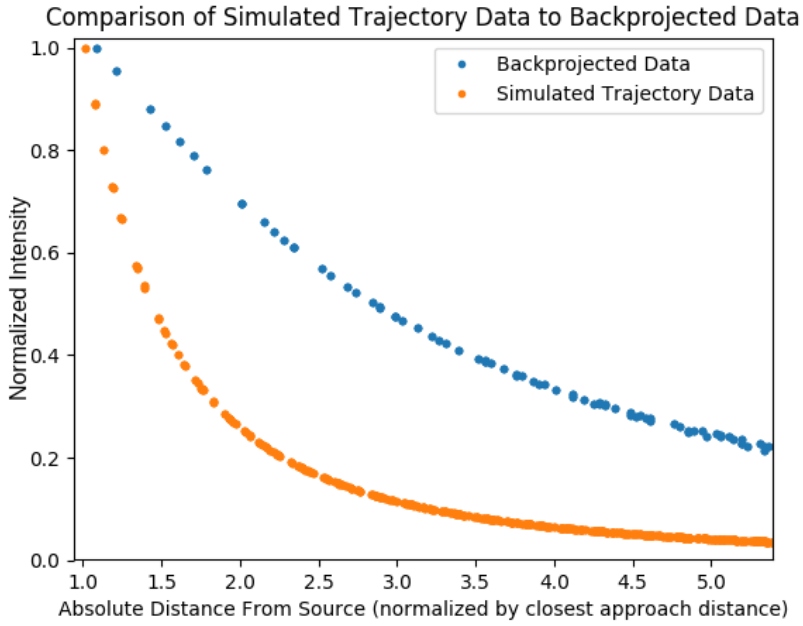

Figure 3.2: Data from the simulated source measurement (Figure 3.1) viewed against normalized distance from the source. The simulated trajectory data represents simply $1/\mathrm{R}^2$ modulation, while the backprojection data represents the intensity at all points in the backprojection grid, $B_j = \Sigma_i B_{ij}$. Both of these data are reported in normalized closest approach distance to the source which was 8 m for both. The point to observe is that the simple backprojection data is broader than $1/R^2$ mapping.

at each measurement i is reported in gray scale from white to black. The sampling of the source at different locations, in this case, only modulates the observed count rate as $1/\mathrm{R}_i^2$, where R_i is the distance from each measurement location to the source. This simplistic model neglects the attenuation, flux distortion and other effects which would contribute to this kind of measurement.

The data from trajectory locations, indexed with i, are aggregated according to backprojection. Simple backprojection is computed on a synthetic grid called the 'model', the properties of which are indexed by j. The model locations often represent physical space where a source can possibly exist. Here backprojection is computed according to $B_{ij} = \frac{C_i}{4\pi R_{ij}^2}$ where C_i denotes counts recorded at trajectory location i and R_{ij} denotes the distance between trajectory location for the measurement at index i and backprojection grid location at index j. The backprojection, computed this way, represents trajectory data weighting onto a regular synthetic grid according to R^2. Again we are neglecting effects of attenuation, and also benefit from the regular sampling of the grid space. Later in Chapter 5 we remove the requirement that the grid must be regularly sampled.

The example presented only emphasizes the distance modulation, however in reality there are flux distortions and attenuation which also provide modulated intensity, even in the point source case. For example, gamma-ray sources embedded in high density materials can create

surface down scattered photon distributions that do not represent the true extent of a source. It is not always possible to reduce the effect of down scattered contributions, and substantial signal can be lost when only specific portions of spectra are used in backprojection.

The fidelity of reconstruction of distributed sources relies on the system point source response, which is broad for simple backprojection, as shown in Figure 3.1. More complicated algorithms for proximity could make use of Maximum-Likelihood Expectation Maximization (MLEM) [61], an iterative method for source reconstruction. MLEM can account for many effects including the system response, sampling biases and can reduce the broadness of the reconstruction at the expense of noise in the image space.

3.2 Compton Imaging

Unlike proximity based imaging, Compton Imaging relies on much more information photon scatter kinematics. Also, unlike proximity imaging, the motion of a detector through an environment may be useful but not strictly necessary to localize sources or distributions[1]. To glean more information about the set of interactions that a single photon has, Compton Imaging detectors must have some position sensitivity and have physical constraints for grouping photon interaction events according to a class type.

COMPTEL is an example of a Compton imager, a portion of the results of that instrument are shown in Figure 3.3. The map estimates the distribution of ^{26}Al in the galaxy, an isotope strongly related with ongoing nucleosynthesis. The angular distribution of ^{26}Al is provided by the directional information encoded in the photon scatters between multiple detectors in COMPTEL. Here, the position sensitivity is derived from several monolithic detector volumes operated in time coincidence for event pairing.

Traditional Compton Imaging

Compton imagers conceptually provide information about incident flux through measurement of Compton scattering physics. The detectors commonly used attempt to provide information about photon scatters through geometric, time and energy constraints such as geometric, time, energy, physical interactions, etc.

Compton scattering is constrained by Compton kinematics. Compton kinematics relies on the electrodynamic exchanges of momentum between a nearly free electron and photon. For scattering with a free electron, the relevant momentum and energy conservation equations can be phrased in the electron rest frame as

$$\vec{p} = \vec{p}' + \vec{p}_e \tag{3.1}$$

$$E = E' + \epsilon. \tag{3.2}$$

A diagram of the Compton scattering process is introduced in Figure 3.5. The parameters $(E, \vec{\Omega})$ represent the incident photon energy and angle of incidence, the $(E', \vec{\Omega}')$ represents an

[1] If one desires more than 2D information at least one more position is required for triangulation.

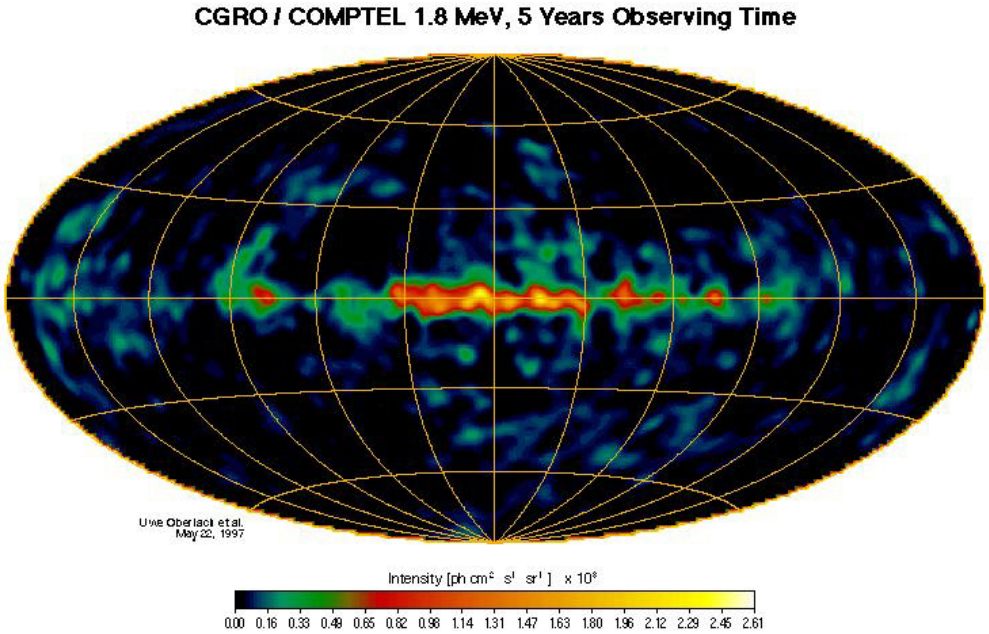

Figure 3.3: The COMPTEL ^{26}Al map of the galaxy and all sky. This measurement was performed by the HEAO-3 telescope with the scintillator based Compton imager over 5 years. Energy and time resolution allows this system to bracket the specific isotope emission related to ongoing nucleosynthesis. Position sensitivity is not inherent in the detectors used, however multiple monolithic detectors with a time coincidence requirement allows for the Compton mode of operation. Figure reproduced from [12].

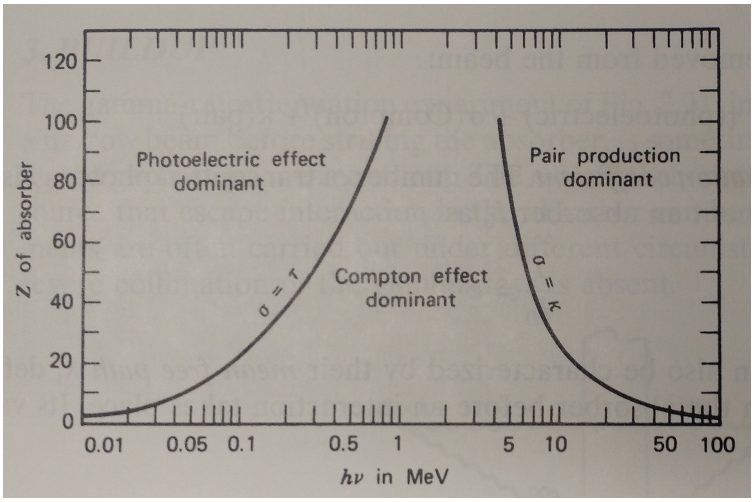

Figure 3.4: Photon interaction cross section trends for many materials and the region where Compton is dominant for that material. Figure reproduced from [37].

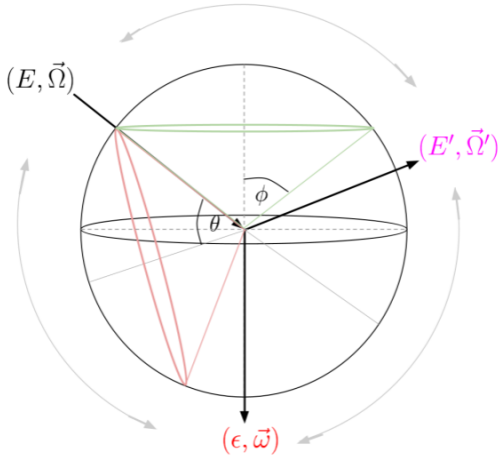

Figure 3.5: The Compton scattering process. An incident photon with energy and direction $(E, \vec{\Omega})$ interacts in the center of the figure, imparting momentum to a free, at rest electron. The photon changes direction and energy according to momentum and energy conservation and is emitted from the interaction with $(E', \vec{\Omega}')$. The electron is emitted with energy and direction $(\epsilon, \vec{\omega})$. These are the so called kinematic quantities to be measured in Compton Imaging. Typically, the goal of Compton Imaging seeks to discover the unknown $(E, \vec{\Omega})$ from measured data permutations of $(\epsilon, \vec{\omega})$ and $(E', \vec{\Omega}')$. The gray arrows on the periphery are indicative of additional constraints to pair interactions in Compton imagers. For example traditional Compton Imaging relies on measured $(E', \vec{\Omega}', \epsilon)$. One attempts to ensure $(E', \vec{\Omega})$ and ϵ are from the same photon by relying on time coincidence. Assuming that the photon scatters only once, losing ϵ of energy and then is completely absorbed, leads to the determination of $E = E' + \epsilon$. The possible directions of incidence are calculated from kinematics, which define a cone of open angle θ about $\vec{\Omega}'$. The cone is shown in red in the above figure.

outgoing photon and $(\epsilon, \vec{\omega})$ is the scattered free electron energy and direction. A frame can be chosen so that the axes of the scatter are in a plane. One can write expressions for (θ, ϕ), the outgoing photon and electron angles with respect to the incident photon momentum vector

$$\frac{1}{E'} - \frac{1}{E} = \frac{1 - \cos\theta}{m}, \tag{3.3}$$

$$\sqrt{\frac{\epsilon}{\epsilon + 2m}}\left(\frac{E + m}{E}\right) = \cos\phi. \tag{3.4}$$

Equation 3.4 above introduces a new variable $m \equiv m_e c^2$, which is energy of the electron only system in its rest frame.

Compton imagers typically take advantage of many of the data permutations listed in Figure 3.5 (perhaps with the exception of $\vec{\omega}$). As an example, time coincident photons can be tracked between two position sensitive gamma-ray detectors. Time coincidence is used as a method for pairing candidate events, while position sensitivity and energy resolution dictate

the ability to reconstruct the scattered photon momentum. Energy thresholding/windowing may be applied in order to increase the number of desired events to false energy-time coincidences. In the case that a photon scatters once in and is then absorbed the scattered gamma-ray defines the axis of a cone with an opening angle of θ defined by equation 3.4. The cone represents the kinematic ambiguity about the scattered gamma-ray axis.

Due to the kinematic ambiguity of the scattering process, one requires many Compton cones to infer incident angular flux from a radioactive stimulus. Coincident summing of the cone outlines produces the source location.

Electron Track Compton Imaging

Electron Track Compton Imagers (ETCI) have the ability to provide denser physical information about the Compton scattering process than traditional Compton Imagers. Specifically, ETCI systems would like to remove the kinematic ambiguities that produce cones in traditional Compton Imagers. This can be achieved by measurement of the scattered electron energy ϵ and direction $\vec{\omega}$, as shown in Figure 3.6. The detectors capable of electron tracking must possess sufficient spatial segmentation to resolve the initial electron track trajectory, while also capturing the full energy of the electron track at decent energy resolution. Event pairing is also required to collect pairs of events in the electron-tracking, scatter detector and the absorber.

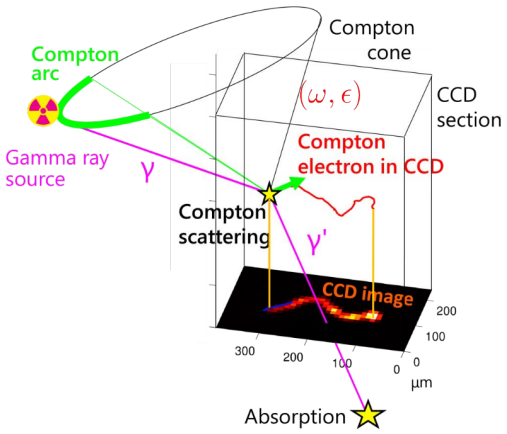

Figure 3.6: Electron Track Compton Imagers (ETCI) cartoon showing the gamma-ray interaction, the scattered Compton electron and the desired condition of gamma-ray absorption in another position sensitive detector volume. Figure from [43].

Equation 3.4 and Figure 3.6 show that the measurement of the electron trajectory $\vec{\omega}$ would reduce the cone ambiguity to an arc segment, bounding the Compton cone possibilities. If the electron track is sufficiently well measured, it is conceivable for ETCI systems to provide enough information that the incident direction and energy of the gamma-ray can be computed from a single event. The direct computation results from the complete kinematic constraint of the Compton scattering problem.

Electron Track Imaging

Electron tracking detectors open a new imaging modality based only on electron tracks. An analytic reconstruction developed by [19] is a method based on an ensemble of track events within an electron tracker. First, the electron track distribution is generated and measured as

$$g(\vec{\omega},\epsilon)=\int_{E_{min}(\epsilon)}dE\int\int d\vec{\Omega}\frac{f(\vec{\Omega},E)}{\sqrt{\epsilon(\epsilon+2m)}}\delta(\nu(E,\epsilon)-\vec{\omega}\cdot\vec{\Omega}). \tag{3.5}$$

An element of $g(\vec{\omega})$ is a set of tracks in $\omega_i \pm d\omega_i$ and $\epsilon \pm d\epsilon$. The input $f(\vec{\Omega},E)$ represents the incident gamma flux distribution. The delta is a choice function for $\{\vec{\omega},\epsilon|\nu(E,\epsilon)=\vec{\omega}\cdot\vec{\Omega}\}$ where

$$\nu(E,\epsilon)=\sqrt{\frac{\epsilon}{\epsilon+2m}}\left(\frac{E+m}{E}\right), \tag{3.6}$$

which was presented previously as $\cos\phi$. The proposed solution is a backprojection of the form

$$b(E,\vec{\Omega})=\int^{\epsilon_{max}(E)}d\epsilon\int\int d\vec{\omega}\frac{g(\vec{\omega},\epsilon)}{\epsilon+2m}\delta(\nu(E,\epsilon)-\vec{\omega}\cdot\vec{\Omega}), \tag{3.7}$$

where the delta is a choice function for $\{\vec{\Omega},E|\nu(E,\epsilon)=\vec{\omega}\cdot\vec{\Omega}\}$. The backprojection, $b(E,\vec{\Omega})$, represents the estimated incident gamma-ray flux in energy and angular space. In order to make the inversion practical, the incident energy must be bound. This is achieved by remapping the $(\vec{\Omega},E)\rightarrow\vec{\mu}$ via the definition

$$\vec{\mu}=\frac{mE}{E+m}\vec{\Omega}. \tag{3.8}$$

The computation is then tractable on the finite interval of $|\vec{\mu}|\in[0,m)$. The mapping produces a function $b(\vec{\mu})$ which can be integrated over a set of measured tracks $g(\vec{\omega},\epsilon)$. A few identities about $\vec{\mu}$ allows one to compute $\vec{\mu}\rightarrow(E,\vec{\Omega})$, which completes the flux inversion based on only measured electron tracks.

The left pane of Figure 3.7 shows the electron track only energy and spatial inversion. On the right pane of Figure 3.7 shows the experimental spectrum recorded for this dataset. Note that the experimental set does not show the photopeak that should be present for ^{137}Cs at 661.7 keV. However, in the left pane, the cluster of points constrains the points in space and energy. The reference [19] gives a much more in depth description of this investigation, such as characteristics of the distribution. The energy of the photopeak from the inversion is estimated to be about 642 keV. The angular resolution and energy reconstruction are believed to be associated with device limitations, not the algorithm used.

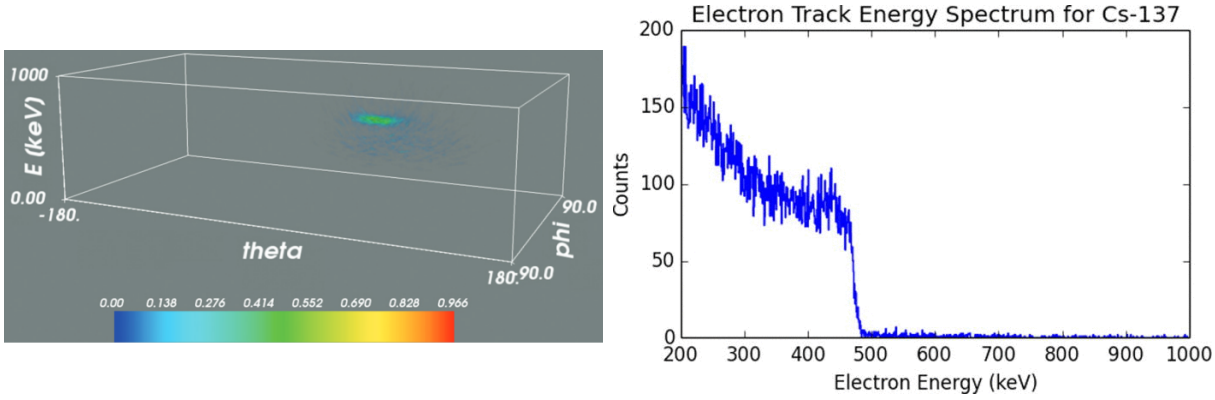

Figure 3.7: (Left) Analytic inversion of electron tracks by [19]. Here the source is found in angular space and the photopeak is partially recovered. (Right) An observed electron energy spectrum from the CCD where no experimental photopeak is observed, also from [19].

Chapter 4

Some Advanced Detector Technologies for Mapping

Chapter 3 presented two modalities for Gamma-Ray Imaging: proximity and Compton. While both of these modalities can be used for Gamma-Ray Mapping, the detectors required for these two modes differ considerably. Detectors used for proximity imaging can be relatively simple and monolithic, while Compton imagers must provide a combination of timing, energy and position resolution. Compton imagers conceptually could provide more sensitivity and specificity for source localization.

Despite the differences in implementations of Compton imagers, Compton Imaging detectors are limited by their ability to measure Compton kinematic products. ETCI detectors could provide unique data to Compton Imaging algorithms through the measurement of the Compton electron recoil. Schematically presented in Figure 3.6, knowledge of the electron track trajectory reduces cones to arc segments, reducing imaging artifacts in Compton cone backprojection. In the limit that the Compton electron tracks can be measured in coincidence with the absorption of the scattered gamma-ray, direct computation of gamma-ray incident momenta is possible on an event-by-event basis.

Substantial problems exist in engineering and science to produce electron tracking systems. Position resolution or generally information density for conventional systems presents a significant barrier to advancement and demands small footprint, high performance electronics. Due to the scaling and physical size, integrated circuits become necessary to preserve the performance characteristics of the devices.

In this chapter, we approach the problem of electron tracking for Compton Imaging. Here we present demonstrations, current approaches, challenges and potential future of Electron Track Compton Imagers.

4.1 Electron Tracking With CCDs

The first demonstration of electron tracking in solid state devices was done in scientific Charge Coupled Devices (CCDs) [60]. These devices are unique in their dynamic range, high spatial resolution ($\sim$1-50μm), low dark noise and significant depletion thicknesses. CCDs were first developed at Bell Labs by Willard Boyle and George Smith; they were awarded the 2009 Nobel Prize in Physics for "for the invention of an imaging semiconductor circuit - the CCD sensor" [38]. A page from Smith and Boyle's laboratory notebook page is presented in Figure 4.1 for the concept of the CCD.

High voltage CCDs were specifically developed as part of the SNAP collaboration to produce 650μm thick, high resistivity devices [21]. Developments in silicon processing [23] and testing allowed for fabrication of 'thick devices'. Fabrication was made possible by gettering breakthroughs and device physics advancements. Improvements in SNAP CCDs contributed to the discovery of dark energy's role in the acceleration of the universe. The 2011 Nobel Prize in Physics was awarded, in part, to Saul Perlmutter for SNAP's devices contributing to the "discovery of the accelerating expansion of the Universe through observations of distant supernovae" [39].

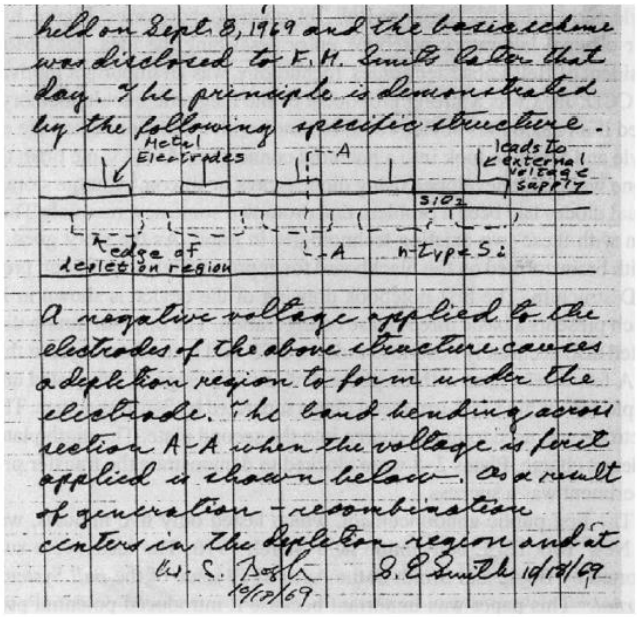

Figure 4.1: Smith and Boyle's notebook entry for the CCD concept. Potential wells beneath metal electrodes are established by fields that are generated via the electrode-SiO_2 interface with a partially depleted bulk. Figure reproduced from [34].

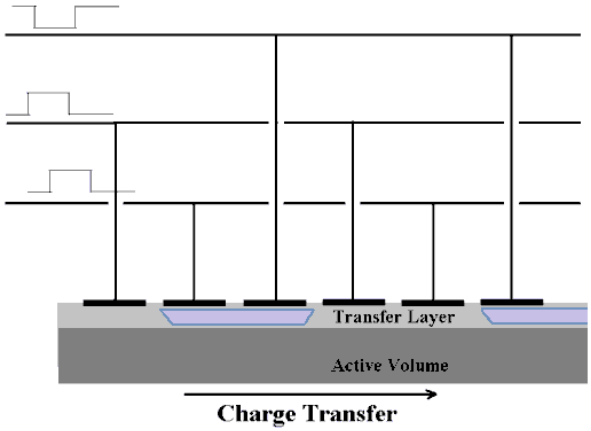

Figure 4.2: A 3 phase clocking scheme to move charges from potential wells out of the CCD. Charge is confined to columns by implants called channel stops. The clock potentials establish virtual rows. Charge can be moved down the column by sequential clocking of the three vertical lines.

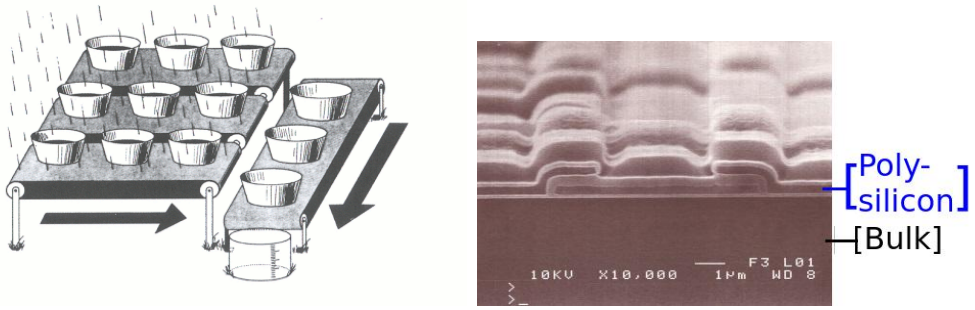

Figure 4.3: (Left) A bucket-brigade charge transfer cartoon, where rain is analagous to charge collecting in physical buckets [27]. The charge is transferred out of the array by clocking as discussed in Figure 4.2. Horizontal clocks move the charges in the last row of the device out to be measured. The measurement device in SNAP CCDs is a floating JFET amplifier implemented outside the pixel region. (Right) A SEM (SEM) photograph of the vertical clock lines in a CCD. Clock lines are metalized polysilicon which are isolated from the bulk and neighbors by SiO_2 field oxide. Shown are the 3 overlapping clock lines needed for charge transfer on the high resistivity bulk. Figure provided by [24].

SNAP CCD Parameter	Typical Spec
Front End Gain ($\mu V/eV$)	2-10
Dark Noise (e^-/sec)	0.25
Read Noise (e^-)	~ 5
Full Well Capacity ($keV - Si$)	90
Dynamic Range (dB)	70

Table 4.1: High level SNAP V3 CCD parameters per pixel.

SNAP Silicon CCDs and Charge Readout

Fully depleted, thick, scientific CCDs were developed at LBNL as part of the SNAP collaboration. The SNAP Version 3 devices were designed with 10.5 μm pitch pixels with depletion thicknesses of about 650 μm. The combination of low dark noise, low read noise, relatively thick depletion layers and large dynamic range make the measurement of electron tracks appealing with SNAP CCDs. Typical parameters for the SNAP V3 CCD are shown in Table 4.1. Listed are the front end charge gain at the digitizer input, a metric for leakage induced noise known as dark noise, a metric for electronic noise known as read noise, the pixel charge well depth in electrons-Si or equivalent noise charge in keV-Si, and typical system dynamic range in the pixel charge well.

The high spatial resolution is especially unique to SNAP CCDs and is achieved through multiplexing. Pixels are defined by potential wells imposed by the 'vertical' clocks and implants known as channel stops. Vertical clocks are those which control movement of charge one row of the pixel array at a time. Charge is confined to columns by the channel stop implants. Transfer of charge is schematically represented in Figure 4.2. SNAP devices rely on 3 phases of clocks to shift charge from one pixel to another. Each pixel has 3 polysilicon electrodes separated from the bulk by SiO_2 field oxide. The right pane of Figure 4.3 shows a view of a partial pixel with three interleaved polysilicon electrodes which are separated by oxide from each other and the bulk of the device. The region just below the pixel plane, in the bulk, is where the depletion region propagates from with applied bias.

Between each vertical clock sequence, there is also a horizontal sequence that moves charge to the 4 floating gate amplifiers, each at a corner of the device. A cartoon is presented in Figure 4.3 in the left pane to demonstrate the charge transfer process. At the end of horizontal registers charge is shifted out into measurement nodes at the corners of the SNAP device. The measurement nodes are gates of on-chip Junction Field Effect Transistor (JFET) source-follower amplifiers. Correlated Double Sampling (CDS) allows for pixel charge to be determined precisely. CDS charge measurement begins with a measurement of the residual charge stored in the measurement node, this charge produces an output level referred to colloquially as the pedestal. A single pixel of charge is shifted into the measurement node and the charge measurement is made again. This quantity is referred to as the signal level. The difference between the signal and pedestal levels yield a voltage difference proportional to the pixel charge.

Figure 4.4 shows the details of the CDS readout from the on-chip floating gate JFET to the output of the preamplifier. In the lower figure, the preamplifier output is shown as channel 1 with the CDS in operation. The important quantity shown is the pedestal subtracted preamplifier signal (labeled in the figure) which is proportional to the charge stored in the well. Also shown is a small set of the digital signals required to operate the CCD. Signals labeled D0-D3 are digital signals related to the operation of the CDS. Channels 3 and 4, respectively blue and magenta, are labeled "H1" and "SW" consistent with the conventions of the LBNL CCD manual [7]. Briefly, H1 is one of the 6 unique horizontal clocks that move charge toward the floating gate JFET, while SW is one of the

four summing well clocks responsible for controlling the transfer of charge from the horizontal register to the floating gate JFET.

The operation of the CCD follows the state machine seen in Figure 4.1. The state machine is presented in a much-reduced form; however, this describes the operational characteristics of the CCD Astronomical Research Cameras (ARC) Owl Application Programming Interface (API) and control system. The nontrivial states have lifetimes which are variable based on the CCD parameters, the readout mode and user settings. For example, the Mini-SNAP V3 CCDs have 1454 x 726 pixels and when readout in the quadrant configuration the clear state has a minimum lifetime of around 200 ms, the exposure time has a minimum lifetime of 1 ms and the readout has a minimum lifetime of about 1 sec. The minimum lifetime of these states dictates the Frame Read Time and thus the limit of timing resolution with this topology of multiplexed pixel devices.

Here we conclude the discussion of the characteristics of the SNAP CCDs and how high resolution 10 μm pixels are readout from the array. The high spatial resolution, in this case, is traded at the expense of the FRT.

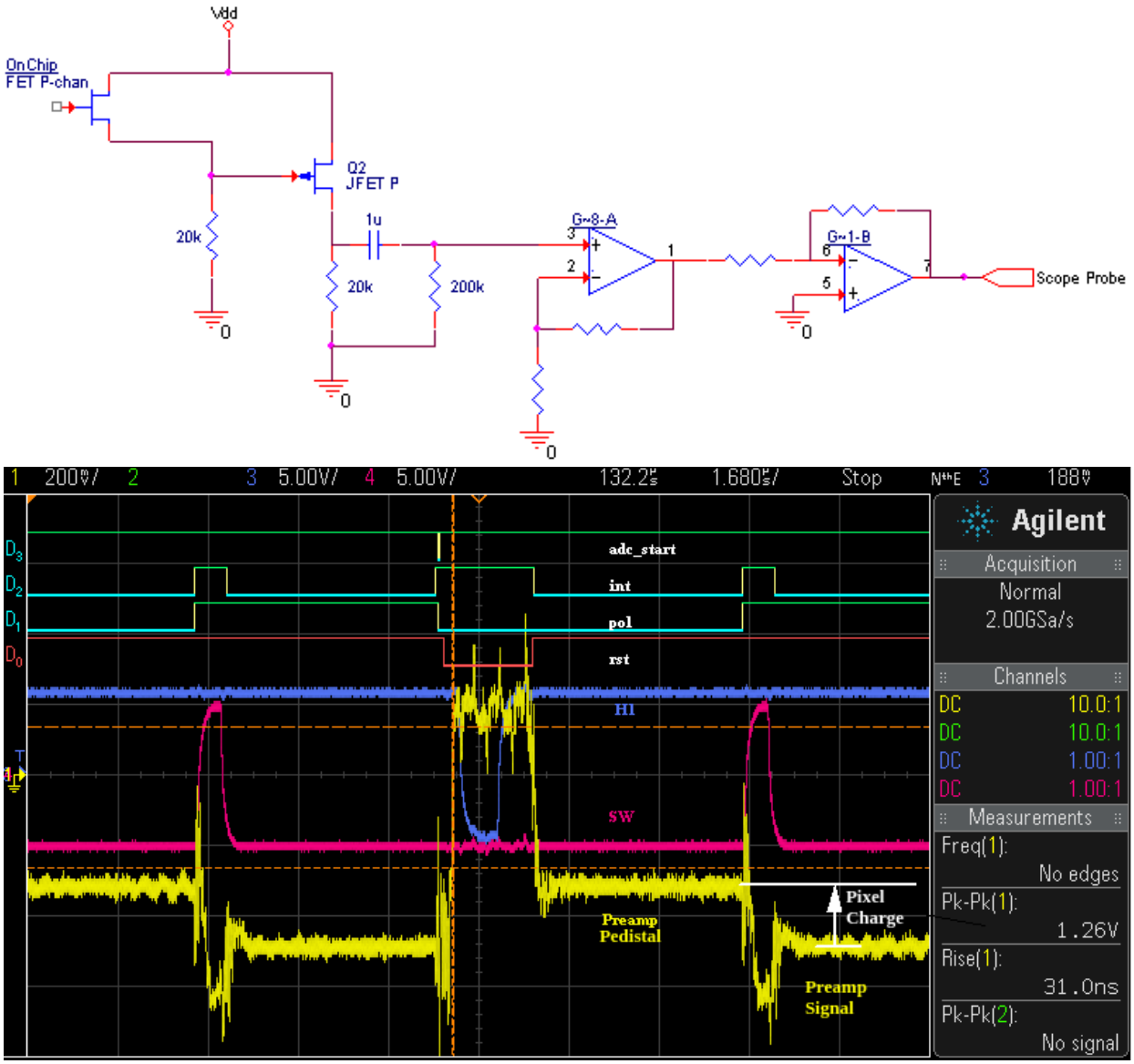

Figure 4.4: (Top) The CCD front end analog signal chain without the floating gate reset circuit. The on-chip floating gate JFET receives charge well packets through clocking of the CCD device. (Bottom) The CDS from pixel readout with the reset and shifted charge voltage levels. Subtraction of the pedistal output and the preamplifier signal yields a voltage level proportional to net charge. Channels D0-D3 are digital clocks that control the CDS sampling. They include a status flag "adc_start" to indicate the start of a CDS sampling, "int" denoting an active low integration period, "pol" indicating the input polarity state, and "rst" an active low reset for the CDS summer. Channel 1 (yellow) is the preamplifier output with the voltage level proportional to pixel charge labeled. Channel 3 and 4, (blue and magenta respectively), are consistently labeled with the LBNL CCD manual and are clocks controlling horizontal charge transfer.

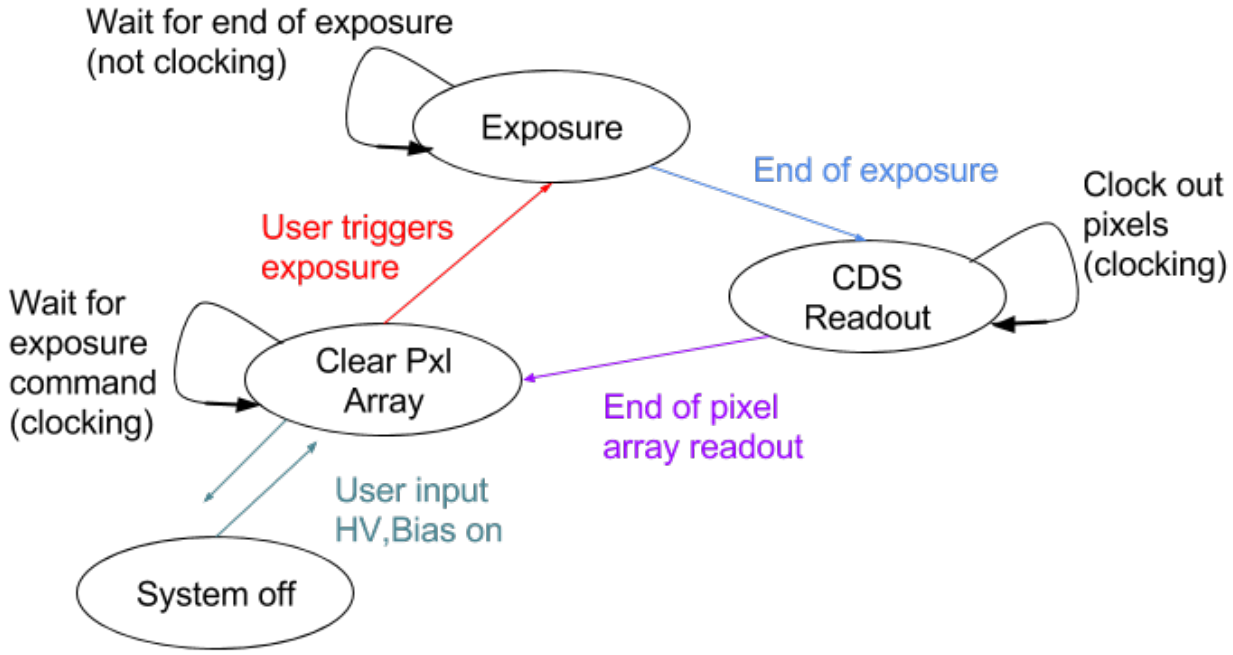

Figure 4.5: CCD state machine for operation of the SNAP devices. The state machine is controlled and implemented by the ARC hardware and firmware. Digitally controlled bias and high voltage are enabled by the user through the ARC Owl API. The transition from **system off** to **clear pixel array** state is initiated by the user, but executes a power on sequence that applies the control and high voltages to the system. Leakage and signal current would collect in the pixel array with bias applied, but is drained by clocking the collected charge out of the array. This state is the **clear pixel array** state or simply the **clear** state. Clocking happens continuously until the user triggers an exposure. The **exposure** state has a minimum exposure time of 10 ms, which is firmware limited. When the user triggers an exposure, the system stops clocking and collects leakage and signal current. At the end of exposure the pixel array is readout through the 4 ADC inputs of the CDS. After readout the system returns to the **clear** state. This state structure has been simplified from the operation of the device, however an important observation is that the clocking of the device occurs whenever the device is powered except in exposure. Clocking prevents device saturation while bias is applied.

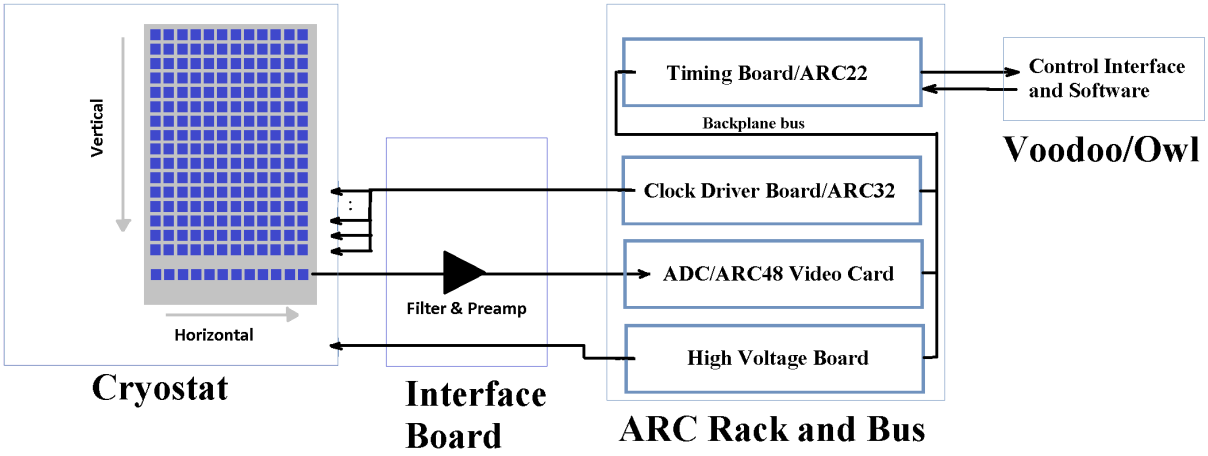

Figure 4.6: Schematic of the ARC readout electronics. There are four areas of interest: the cryostat, the Interface Board (IFB), the ARC Rack and Bus and the Owl software. The CCD is inside the vacuum cryostat so that it can be cooled during operation with feedthroughs for all the digital control lines, the high voltage and the analog outputs. The IFB does some minor clock filtering and signal conditioning and is the mounting point for the CCD preamplifiers. The ARC Rack and Bus contains the electronics needed to operate the CCD. The Clock Driver Board known as the ARC32 buffers clock signals generated by the ARC22 Timing Board. The high voltage board provides substrate bias to deplete the CCD. CDS is performed on the ARC48 Video Card, where pixel signals are digitized. All communication is managed by the Timing Board through fiber optics and is controlled by ARC Owl or the legacy software Voodoo.

Electron Tracking

The 10.5 μm pixelation in the CCD allows for observation of Compton electron track and charged particle interaction. Charge is collected from these interactions in a depleted volume while the CCD is in the exposure state. Liberated charge can be clocked out of the CCD via the schemes in Figure 4.3. Electron tracking has the goal of determining the scattered

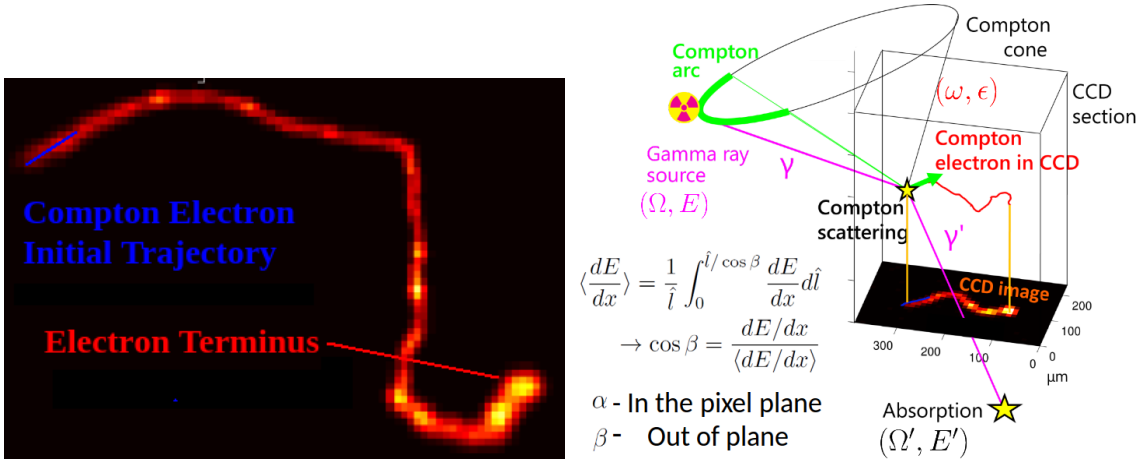

Figure 4.7: (Left) Compton electron track in SNAP 10.5 μm pitch, 625 μm thick CCD at 140 K, 85 V, 1MeV. (Right) Scheme for electron tracking partially presented in Figure 3.6, however note that the CCD projection of the electron track into the pixel plane limits the estimation of $\vec{\omega}$. Therefore, we define α, β as in-pixel plane and out-of-pixel plane components that construct $\vec{\omega}$. β is estimated via a measured projection of the charge in the plane and an expected value from tabulated $\frac{dE}{dx}$. Compton scattering cartoon adapted from [43].

electron direction and energy or $(\vec{\omega}, \epsilon)$. Measurement of $(\vec{\omega}, \epsilon)$ can be made through image processing techniques.

In order to estimate $(\vec{\omega}, \epsilon)$ parameters, the track must first be isolated in a given CCD frame. Isolation is required in order to process the individual tracks, which are from single photon interactions. Binary segmentation is used to separate tracks. The segmentation uses a per pixel median subtracted and thresholded CCD frame as a binary input image [43]. The threshold used for segmentation is typically the blacklevel σ_{bl}. The blacklevel is estimated based on median subtracted pixel distributions and represents the system noise floor on a per pixel basis [34]. The blacklevel σ_{bl} can sometimes be modified by a multiplicative factor for practical or resolution considerations. After separating the tracks in the binary image, the binary electron track image is dilated by a 3x3 image kernel. Essentially, this grows the segmentation region to collect all charge. Small dilation kernels are desired because high S/N ratio in the pixel plane implies that large dilations will quickly degrade the overall S/N. After segmentation and dilation of the track has been performed a simple sum on the region produces an energy estimate or ϵ.

Determination of $\vec{\omega}$ can be done from the segmented image. The initial trajectory is broken down into two angles that can be measured: α, in the plane of the pixels and β out of the plane of the pixels. A convention on β: it is zero in the pixel plane and $\pi/2$ perpendicular to the pixel plane. To select the entire $(-\pi/2, \pi/2)$ range of β, a sign must be determined for $\langle \frac{dE}{dx} \rangle$ by the track diffusion or other properties. The determination of the initial segment bounding box can be made through deposited energy and the track topology heuristics or imaging processing techniques. After the initial segment is identified a small region along the initial segment is used for determination of α and β. The region select at the beginning of the track can be a fixed number of pixels, relate simply to energy, or be based on an extrapolated range tabulated value.

Determination of α, the in-plane angle, is somewhat straight forward. However, the out-of-plane angle lacks sufficient information to be explicitly determined. Difficulty in the measurement of β is due to the fact that the track may be incident on the device with many different values for β; however, all of the information about that angle is compressed by projection of charge in the pixel plane. The compression of charge takes place due to the drift and storage of charge carriers in the pixel plane. One strategy for determining β relies on tabulated values of deposited energy per unit path length $\frac{dE}{dx}$. The tabulated value can be deduced after knowing ϵ. The out-of-plane angle can be estimated by understanding that the projected charge per unit path length can be calculated as $\langle \frac{dE}{dx} \rangle$ from the electron track, over the initial segment. Conceptually, the out-of-plane angle can be estimated by the relationship

$$\cos\beta \approx \frac{dE/dx}{\langle dE/dx \rangle}, \tag{4.1}$$

which follows from a path integral along the initial portion of the track where dE/dx is relatively constant.

Energy resolution for cooled CCDs is quite good, near the Fano limit. However, the limits to which the (α, β) are difficult to determine, but have been demonstrated with a laboratory Compton system exhibiting 60 deg resolution for Cs-137 Compton electrons above 200 keV [43].

4.2 Simulation of Electron Track Response

Up to now we have largely presented important groundwork and select results to discuss the complexity of electron tracking. Now, we focus on our contributions, present simulation results and benchmarks toward the goal of understanding device limits. Simulation of electron tracks is necessary to understand the limits of algorithms, imaging modalities, devices and physics. Electron track simulation must correctly replicate the Compton physics as well as the device characteristics and limitations. Verified simulations are necessary to provide confidence in simulations that compute system ETCI limits. Simulations require high fidelity representation due to the high spatial resolution of CCDs, the limit of 2D information of

the CCDs, the finite range of the electron track, and the limited information on the initial electron track trajectory.

This section presents a classification of Compton electron event types and a simulation of the CCD readout. In the classification, we examine the populations of electron track event types for a few specific cases and provide a simple energy histogram benchmark on the system. The simulation of the CCD readout implements a sparse representation of the charge drift, diffusion and segmentation problem in the CCD; here another benchmark is presented for the spatial distribution of charge in electron tracks. Finally, this section is concluded with some results that were used in the verification of a new electron track only imaging algorithm.

GEANT4 Introduction

The CCDs high spatial resolution of 1-50 μm implies very strict requirements on electron tracking simulations. Tracking down to the 100 nm level is desirable to be significantly detailed in charge deposition on length scales smaller than the pixel pitch. The segmentation threshold and the many delta-rays that may be produced in tracking Compton electrons establish the lower limit to tracking electrons in the simulation. The lower limit of validity should be in the 20 eV-100 eV range.

Generation of Events ANd Tracks (GEANT4) [1] provides a Monte Carlo approach to simulation, particles are tracked down to zero energy with the ability to limit the creation of secondaries through range and energy production cuts. GEANT4 is then an powerful tool for tracking spatially pixelated charge particle detector readouts because the physics information can be mapped externally to detector readout characteristics.

Physics process	Process class	Model class	Recommended low enery applicability limit of model	High enery applicability limit of model	Process name (#)
gamma					
Photo-electric effect	G4PhotoElectricEffect	G4LivermorePhotoElectricModel	250 eV	100 GeV	phot
Compton scattering	G4ComptonScattering	G4LivermoreComptonModel	250 eV	100 GeV	compt
Polarized Compton scattering	G4ComptonScattering	G4LivermorePolarizedComptonModel	250 eV	100 GeV	compt
Rayleigh scattering	G4RayleighScattering	G4LivermoreRayleighModel	250 eV	100 GeV	Rayl
Polarized Rayleigh scattering	G4RayleighScattering	G4LivermorePolarizedRayleighModel	250 eV	100 GeV	Rayl
Conversion	G4GammaConversion	G4LivermoreGammaConversionModel	1.022 MeV	100 GeV	conv
e-					
Ionisation	G4eIonisation	G4LivermoreIonisationModel	10 eV	100 GeV	eIoni
Bremsstrahlung	G4eBremsstrahlung	G4LivermoreBremsstrahlungModel	10 eV	100 GeV	eBrem

Figure 4.8: LLNL Low Energy Electromagnetic Models stated validity range. These meet our simulation requirements well on their stated intervals. Figure reproduced from [18].

Figure 4.8 shows the validity range of the physics for particles and their associated interaction processes. Validity ranges imply lower and upper limits of applicability of a physics package. The limits are important since the tracking paradigm allows tracking to zero energy and range. Validity limits represent a range over which validation experiments and testing

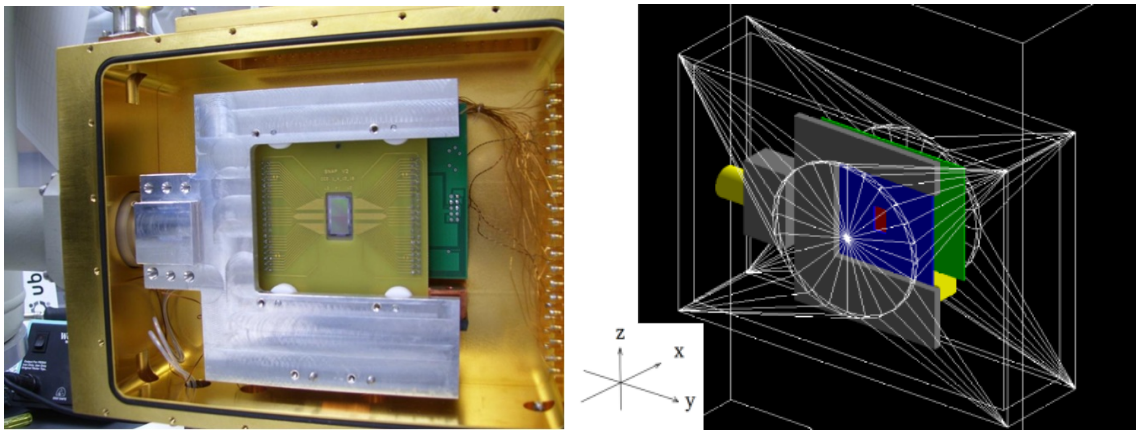

Figure 4.9: (Left) Photograph of CCD inside of cryostat. (Right) Simulation geometry constructed to mimic the CCD setup. Detail in the geometry is required here due to the amount of mass surrounding the CCD. This was a demonstration setup and was optimized for flexibility. The goal here is to understand the event populations inside the device, which can sometimes be affected by the surrounding materials. Further discussion of this is done in presentation of simulation results.

with the physics has been performed. GEANT4 is also open source, making verification, testing and improvements possible.

GEANT4 also provides geometry based optimizations in tracking. Volume nesting significantly improves particle tracking efficiency. This defines a hierarchy which allows complicated volumes to be handled efficiently for tracking. Figure 4.9 provides a comparison of the experimental and simulation geometries. The experimental setup is shown with the vacuum cryostat open on one side. Detailed geometry is needed in this situation due to the amount of detector mass to total system mass that is nearby. The experimental system was designed to be a demonstration stage only, so it was not optimized with this consideration.

Classification and Energy Response Benchmark

Classification was performed to understand the event populations in the electron tracker.

For classification three categories span the events of interest: inscattered, multiple gamma-ray scattered, and Compton electrons. Inscattered events are important due to the high ratio of surrounding mass to detecting mass in Figure 4.9. Inscattered electrons represent photon interactions in the surrounding materials that lead to charge deposition in the CCD. As Figure 4.10 demonstrates there can be observable contributions to the spectrum by these events. Figure 4.10 also shows multiple scatter events above the Compton edge, which in classification are single electrons, but in experiment are multiple Compton electrons. The multiple scattered electrons are not as prominent as other event types, but show that classification is happening correctly for those events above the Compton edge. Compton events that are used for electron tracking can be logically broken down into contained, escape and multiple

scatter events. The classification is possible due to the track information available from GEANT4 simulations. Escape events are defined as electron leakage events from Compton scatters. Figure 4.11 shows the breakdown for this particular scenario. The escape events, in this case, decrease in probability with absorbed energy probably because high recorded energy deposition is a criteria for electrons scattered in containment favorable directions and interaction locations. For example, high energy events near the Compton edge must capture all the electron energy, including the electron terminus. Backscatters occur with uniform probability in along the pencil beam. However, only backscatters that are contained contribute to the Compton edge, escape events will contribute to the lower energy features of the continuum. The multiple scatter region completely accounts for the photopeak and the portion of counts beyond the Doppler broadened Compton edge.

To remove effects of inscattered electrons a pencil beam was directed through a thinned portion of the cryostat wall. The angle selected for intersection on the CCD was about 22 degrees. Simple summing of event deposited energy produced the energy benchmark seen in Figure 4.12. The agreement here is decent, with the most notable disagreement in the multiple scatter region. This disagreement is small, representing less than 8% of events over the entire spectrum, and is logically explained. Multiple scatter in experiment would produce separate electron tracks in the CCD from the spatial segmentation process, however the classification scheme from simulation does not spatially resolve the electron tracks. A readout simulation is needed to account for the multiple scattering region, which is presented later in this chapter. Additionally, a background subtraction was not performed but possibly represents a similar fraction $\sim$ 5% of events. Agreement is seen in Figure 4.12 between simulation and experiment rely only on total count normalization of the two datasets.

CCD Readout Simulation: Charge Transport and Segmentation

The classification analysis presented in the last section lacks the ability to benchmark electron track charge distributions. Additionally, there are other physical phenomenon that the Monte Carlo simulations do not cover such as drift, diffusion, track fragmentation, etc. The effects are related to the readout of the charge information on the CCD pixel plane. Processing the track information requires simulation of the readout for each energy deposition to the lattice by an electron track. Specific focus here was directed at drift, diffusion and segmentation.

Drift and diffusion were simulated through a linearly ramping electric field from the CCD backside to the pixel plane. An analytic solution for this case has been developed by [42]. In the specific case of the n-type SNAP CCD hole charge transport was simulated. The initial charge cloud size at every location of energy deposition along the electron track was modeled according to a semi-empirical model, the model is supported by verification on Scanning Electron Microscopy images [33]. Energy depositions only occur along the track if secondaries are above the production cuts. Existing particles track to their at-rest state, where they are "killed", in GEANT4 terminology.

A sparse segmentation was implemented for the efficiency of the simulation at small pixel sizes. Electron tracks produced by GEANT4 were drifted and diffused to the pixel plane.

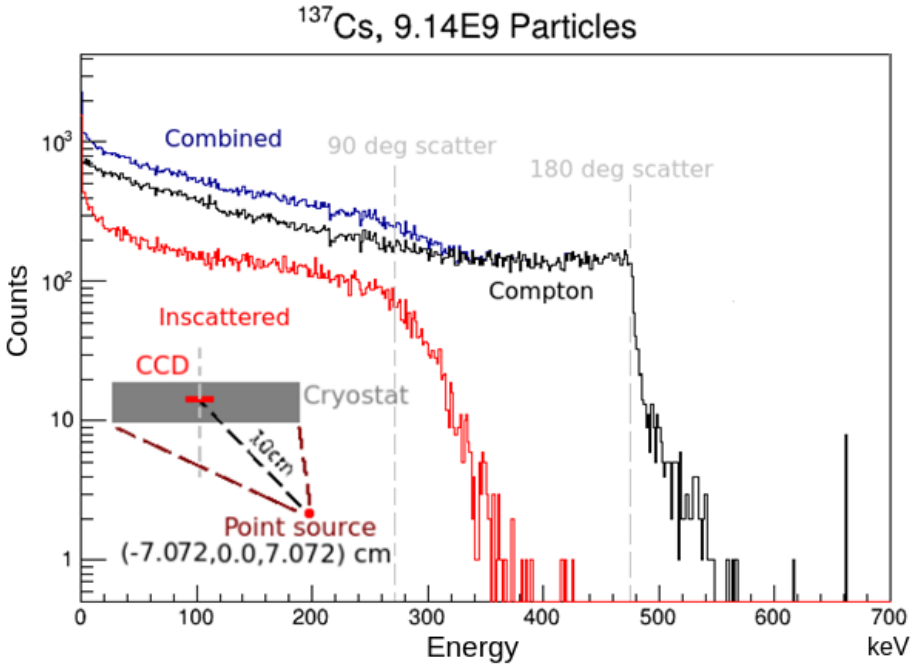

Figure 4.10: GEANT4 simulated results of a source detector configuration that highlights the inscattered electron component from a source of 661.7 keV gamma-rays. This source represents ^{137}Cs. In grey the 90^o and the 180^o photon scatter energies from ^{137}Cs are shown. The source is a 4π emitter. Overall it is interesting to observe that the spectrum differs significantly from Figure 4.12, as the source and geometry are slightly different. This effects the event populations in the CCD, especially the inscattered electrons in this case. Inscatter electrons are nearly indistinguishable from Compton electrons in the experiment with only the CCD.

If a pixel contained charge, it was added to the sparse pixel plane map. Connectivity was determined by a spanning tree across the pixels in the diffused plane. Compton electron tracks can then be generated. Figure 4.13 demonstrates a few drifted and diffused electron tracks. In the case of multiple gamma scatter from a single photon, depositions are spatially separated via segmentation as shown in Figure 4.14. Segmented electron tracks would be added to the spectrum as separate entries in the event histogram. Segmentation spatially resolves these tracks because they are not spatially coincident. Finally, we show that it is possible to demonstrate an electron track distribution benchmark in Figure 4.15. The energy per unit area is computed for each track in the simulated spectra and is binned accordingly. Experimental data are compared with this. Interestingly a low energy shoulder exists in the simulated events, which appears blurred by the experimental spectrum. Classification shows that this shoulder is almost completely attributable to escape electron tracks, those events which do not capture the electron track terminus. As seen in Figure 4.7 and Figure 4.13, the terminus contains a large amount of charge over a small area.

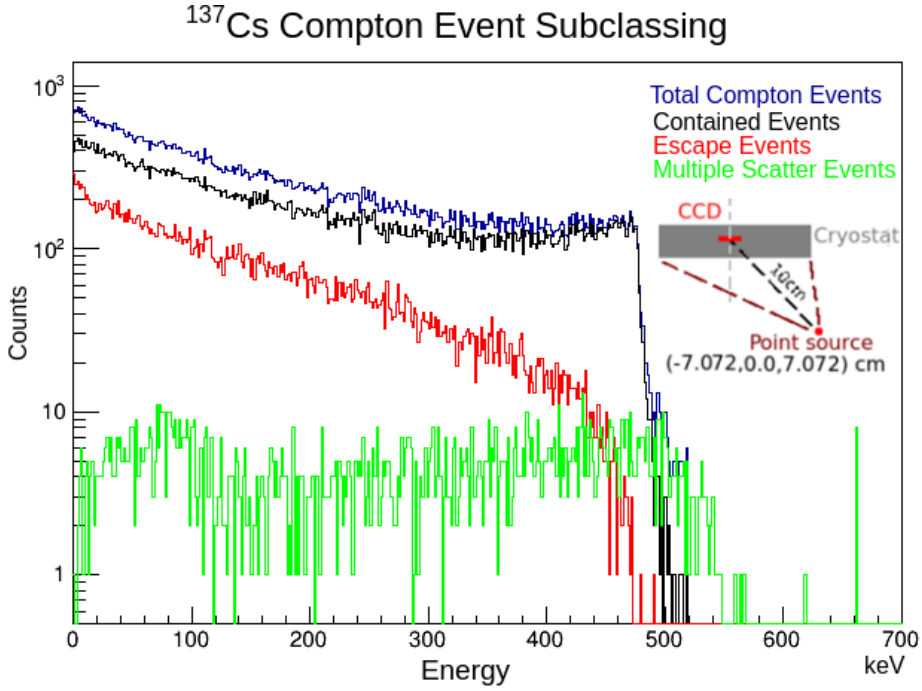

Figure 4.11: GEANT4 simulations with classification used for determination of event populations for events within the CCD from 661.7 keV gamma-rays. There is an interesting trend in the number of contained events approaching the Compton edge, in that electrons which deposit large amounts of energy are likely to be contained. A large fraction of the total energy is contained in the electron terminus, which is localized in deposition. Multiple scattering is a very small fraction of the total events in simulation, on the order of 5-8%. In experiment the spatial segmentation reduces these interactions to single tracks. The classification does provide some insights but is not sufficient to replicate many of the device level properties.

Conclusion

Simulations were performed with GEANT4 to produce high fidelity benchmarks for both energy and track distributions in a demonstration setup. The goal of these simulations was to investigate event populations and obtain benchmarked track data. The benchmarked track data provides unique insight to single events within the CCD. Track data allowed analysis of the limits of a new electron track only imaging algorithm developed by [19]; a few results of that development are shown in Figure 3.7. The simulation data assisted in showing that the image reconstruction presented in Figure 3.7 was device limited [19]. The data comes from simulated electron tracks produced by classification and segmentation, which is necessary for understanding the device limitations.

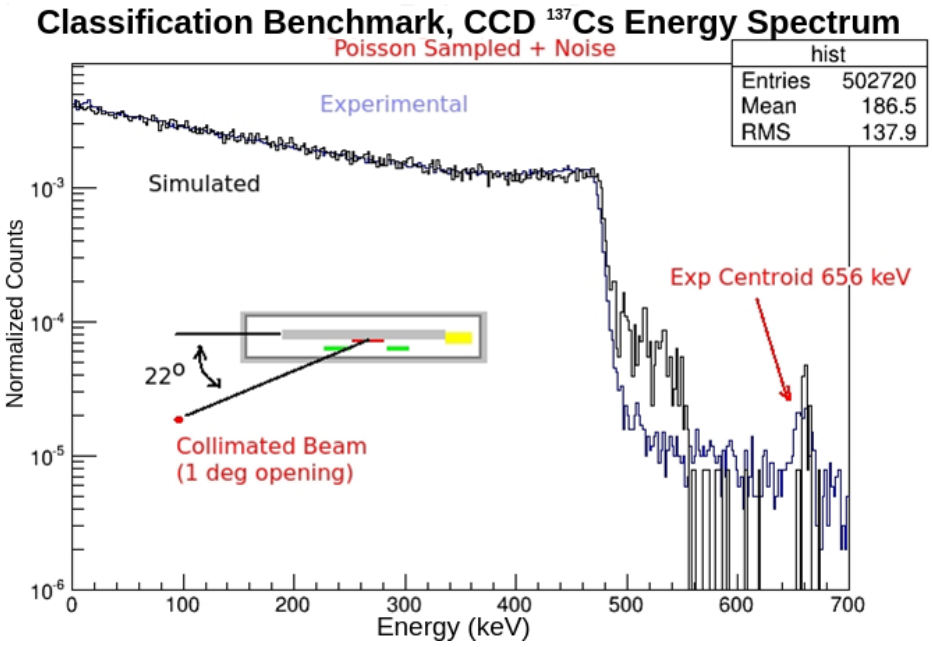

Figure 4.12: An experiment and simulation for benchmarking the energy response with the physics package from Figure 4.8 with energy and range production cuts of 100 eV and 10 nm was performed with a collimated ^{137}Cs beam with 1^o opening angle. The results from simulation are normalized to total counts in each spectrum. One should note the multiple scattering region between the Compton edge and the photopeak. The multiple scatter region is present in experiment because the classification does not delineate between tracks which are spatially separated, it only considers the event deposited energy and that it was a Compton event.

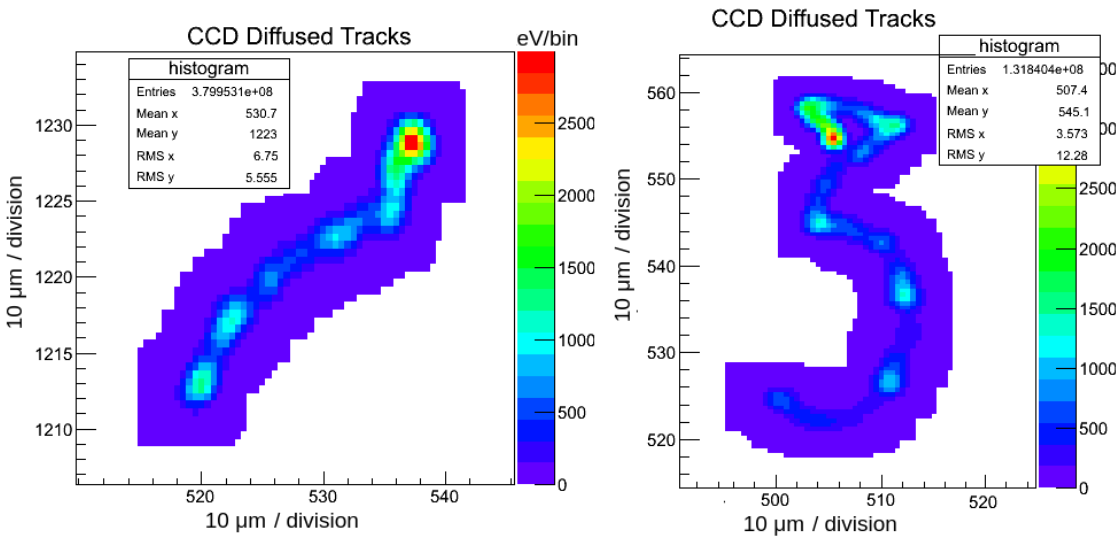

Figure 4.13: (Left) A simulated 241 keV Compton electron track in silicon diffused to the CCD pixel plane. (Right) Another simulated Compton electron track but at 417 keV. High angle scatters can either be nuclear or electronic. In the case of low energy deposition these are likely nuclear scattering. Both tracks are shown without blacklevel noise and at 10 μm pixel pitch.

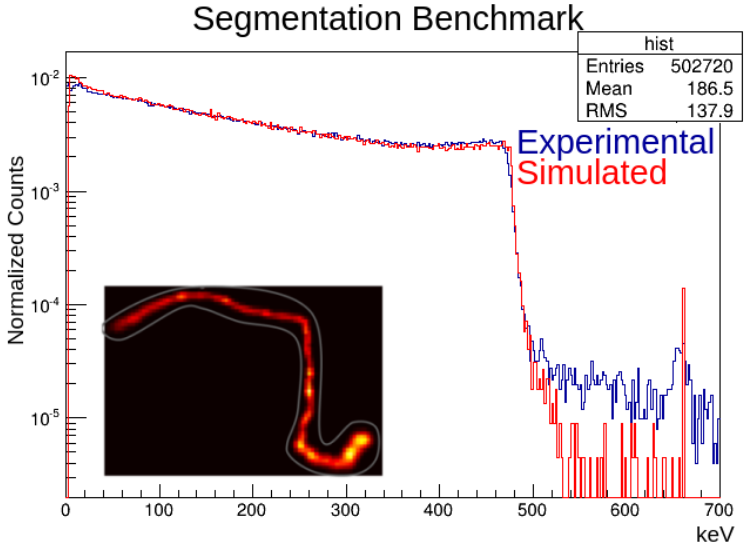

Figure 4.14: Segmentation of experimental and simulated electron tracks. The inset is an experimental track. Simulated tracks were produced and processed with 10 μm pixels and $\sigma_{bl} = 20$ eV. Simulation of the readout removes the classification approximation presented in Figure 4.12 as can be seen in the multiple scattering region. Normalization is applied via total counts. Poisson sampling should be included for the complete response, which makes the spectral features sharper than experiment. The experimental measurement has the same geometry as presented in Figure 4.12.

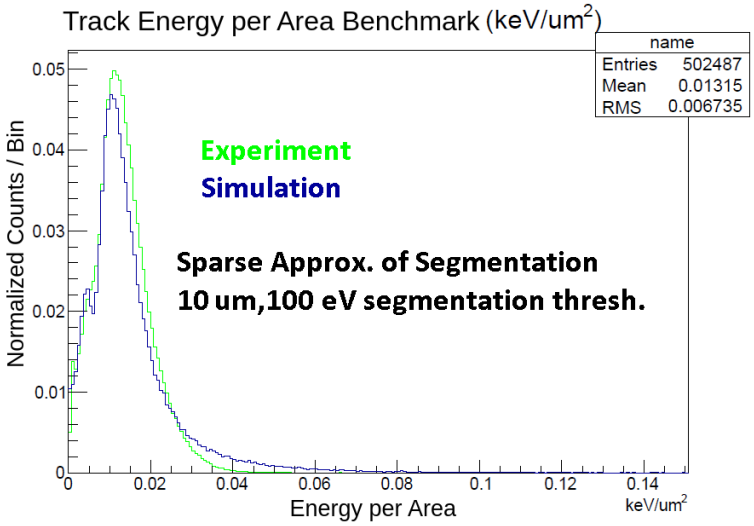

Figure 4.15: Benchmark histogram for track energy per area with data from Figure 4.14. The agreement is decent here, with some deviation at the apex and near the tail of the distribution where energy per area is overpredicted in simulation. In the simulated data there is a shoulder near low energy. In the experiment, the shoulder is blurred by the detector physics. Investigation of the shoulder indicates that almost all events are escape events that do not capture the electron terminus and thus have lower total energy per unit area over the entire track.

4.3 Potential and Progress Toward ETCI with CCD-Strip

Complementary to the goals of simulation, algorithm and limits evaluation, there are some practical issues with the operation of CCD Compton imagers which have so far been neglected. These issues are fundamentally related to the lack of time resolution in the CCD multiplexing scheme. The readout architecture restricts the integration of CCD electron trackers in conventional Compton imagers. Moreover, they are limited in use for more general imaging applications which require time correlation with external sensors.

In the following, we outline the limits of current CCD systems, propose CCD-strip as a way to circumvent some of these problems and report on the current state of this work and the challenges that still exist.

Multiplexed Time Resolution Limit: Frame Read Time

The multiplexed CDS scheme for pixelated sensors reduces readout complexity and channel density. For CCDs the time resolution is constrained to the FRT. The frame read time is

$$\text{FRT} \quad \sim \quad (n_c n_r \tau_r)/n_{amps}, \tag{4.2}$$

where n_{amps} represents the number of amplifiers on a device, n_c and n_r are the number of columns and rows on the device, and τ_r is the period of row/horizontal transfer registers described in Figure 4.3. The FRT for the SNAP V3 generation have horizontal clock periods on the order of 8 μs (see Figure 4.4). This implies an FRT of about 1 sec/MPxl. Equation 4.2 assumes zero exposure time. For Compton Imagers, the FRT as a time resolution of the CCD is practically infeasible for coincidence windows, additionally scaling the device area trades in time resolution. Faster clocking and the concept of column parallel CCDs is a multiplexing scheme that increases the number of amplifiers. The evolution of the multiplexing architecture can provide smaller FRTs and these are under investigation for other applications [10]. Unfortunately, the time resolution achievable in multiplexed architectures of this time will be bound to the horizontal clock period and does not address the FRT scaling with pixel density.

CCD-strip Proposed Solution

To overcome the limitations in multiplexed CCD architectures, CCD-strip was proposed. This concept is presented in the right pane of Figure 4.16. The CCD-strip design circumvents the FRT by applying metal strip electrodes to the CCD backside with strips parallel to the horizontal registers. Conceptually, this could provide time resolution on the order of the liberated charge drift time via the strips, while maintaining high spatial resolution on the pixel side. Backside strips would be instrumented with conventional, continuous reset CSAs

CCD-Strip Parameter	Nominal
$V_{depletion}$ (V)	40
ρ (kΩ-cm)	$\sim$20
C_{dep} (fF/strip)	402
C_{ss} (fF/strip)	582
Pitch (in pixels)	35
Gap (in pixels)	5

Table 4.2: Parameters for the CCD-strip devices.

to record charge induction from carrier drift. Electron tracks, collected on the pixel plane, could be correlated with the strips by spatial coincidence (left pane of Figure 4.16). The strips could provide time stamps of recorded charge arrival to the backside. This scheme requires double sided processing to produce CCD-strip devices.

There are significant challenges associated with the fabrication of CCD-strip devices. Specifically, the strips require submicron alignment with the pixel plane and double sided handling/fabrication processes. Processes are typically optimized for one sided processing in semiconductor fabrication facilities. High fixed cost and the general risk to other wafer processes is often prohibitive to retooling manufacturing to provide double sided processing. Electrostatic Discharge (ESD) sensitivity and process incompatibility (temperature, materials, etc.) also present significant challenges. ESD sensitivity is a result of small feature sizes, in particular, the thin 100 nm thick dielectric region between the clock lines and the bulk of the device present a shorting risk. Small feature sizes like this imply high fields for relatively small amounts of differential charging. Intellectual Property (IP) of different fabrication facilities must also be taken into consideration as different sites have different strengths.

In light of the listed constraints, devices were fabricated according to Figure 4.17. DALSA provides expertise in fabrication of the LBNL SNAP CCDs on high resistivity silicon. The collaboration with the LBNL SNAP group provided controls for producing high yield quantities of high performance CCDs. SINTEF provides expertise in strip detector fabrication with the capability of doing double sided processing with submicron alignment. Fabrication was done at these two fabrication facilities: Teledyne DALSA (DALSA) and SINTEF Research (SINTEF), while the LBNL SNAP group provided designs for CCD detectors and the strips were specified by our CCD collaborators. The design, while presented in this work, was not the work of this author. An attempt to cite those sources is done in the relevant figures.

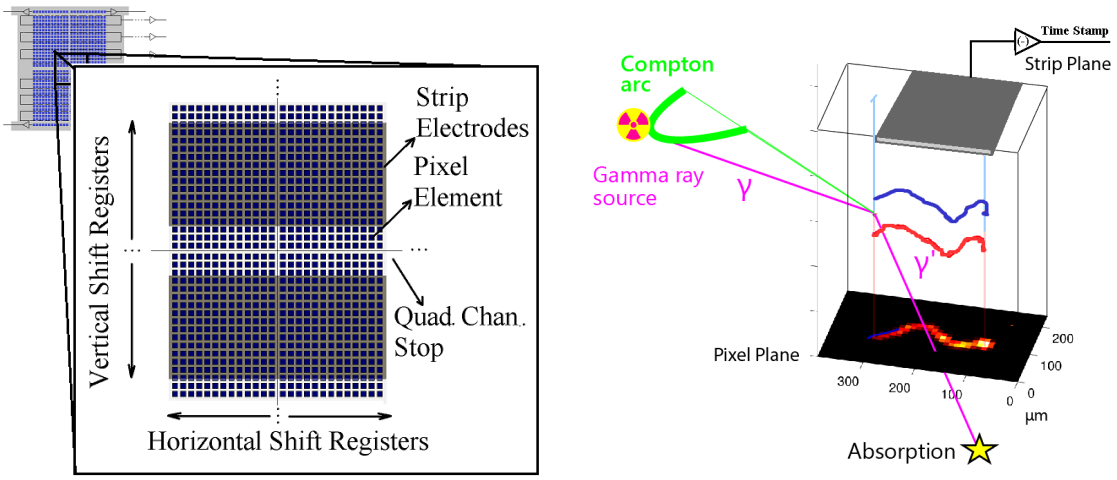

Figure 4.16: (Left) A top-down schematic of the CCD-strip concept, demonstrating the pixel-to-strip mapping of the topside pixels and the backside strips. Here aluminum strips are applied to the device backside to provide event time stamps during CCD exposure. These time stamps can be spatially coded by strip channels through a strip-pixel registration, the goal being that strips would correspond to a set of pixels. If an electron track was captured in the pixel plane the track could be time stamped by the corresponding strip signal. This method does not guarantee uniqueness; in reality many time stamps could be generated during a CCD minimum exposure period. If many tracks overlap the same strip, one needs to rely on energy to discriminate. However, energy is only resolvable if the events fully collect on that strip and are farther apart in time than the drift times of the carriers involved. (Right) A Compton event within the CCD-strip bulk where electron-hole pairs drift toward the strip and pixel planes. Time resolution on the order of the charge drift time in the bulk is expected, while maintaining high energy and spatial resolution of the CCD electron tracker.

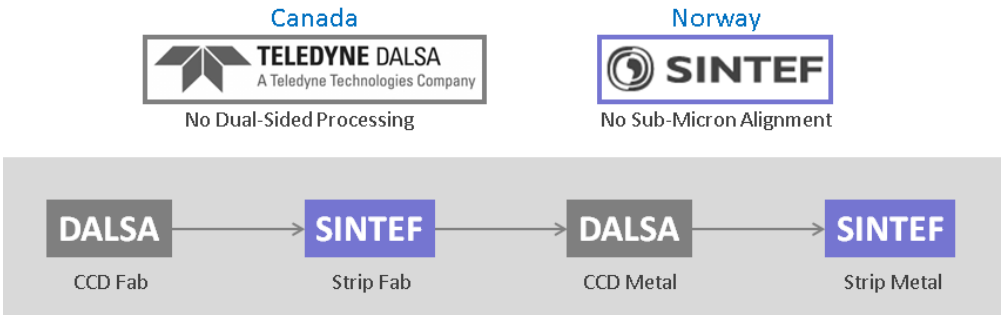

Figure 4.17: Coordination for fabrication of CCD-strip devices. Fabrication was performed at both DALSA and SINTEF. These two provided complementary capabilities of CCD expertise, submicron alignment technologies, strip detector expertise and dual sided processing. The metalization step was split between the foundaries due to process and temperature considerations.

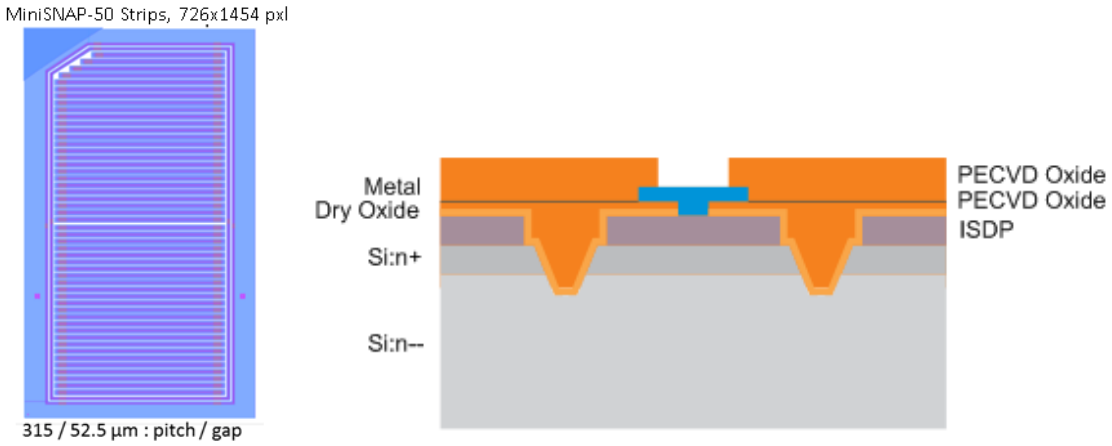

Figure 4.18: CCD-strip design layout and fabrication process from [4]. (Left) Strip design for Mini-SNAP CCDs with 50 strips that have a pitch of 315 μm. This implies about 35 vertical pixels per strip with strips that almost span the horizontal register of the device. Two guard rings are present to sink surface leakage current which is typically one to two orders higher than the bulk leakage. (Right) A cross-section of the backside strips. PECVD oxide was used for building inter-strip isolation channels. The metal region (blue) was aluminum applied to n+ material for the ohmic contact to the n– bulk.

CCD-strip Implementation

Ten 6 in 20 kΩ-cm n-type silicon wafers were used to implement the CCD-strip devices. DALSA Semiconductor began processing of the CCD elements of the devices which were passivated with SiN on the pixel plane to prevent scratching while processing the wafers face down for strip processing. Wafers were then sent to SINTEF for the strip masking and polysilicon doping. SINTEF removed the SiN passivation layer to open bond pads and returned the wafers to DALSA for CCD metallization. Finally, the aluminum strips were applied at SINTEF. Two wafers were held for future processing at SINTEF.

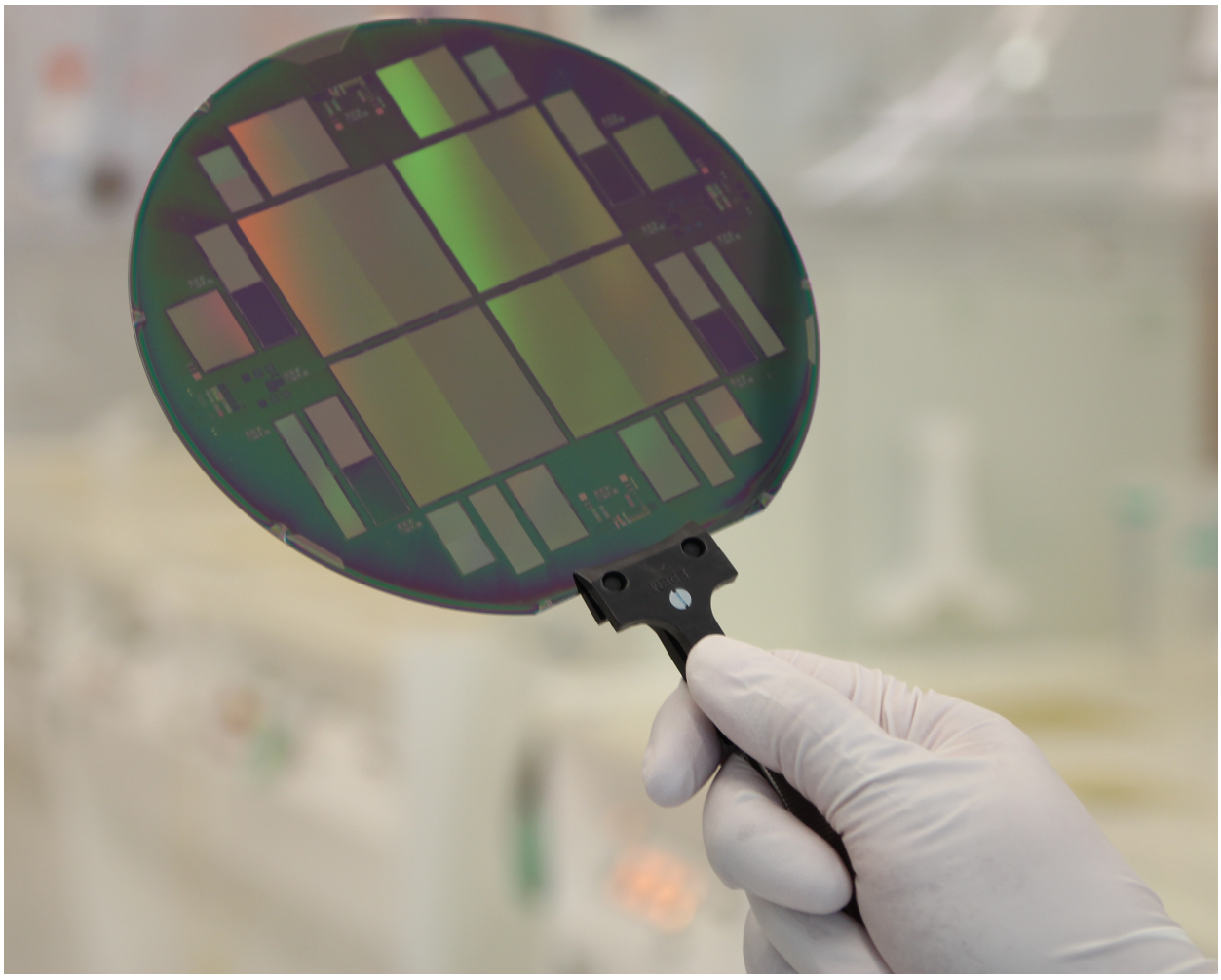

Figure 4.19: CCD-strip wafer photo from a SINTEF cleanroom. Figure provided by [49].

Wafers from batch 145714.3 numbered 9, 10 and 11 were processed by DALSA as controls, these were returned to LBNL. CCD-strip wafers from batch 147514.4 numbered 3, 4, 6, 7 and 8 were processed by SINTEF. From this batch 8 was not given alignment patterns on the backside by DALSA. This wafer was a SINTEF control but could only be handled up to the plasma etching step at SINTEF. The function of the plasma etch was to remove

the polysilicon and dieletric stack, normally on the backside of CCD devices. Temperature control at this step was difficult due to SINTEF's inability to clamp the wafers without risking height variations on the backside during photolithography. The lack of temperature control caused reticulation of photoresist in subsequent processes, making the strip alignment and processing in general difficult. UV inspection of the wafer surface was performed at SINTEF after all process steps; however, significant distortion was present due to the unpolished strip side of the wafer, as shown in Figure 4.20. Polishing was not possible due to concern for the CCD side of the device. After SINTEF completed processing strip implants, the devices were passivated and sent back to DALSA for application of CCD metal. Finally, the devices were sent to SINTEF to apply strip electrodes and CCD-strip devices were sent back to LBNL for testing.

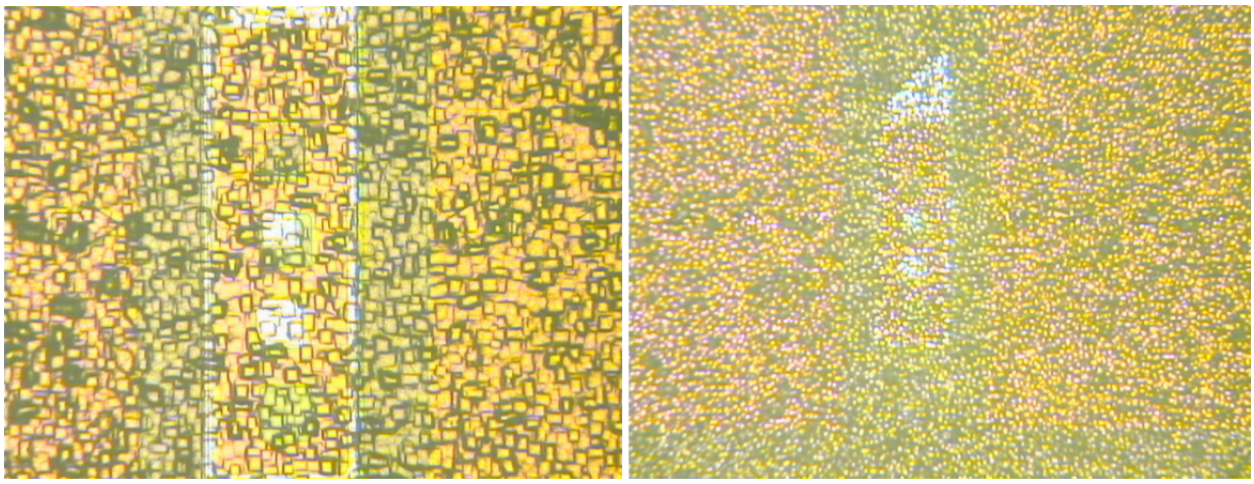

Figure 4.20: Microscope view of the strip side alignment marking for strip-pixel alignment during SINTEF lithography steps. (Left) The original alignment mark, the light band in the middle of a slightly darker background is the reference for alignment of strips during processing. The unpolished nature of the strip side of the device provided difficulty in identification of alignment marks. (Right) The alignment mark cross-hair zoomed out. In subsequent lithography steps alignment marks became very difficult to view due to increased surface roughness. Figure from SINTEF CCD-report [49].

Probing of wafers was done for wafer screening and dicing quality control by our SNAP collaborators. A few results are shown for posterity. The wafers were flying probed on an engineering test stand in the SNAP research group at LBNL. Testing is automated and is routinely performed at -45 ^{o}C or -65 ^{o}C with different substrate (ohmic) contact voltages V_{sub}. A complete summary of the probing is out of the scope of investigation, however we present the results of two different CCD-strip wafers in Figure 4.21. The left pane in Figure 4.21 shows a wafer with overlayed images of a 60 sec CCD exposure. This wafer has a significant number of clock shorts and overall grainy images due to elevated dark noise. The second wafer, shown in the right pane of Figure 4.21, shows a 60 sec exposure from devices that is flatter with overscan regions visible at the shared quadrant boundaries. Wafer 147514.4 #3

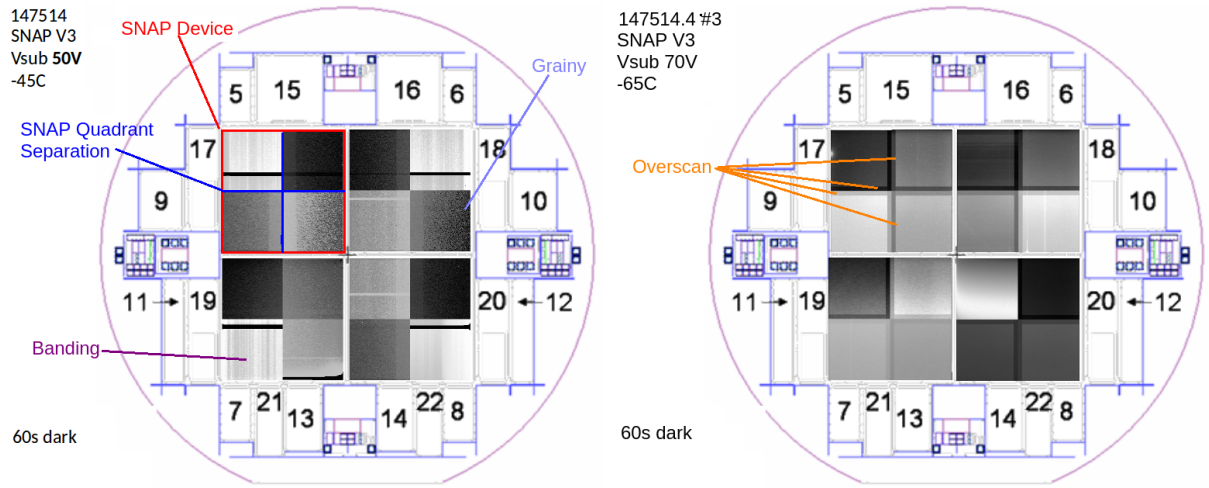

Figure 4.21: Wafer screening and cold-probe testing in the SNAP CCD engineering test stand at LBNL, performed by [25]. (Left) Example test wafer with individual devices labeled. The large format SNAP V3 devices show a single 60 sec exposure. These test wafers of CCD-strip devices show severe clock shorts showing as vertical columns in select quadrants. Grainy quadrants are those with elevated black noise, while vertical banding, in this case, is related to charge injection from clock shorts. (Right) Probe of 147514.4 numbered 3 on the engineering test stand at higher applied bias and lower temperature. This appeared to be the best wafer where devices are essentially free of clock shorts. Device leakage is still much higher than expected.

produced the first CCD-strip electron tracks (see the left pane of Figure 4.23). This was the most promising wafer tested of the CCD-strip batch in terms of dark current and uniformity.

Mini-SNAP devices were extracted from wafer 147514.4 #3 and 145714.4 #9. These wafers are CCD-strip and DALSA control wafers respectively. Engineering at LBNL diced the wafer so that devices could be tested individually. To have maximum flexibility and capabilities, a variable temperature cryostat was constructed to demonstrate the operation of the CCD-strip devices. A new cold finger attachment was designed along with Heat Spreader Bar (HSB) for a controlled thermal link to the liquid nitrogen dewar. Test devices were mounted in the cryostat, thermally linked to the cold finger via the HSB and Picture Frame Board (PFB). The PFB also provides mechanical support and has connectors for the feedthrough pigtails. The pigtails bring in signals necessary for the CCD-strip system to operation. Figure 4.22 shows a Mini-SNAP V3 from a DALSA control run mounted in the cryostat. The dewar and cyrostat in our configuration share a vacuum, which was optimally pumped to about 1E-6 mBar using a turbomolecular pump. The heat load in this configuration mostly radiative. Two small 50Ω heaters were attached to the HSB to provide an operational range of 120-200 K. Heat loads could be adjusted by varying the number of copper shims connecting the HSB to the mount/cold finger.

Vacuum feedthroughs provided access to two temperature diodes, heaters, bias lines for

CCD operation, clocks for shifting out charge, bias voltage and signal lines that are required for CCD and strip operation. These were individually routed in vacuum through 2 64 pin pigtail connectors.

Electronics for this setup were from Astronomical Research Cameras (ARC). This semi-commercial set of electronics provided the basic functionality required to readout the CCD. The components of the system can be seen in Figure 4.6. Preamplifiers, the IFB and the LBNL high voltage board were assembled by hand. Operation was verified and tested. Firmware was flashed to both the timing board and the high voltage board. We requested the ARC48 Video Card documentation from ARC; unfortunately, the hardware version we had was undocumented. We reverse engineered the ARC48 Video Card bit addressing scheme from previous versions of the ARC48 schematics and physical part numbers on the board. Parts of the assembly failed to use address registers provided on the backplane, which would previously change voltages set by the high voltage board. Additionally, upon first operation of a test CCD a banding and inverted pattern appeared on the device (right image of Figure 4.23). This problem was two fold: the integration period in the Digital Signal Processor (DSP) did not properly bracket the clock injection in the CDS and the ADC did not have the proper polarity configuration. These manifestation of these two problems were in an inverted intensity image and in intermittently saturated rows at regular intervals in the CCD image. The banding was similar to an aliasing effect.

Figure 4.23 in the right pane shows the corrected operation of the CDS with the test device in the new cryostat. Additionally, the right pane in Figure 4.23 shows nominal operation and spectral resolution expected of ^{241}Am stimulation. Measurement of the black level noise is a very sensitive metric for pixel plane performance when resolution is difficult to measure. Black level noise is quoted as FWHM/pxl. This value is much easier to measure than photopeaks, largely because photopeak efficiency for gamma-rays is very small in CCDs. Because the device under test is a DALSA control CCD, bias is applied through the CCD topside bias implant. Leakage current is sinked through a ohmic path along the side of the device to apply positive high voltage to the backside. Leakage currents measured were quite large as Figure 4.25 shows, as a result exposure times were limited to less than 1 sec. Over the 1 sec exposure periods, the device will reach saturation of the pixel wells. CCD-strip devices would likely not require long exposure times. However, it is indicative of the device state and performance. Higher leakage leads to larger contributions from dark noise. The minimum achievable exposure time for this system is 1 ms.

The DALSA control device showed that pixel plane operation for exposures of 10 ms produced spectral resolution comparable to previous CCD electron tracking devices. The leakage current, however was as much as 1E3 times larger than typical devices [47]. Saturation of the pixel wells was seen in large areas of the device and appeared to be uniformly distributed, however in this revision of the test stand we did not have an integrated way to perform extensive leakage current tests. Additionally probing certain areas of the device was not possible due limitations in input impedance of the voltage probes. Therefore, the exact origin of the device leakage could not be determined.

After first acquisition of electron tracks in our cryostat and demonstration of some

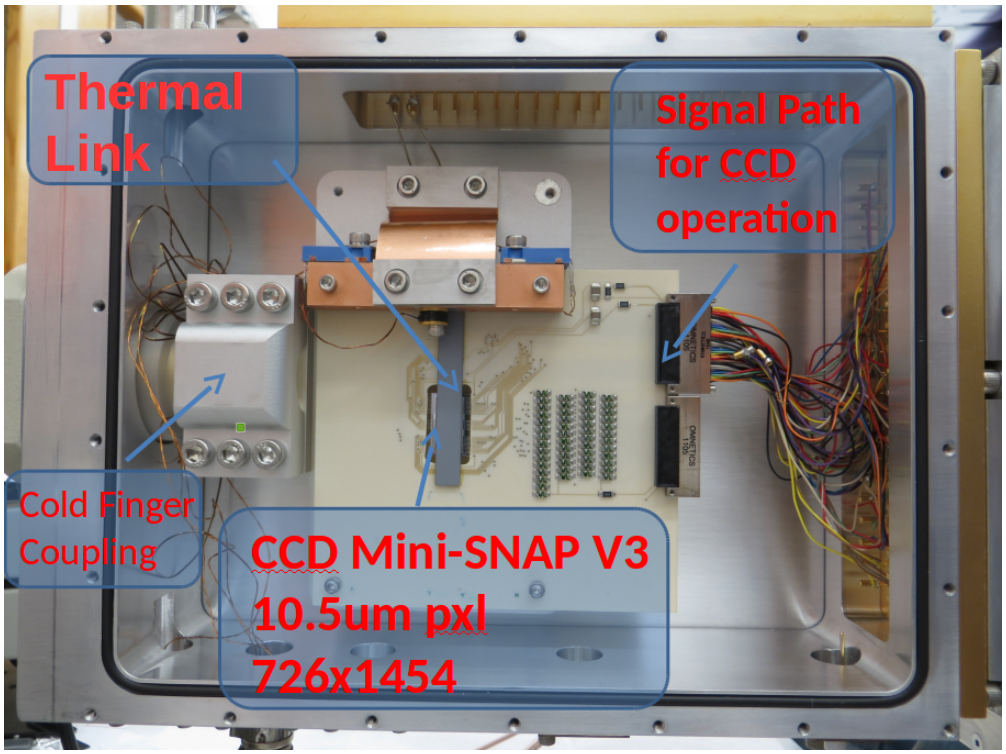

Figure 4.22: Variable temperature cryostat and DALSA control 147154.4 #9. Feedthroughs provide clock and bias lines to operate the device. The thermal link is SiO_2 to which the Mini-SNAP CCD is glued. This bar covers the pixel plane of the device.

DALSA CCD performance metrics, a candidate Mini-SNAP CCD-strip device 147514.4 # 3 was chosen for demonstration of the CCD-strip readout. Here we wire-bonded the device on both sides of the PFB with strips biased via 1 GΩ resistors on each of the 52 strips. An 8nF AC coupling capacitor was used to readout strips and provide some bias filtering. Strips were instrumented with a small number of MAFIA CSA [17] which had a gain of about 6-8 V/pC. Time constants for the preamps varied somewhat but were centered around 125 μsec. Preamps provide AC ground for signal present at the strips, which is important to operation. Strips that were not instrumented were AC grounded.

High leakage current was present in the CCD-strip device. This leakage was similar in magnitude to those observed in the DALSA control. The effective DC impedance of about 19 MΩ through the strip bias resistors implied that a significant fraction of applied bias would drop across them. Additionally, large transients appeared in the preamp outputs for CCD-strip (Figure 4.26) at moderate applied V_{sub} voltages of around 50 V. The amplitude of these variations was at times 3-5 MeV, in equivalent charge, with long time constants on the order of milliseconds. Note that these are convolved with the preamp time constants, however the structure was not periodic in an obvious way. These transients were observed over each instrumented strip.

Strip operation would be severely limited by the excessive leakage that was present in

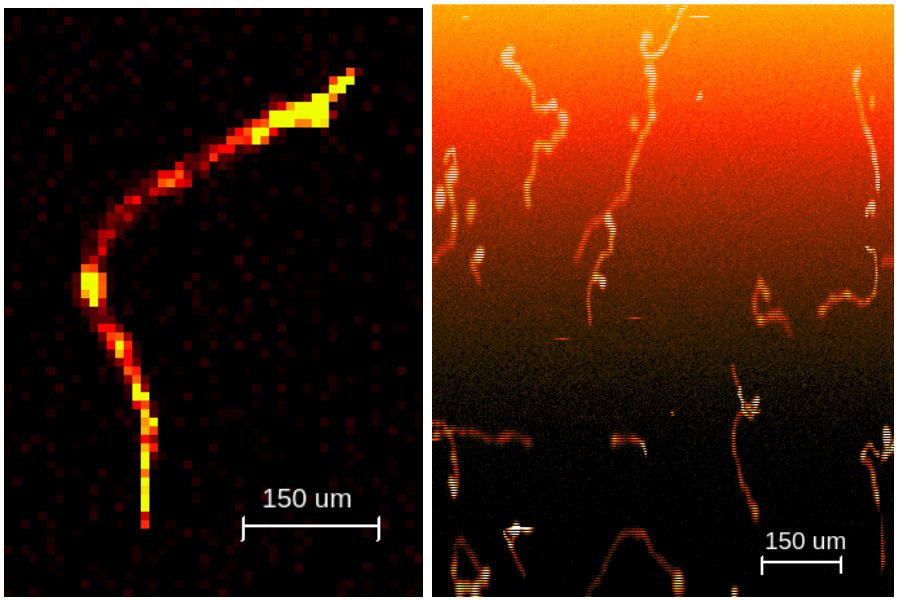

Figure 4.23: (Left) First observed electron track at the LBNL SNAP cold probing station from wafer 147514.4 #3. Conditions were -65°C, 60 V. The electron track is degraded due to higher leakage at this temperature. (Right) First electron tracks observed in our cryostat. Horizontal banding occurs here due to a phase and delay problem in the CDS. Conditions were 140 K and 60 V.

CCD-strip system and was the most obvious problem present in operation. It was, therefore, important to characterize the leakage to deduce the origin. In previous generations of the SNAP devices, puchthrough currents had been a significant source of bias leakage [22]. These are parasitic sources exist due to parasitic JFETs formed by the channel stops on the CCD plane, the n– bulk and the n+ backside. These effects were of interest to us as possible sources of excessive leakage in the device, so we added 2 picoammeters, a custom 1 GΩ input impedance electrometer and a 2 MΩ current source to our setup (Figure 4.29). Ultimately, we were attempting to control V_{N+}, however given the location of the 4 MΩ pull-down resistor and the 0.11 μF bypass capacitor was inside of the cyrostat we elected to sink current down the 4 MΩ resistor. At the same time we measured the voltage with the high impedance electrometer.

Figure 4.28 shows early measurements of the testbed and the reduction in leakage observed. Channel stops are N+ implants in the device which establish the separation between pixel columns in the device and run perpendicular to the detector strips. These structures absorb surface electron current just below the clock field oxide and are normally fully depleted. The 4 MΩ resistor on the channel stops is used as a pull-down to prevent excessive voltage and breakdown near the CCD clocks. In CCD-strip there exists larger coupling between the strips and channel stops which promotes a parasitic current. Because the bulk is depleted, this is a tunneling process which is referred to as punchthrough. Reduction of the current is achieved by reducing the parasitic JFET V_{ds}, which can be results from raising

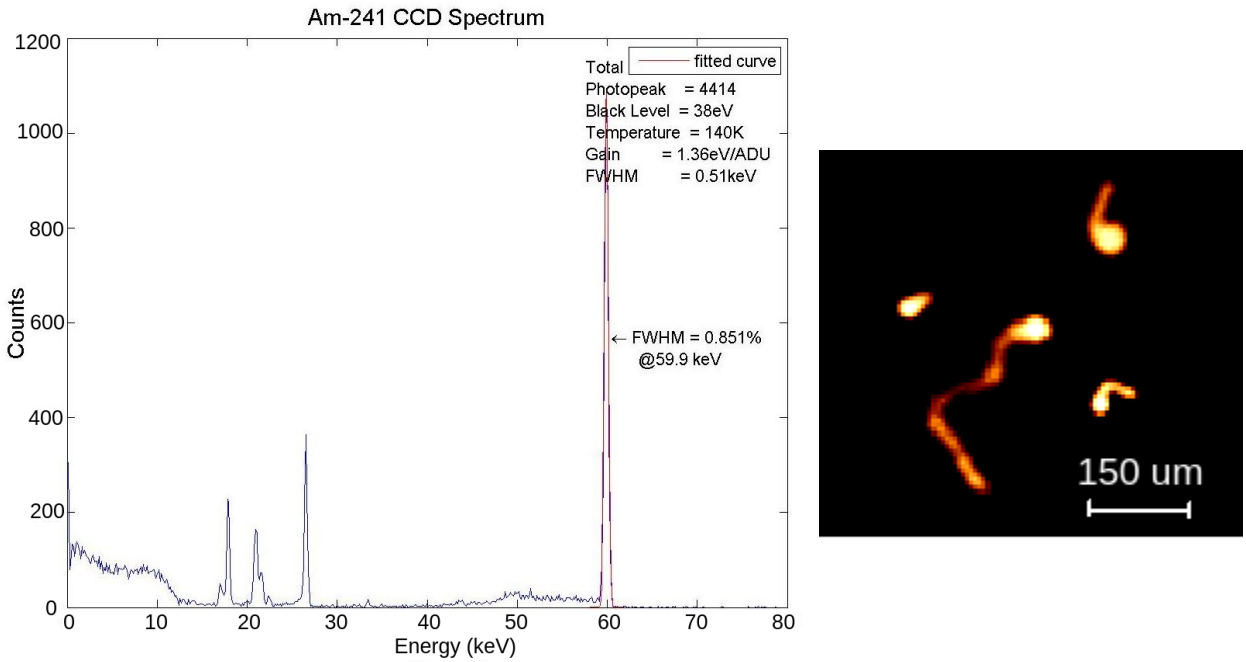

Figure 4.24: Results from the DALSA control device 145714.3 #9. (Left) An ^{241}Am spectrum with performance characteristics around 2x the Fano limit of energy resolution for silicon. (Right) Electron tracks from a ^{137}Cs source. Here we can see that the banding problems observed in the right pane of Figure 4.23 have been removed. Figure 4.23. These two results confirm that CCD devices can be operated in our custom test stand with performance metrics expected from high performance electron tracking CCDs.

the channel stop potential.

Reduction of the bias current removed the transients observed in Figure 4.26. We should note that a degradation in the pixel side resolution was observed, with the blacklevel of 282 eV-FWHM/pxl. This is very loosely consistent with an increase in shot noise from current down the 4 MΩ resistor. Optimally this should be replaced with a 1-10 GΩ resistor to fix the operating point of the parasitic JFET and remove the shot noise. The CCD-strip device performed qualitatively similar to the 10 ms exposure characteristics observed in the DALSA control device. However, comparing Figure 4.24 with Figure 4.32 we can see that the blacklevel noise is about a factor of 3 worse. While this result is not substantiated by a series of devices tested, it is an important observation on the grounds that it compares a CCD to a CCD-strip device in our testbed. Figure 4.32 allows us to conclude that the resolution loss is consistent with the increase in blacklevel noise. It is important to note that the resolution loss for higher energy events becomes larger, the resolution loss scales with $\sqrt{E} \sim \sqrt{\sum_i^{npix} E_i}$ where E_i is the energy deposition per pixel included in the segmentation. The number of pixels $npix$ contributes σ_{bl} per pixel. Thus the Compton shoulder in Figure 4.32 is blurred.

The strip noise floor is about 100 keV-RMS-ENC after shaping on 0.5 μs timescales

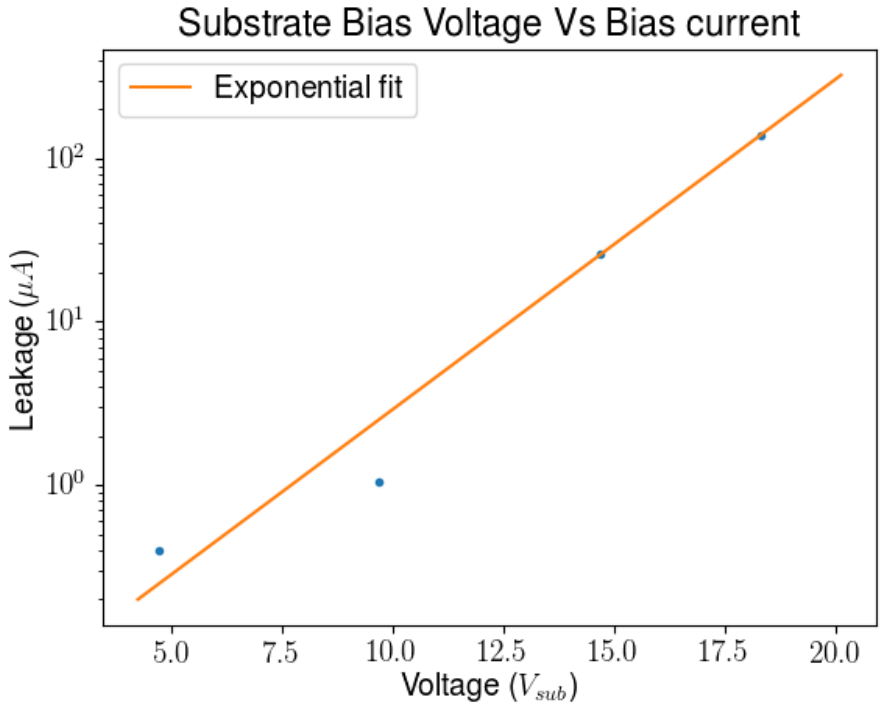

Figure 4.25: DALSA control device 145714.3 #9 at 140 K. The bulk plus surface leakage current was much higher than expected - easily being several hundred microamps at much less than the expected depletion voltage. This behavior in DALSA control wafer was not definitively determined. In niche scenarios, namely at the minimum exposure time, tracks were obtainable with good resolution and comparable blacklevel noise as noted in Figure 4.24.

with battery powered preamplifiers and all other instrumentation powered off. Figure 4.33 shows the supporting data, where the preamplifier and shaping amplifier output noise was measured versus many time scales to capture portions of the noise bandwidth. A Root Mean Square (RMS) measurement was performed at each time window of the strip preamplifier baseline. The scale was set with the preamplifier gain of about 8 V/pC. The scale for the shaped signal was computed by removing the additional voltage gain through the shaping amplifier and with the preamplifier gain. On timescales representative of shaped pulses 0.5-10 μs the noise approaches around 100 keV-RMS-ENC. Different shaping times did not present significantly better baselines. The difference in the shaped versus preamplifier signal noise floor is due to the shaping amplifier bandwidth limiting. For the preamplifier output, we observe about 400 keV-RMS-ENC in quiescence. When the system is powered with voltage applied this noise floor is about 600 keV-RMS-ENC. This is prohibitively high for measuring electron events.

A number of countermeasures can be taken for the powered state of a detector system. However, the bulk of noise is present in the powered off state. The detector is undepleted. For context, Figure 4.34 shows what an ideal pulse would look like overlayed with white

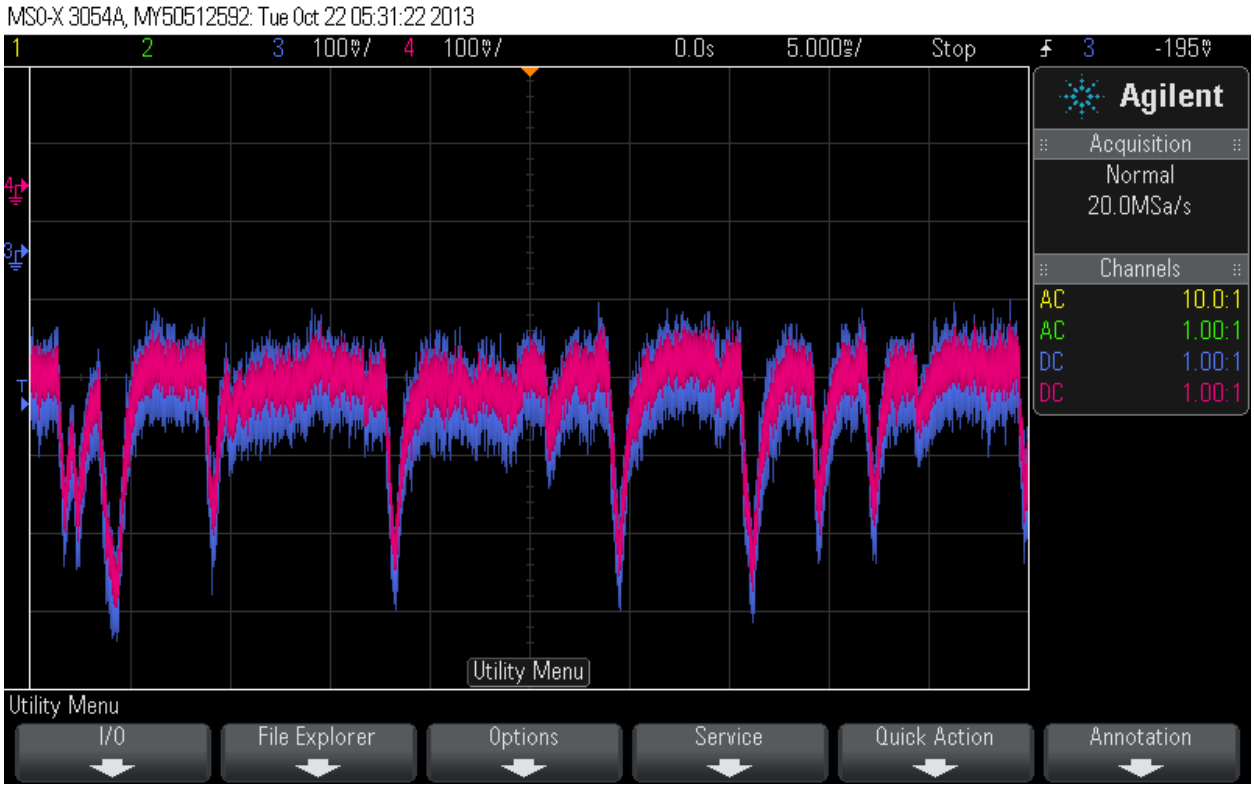

Figure 4.26: CSA output of MAFIA preamplifiers while the CCD is in the **exposure** state. No clocks are operating during this time. Two strips are shown at timescales of 5 ms/div. The strips appear to be coupled to the same transient source and are physically separated by 5 strips. Peak to peak variations (using the preamplifier gains) are on the order of 2-5 MeV, of equivalent charge injection. Conditions are 140 K, 50 V.

noise where the RMS of the white noise is the same as the signal amplitude. The shaped case is more poignant, as shown in the right pane of Figure 4.34. The quiescent state is the baseline upon which, in the bias applied state, the detector would add additional noise sources. These include many other sources, but the 4 MΩ shot noise has been mentioned specifically. This component would only add in the powered state, not in quiescence. The origin of noise in the quiescence state, in this scenario, is limited to external Electromagnetic Interference (EMI) coupling, Infrared (IR) and microphonics. EMI is normally identifiable when coupling occurs due to the emissions that are specific to the operational frequency of the device that emits them. IR would be effected by the temperature of surfaces that emit onto the device. Due to the heat shield, it is relatively hard to stimulate this sensitivity. Microphonics is somewhat non-specific unless there is a clear resonance. Generally, one is worried about wire bonds and cabling that spans the gap between the detector contact, the AC coupling capacitor and the preamp input. Unfortunately, almost all solid state detectors are extremely sensitive to vibration. There is no clear candidate in our current understanding for why electrons cannot be measured at the CCD-strip backside, other than the noise floor

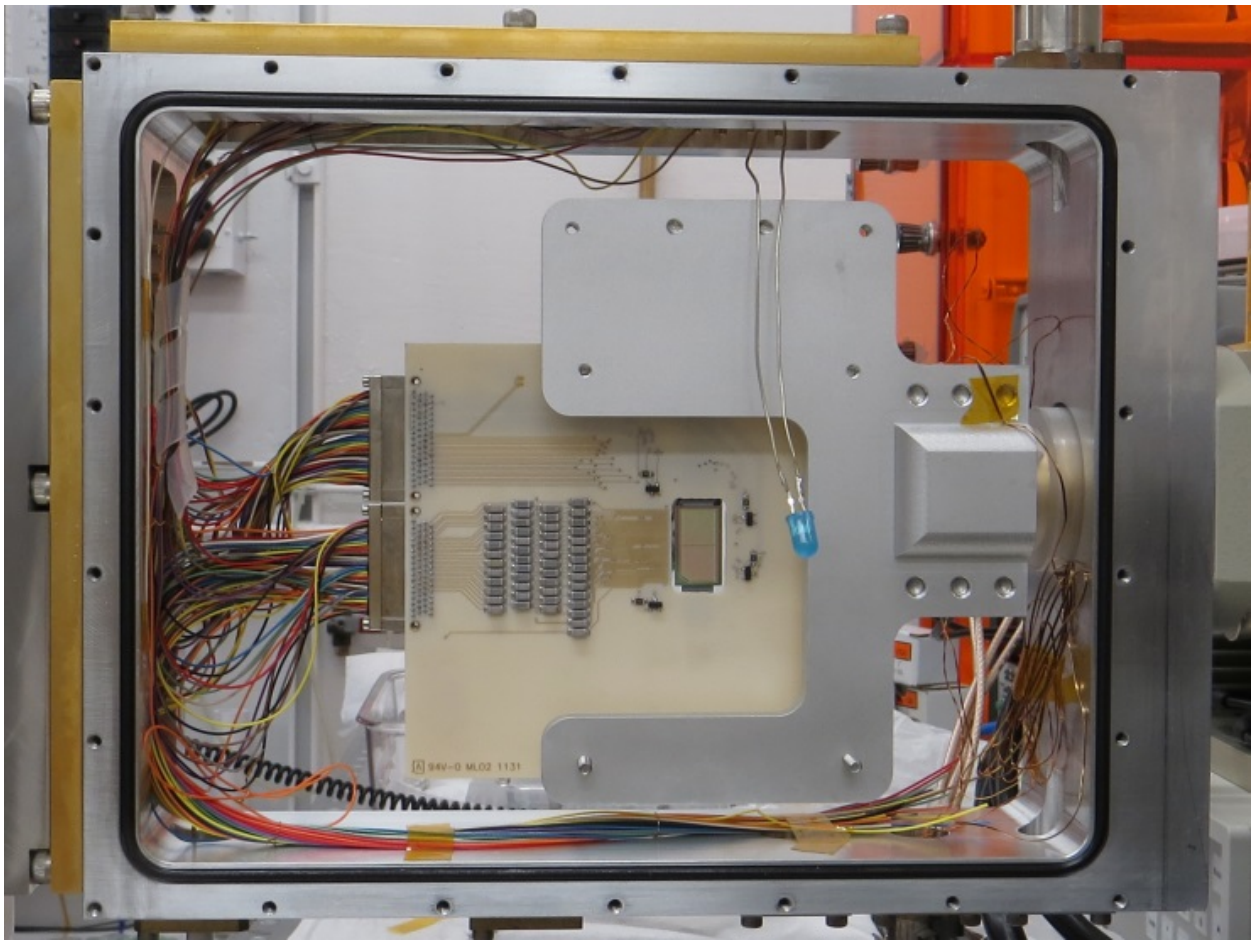

Figure 4.27: CCD-strip mounted and instrumented in cryostat. The 8nF coupling capacitors make up the component array seen with traces to the lower 64 pin connector. This connector attaches pins individually to feedthroughs at the top of the cryostat.

is high even when the detector is in quiescence, as Figure 4.33 shows.

In consideration of the noise problems, we have several tasks in future work that could help to reduce noise in the quiescent state. The thermal link in the detector system is suspect for some of these issues. The concern here is mostly related to wire bond microphonics. The mass of copper HSB floats at the end of copper shims off the cold plate, the copper HSB contacts the Si HSB as a beam with a center fulcrum. Securing the copper HSB relies on screws which act as loads at the ends of the beam, when the loads are applied the Si HSB deflects as the PFB is strained by the loads. Two problems exist here: the copper HSB is a massive object attached to spring-like copper shims and the PFB deflection induces strain that is not necessary. Fixing the thermal link could also benefit from a low profile thermal shield to reduce IR leakage. A design was produced, however the implementation and testing are yet to be realized (Figure 4.35). These have the potential to reduce the powered and unpowered noise states.

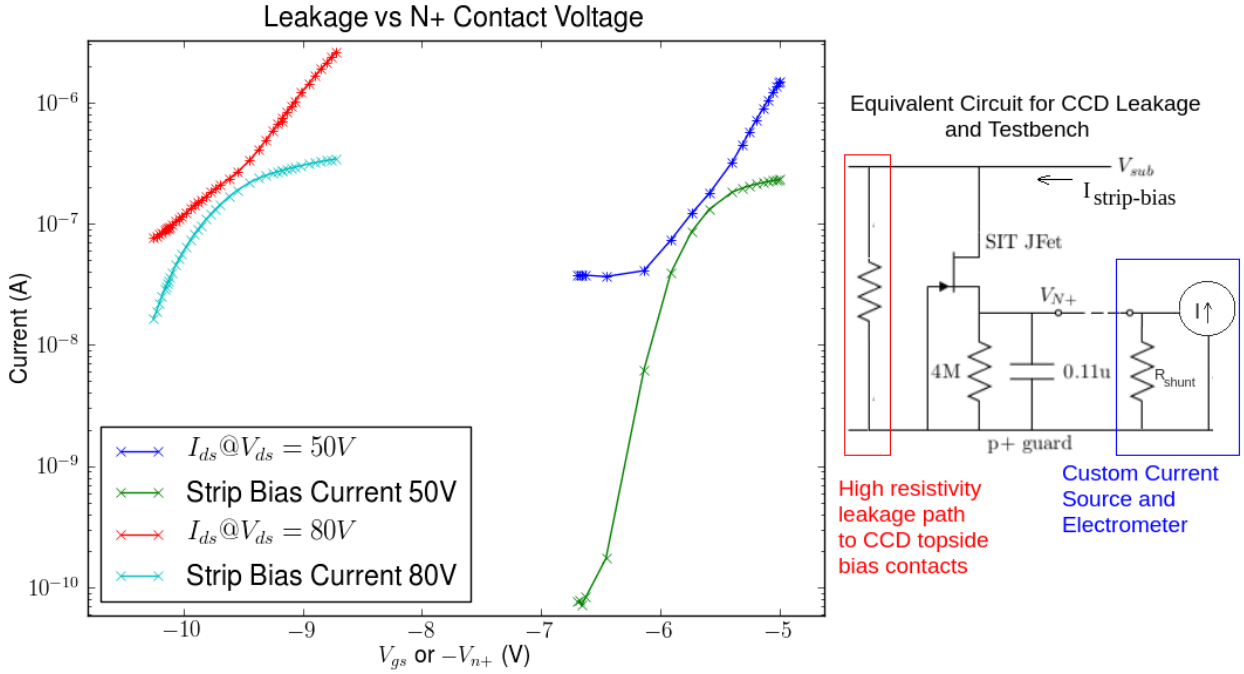

Figure 4.28: Early revision of the test stand we created for measuring bias, strip, and channel stop current. In normal operation most of the strip bias should leave the device through the depleted region, meaning that very little current should be routed to the topside bias contacts. The leakage that the device approaches, $\geq 10\mu A$, is far to high to allow leakage down the effective impedance of the 52 strips, of namely 19 MΩ. The leakage instead is routed to the topside contact. As V_{n+} becomes more negative, with application of bias controlled via the current source, the leakage in the device drops as the SIT JFET[22] is forced into deep cutoff. If the strip bias current and the I_{ds} of the device accounted for all bias current, they should be equal. However, in this implementation of the test stand the 20 MΩ shunt impedance limited our measurement. In summary by adjusting the bias on V_{N+} we see an exponential drop in current, which is necessary for correct strip biasing and leakage current flow. The motivation behind the SIT JFET model is proposed in Figure 4.29. These curves are characteristic of JFET amplifiers in deep cutoff. Figure 4.30 shows the final version of the testbench, where the currents are equal. Measurement conditions as specified and 140 K.

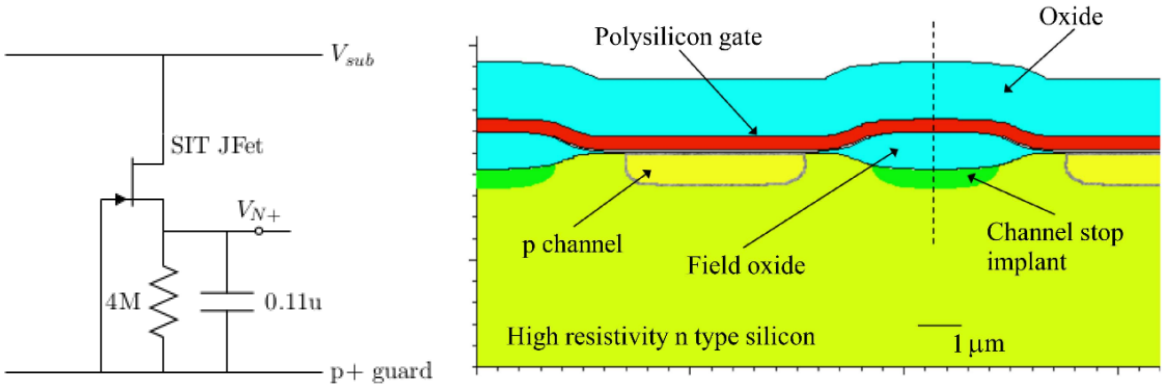

Figure 4.29: (Left) A Static Induction Transistor (SIT) JFET parasitic structure within the CCD reported in [22]. Channel stops (designated V_{N+}) are present in the device to constrain charge wells in the horizontal direction. (Right) A cross-section of the pixel plane and channel stops is presented from [22]. These structures are reverse biased from the charge wells in the p-channel and absorb electron current produced at the surface of the device. The p-channels are cleared at the beginning of exposure, establishing a floating but near zero potential. This is the rectifying contact in the CCD. On the regions exterior to the imaging plane there are other p-type structures called p+ guard rings which behave in the same manner as the gate of the parasitic JFETs. The JFET channel is formed by the N+ strips and channel stops with the n– bulk. The leakage from channel stops establishes an operating point with the pull-down resistor. A discrete resistor and capacitor form the pull-down and AC-bypass and are located on the PFB.

Return paths are also important for reducing susceptibility to noise in the detector system. This is fundamentally related to sinking signal currents around the detector front end to reduce the number of components which could impact grounding or induce noise. In our case, we need to be aware of the n+, CCD preamplifier and strip preamplifier returns as shown in Figure 4.36. Balancing circuits to increase the common mode response is also desirable, which has been explored but should be considered further.

After CCD-strip operation is demonstrated, it is interesting to observe that checking the strip-pixel registration can be done *in vivo*. CCD-strip is sensitive to visible light from the backside. The metalized strips and polysilicon attenuate blue light differently, providing a transmission mask as can be seen in Figure 4.31 when stimulated with a blue LED. Once demonstration of the strip-side operation is completed, it would be beneficial to analyze this projection with a controlled exposure to the LED. Here we can see significant bending around the edges of the device, which is possibly due to the forward directed emission of the LED.

Alternatively, it would be interesting to investigate the use of the n+ channel stops to detect drifting charge. These contacts are non-collecting (other than electron leakage current). In the properly biased configuration, the leakage down these is < 10 nA. These qualities provide an interesting prospect for generating charge time stamps: these contacts

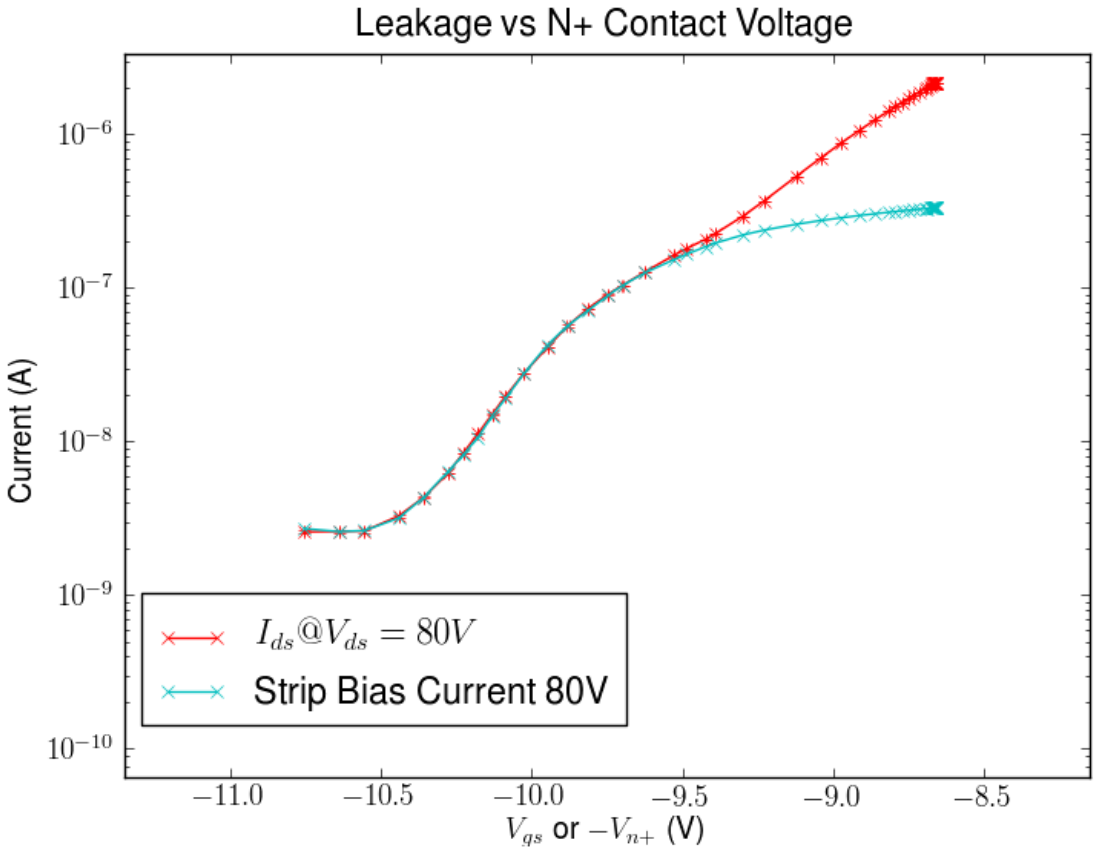

Figure 4.30: Current sums around the device contacts. At large V_{N+} the leakage is reduced by a factor of 1E3. From the second picoammeter, we see that the bulk leakage agrees with the total bias current to within 1 nA. The parasitic channel was the main source of leakage in the device. Upgrades and calibration of the V_{N+} control allowed 1 GΩ shunt impedance on the custom current source and electrometer, which allowed us to account for the remainder of current around this node. In summary, the leakage reduction allows correct dissipation of electron current at the strip contacts. This removed the large transients in Figure 4.26. Please also refer to the equivalent circuit in Figure 4.29.

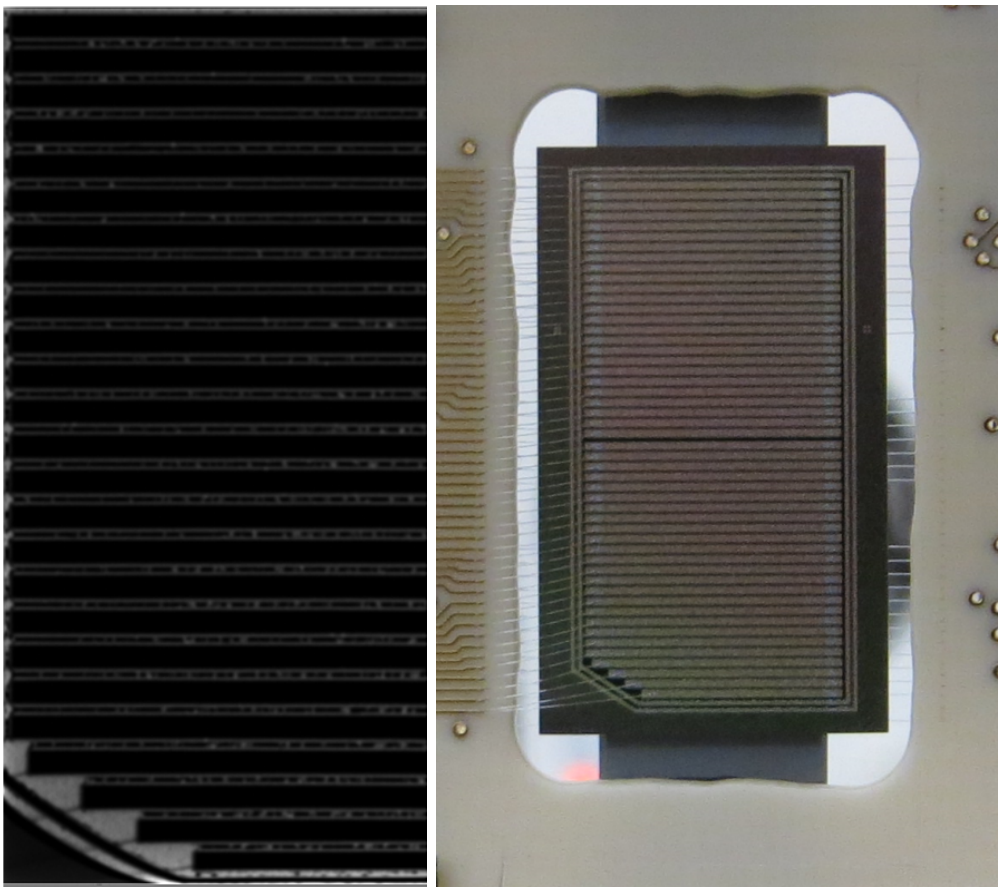

Figure 4.31: (Left) A CCD image of the backside strips from one quadrant. Partial attenuation of blue light from the strip pattern on the back of CCD-strip. The pattern is dark over strips due to high attenuation of the metal, while there is transmission through the passivation in the gap. In the gap the pattern is light-dark-light due to the strip isolation structures from Figure 4.18. Light dots between strips must be places where transmission is favorable, however we do not offer an explanation of this. (Right) A photograph of CCD-strip loaded in on the PFB in our cryostat.

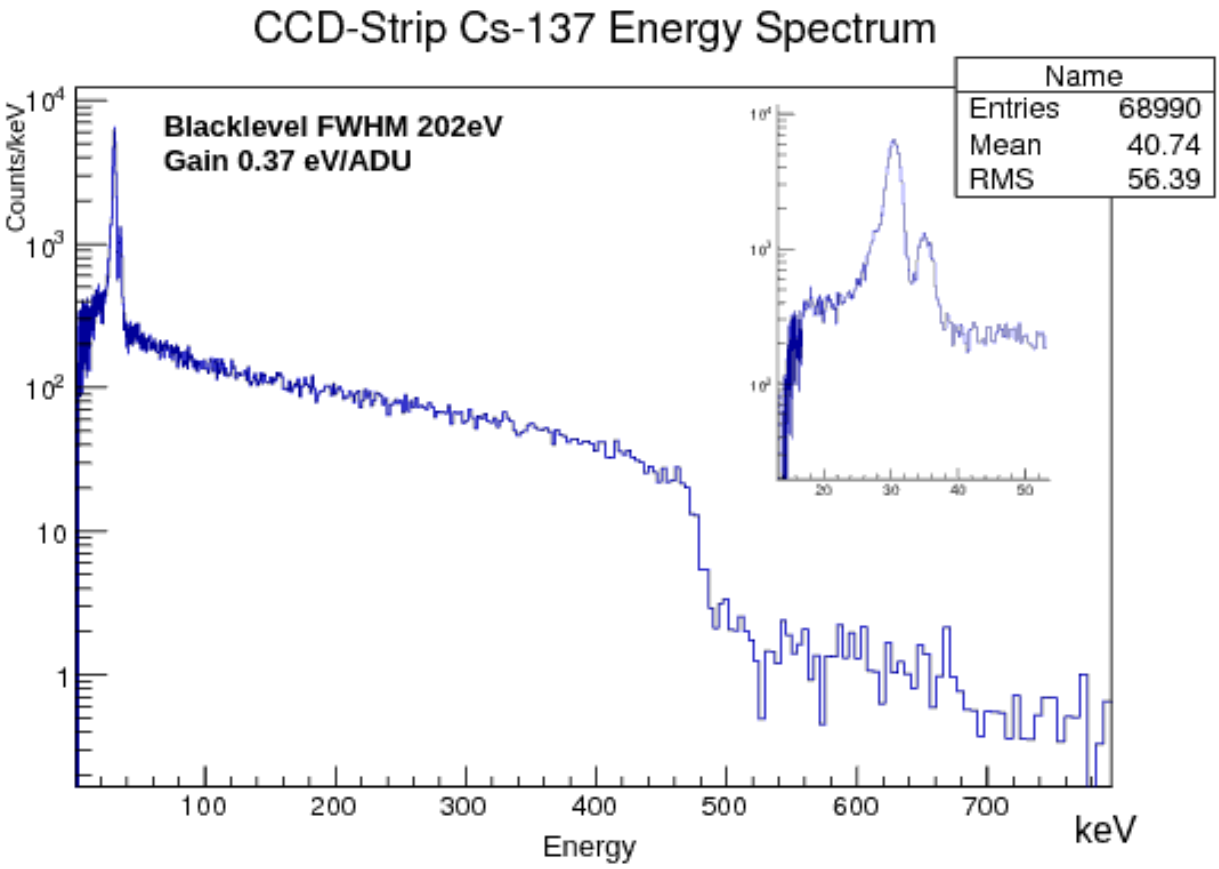

Figure 4.32: Pixel plane operation of CCD-strip exposed to a ^{137}Cs source. An inset enlarges three Cs xrays with energies (intensities) of 32.2keV (3.67%), 31.8keV (1.99%) and 36.40keV (1.35%). The 36.4keV in silicon would be expected to have a FWHM of about 0.8% ideally and 1.2%given the DALSA noise floor. . However, here we measure it to be worse at 6%. This is consistent with the expected increase in blacklevel previously observed at 38 eV-FWHM/pxl to about 202 eV-FWHM/pxl.

must feel induced charge of hole migration to the pixel plane. In effect these are steering grids. The instrumentation of this grid would possibly provide some charge arrival information. These implants are located in many regions not in the imaging area, so in the current implementation it is not clear that they could provide timing information. However, if one found sensitivity, splitting these implants into several sets and routing them out to separate contacts could provide the same functionality as strips applied to the backside. The specificity would be limited due to the fact that they would denote columns rather than rows, however in a Mini-SNAP device the number of rows per channel stop is the same as the number of columns per strip. Combining channel stop implants together would reduce the density of routing.

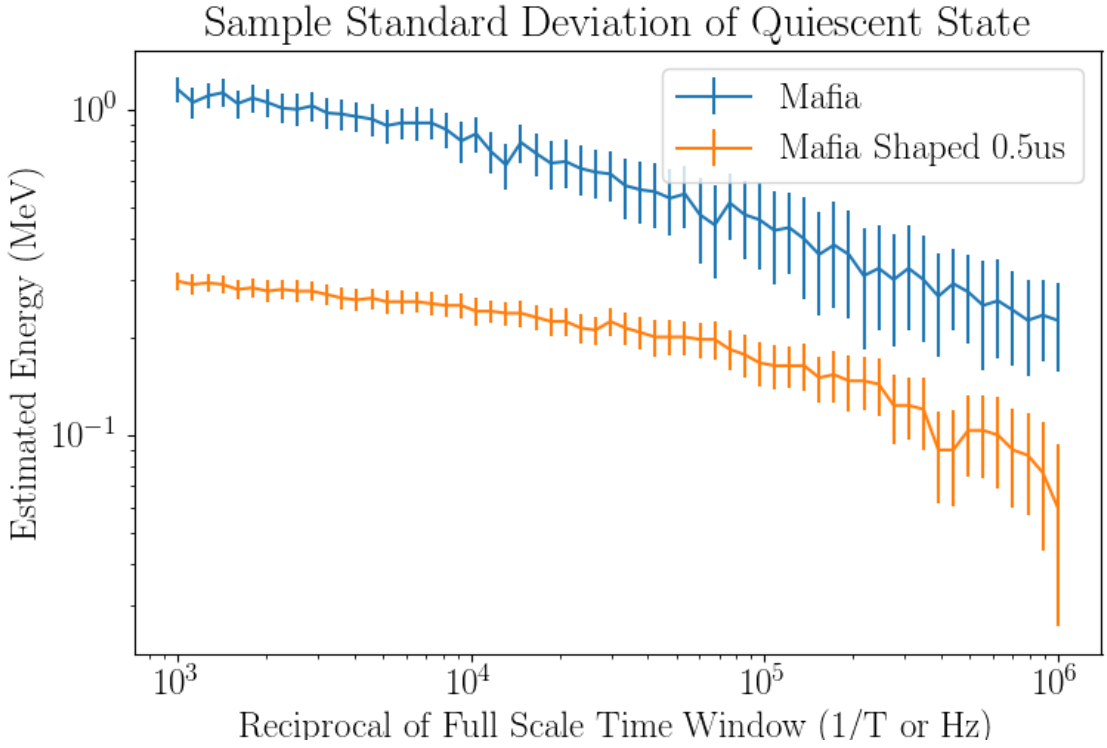

Figure 4.33: Strip preamplifier noise floor at the quiescent state. The sample standard deviation at many time windows was selected because the bandwidth of the measurement changes with the timscale. For shaped pulses this approaches the 100 keV-RMS-ENC level, which Figure 4.34 demonstrates what the $\frac{S}{N} = 1$ would be for ideal pulses by super-imposing a toy strip CSA response for a charge deposition that is equal in magnitude to white noise RMS voltage convolved with the preamplifier response.

CCD-strip Conclusion

This section has presented challenges facing CCD electron trackers, namely that the FRT establishes the time resolution of these devices. The FRT scales with device area and is far too slow for Compton Imaging coincidence time windows. CCD-strip was introduced as a possible electron tracking detector that could overcome the limits of the FRT. We have shown progress in the fabrication of these devices and have demonstrated basic operation of the pixel plane in an LBNL test stand and in our own custom cryostat. We demonstrated performance typical of SNAP CCD devices in our cryostat with the DALSA control devices. Additionally, we demonstrated the pixel plane operation of CCD-strip detectors at 10 ms exposure. A leakage reduction of a factor of 1000 allowed us to remove transients observed on the strip preamplifier outputs. However, the baseline noise was prohibitively high to demonstrate strip operation. The majority of this noise was seen in the state where only the preamplifiers were biased, suggesting that the possibilities for performance degrading phenomenon are

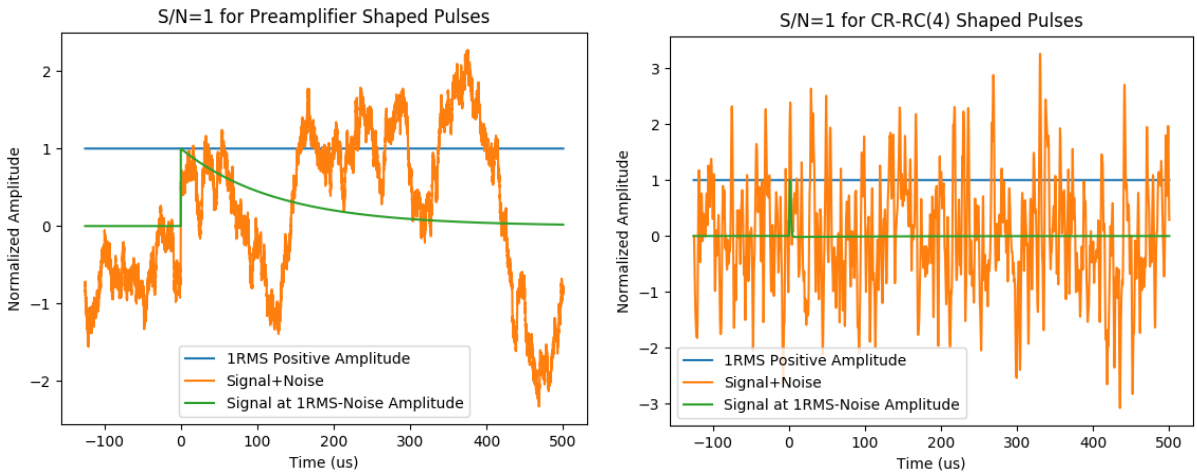

Figure 4.34: (Left) Computed $\frac{S}{N} = 1$ for white noise convolved with the preamplifier response and a strip CSA signal with equal charge to the white noise RMS voltage. (Right) CR-(RC)^4 shaped pulses of the left figure where the amplitude of the shaped ideal strip CSA signal is equal in magnitude to the shaped white noise RMS voltage. These figures attempt to convey the apparent difficulty in extraction of pulses from the noise floor, prohibiting electron measurement on the strips.

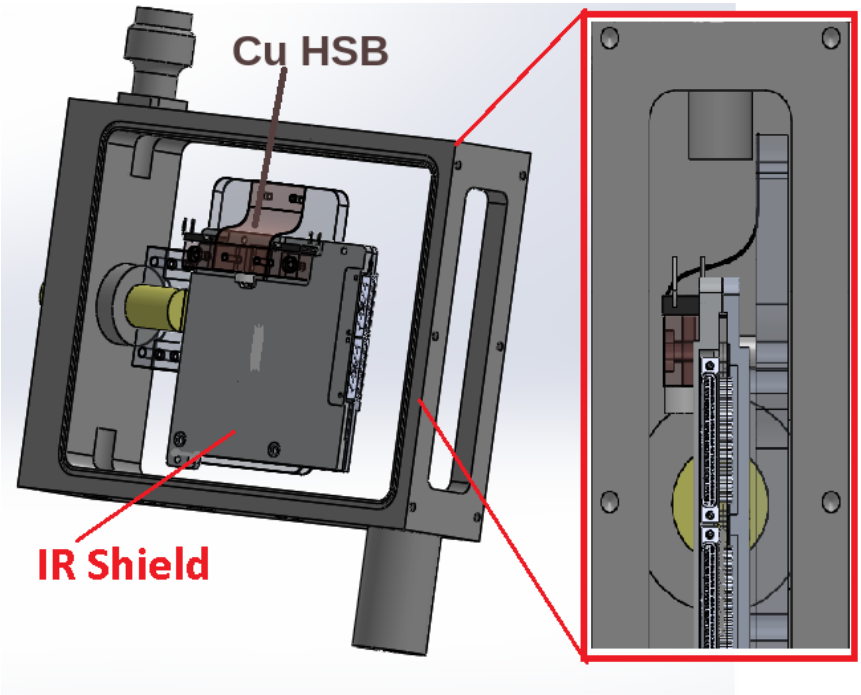

Figure 4.35: The revised IR shield. This design attempts to reduce the vibrational sensitivity to the Cu HSB and provide a lower profile shield so that IR leakage is reduced.

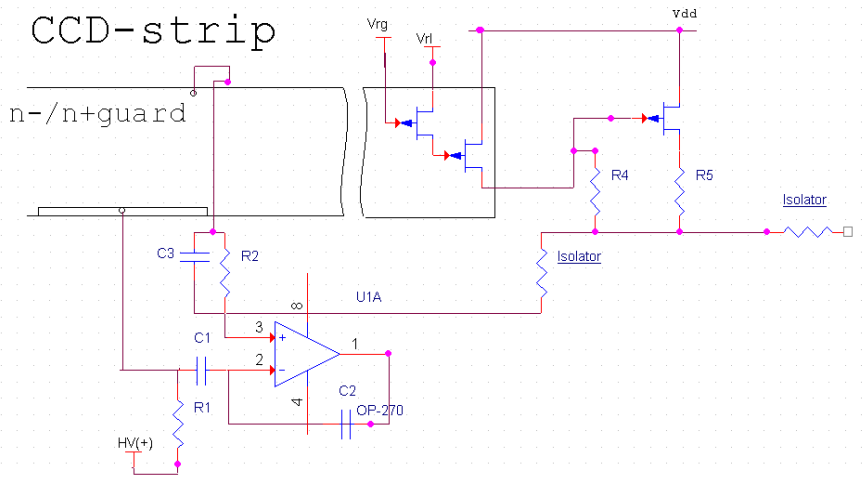

Figure 4.36: Signal current can be made less susceptible to interference by reducing the number of components and the area of the return loop. The scheme listed here shows the readout paths for electrons and holes in the device, and attempts to sink them close to the PFB. Shown are the CCD integrated floating gate amplifiers with a source follower cascade and the strip CSA preamplifiers. Isolation resistors are present in order to provide the option to decouple.

microphonics, IR leakage or EMI. We presented techniques and suggestions for rectifying these problems by replacing the HSB mounting scheme with a low tolerance IR shield. This could potentially help both the microphonics and/or the IR issues. Additionally, we discussed and explored signal return paths for rectifying EMI. This concludes our discussion of the progress with CCD-strip, the next section presents fundamental problems with multiplexed, pixelated architectures and explores other sensors that could be used for ETCI.

4.4 Some Alternative Electron Tracking Technologies and Needed Improvements

The high spatial and energy resolution of CCD based systems is attractive for producing high resolution ETCI imagers. However, we note that there are some general features of pixelated systems which should be observed in the utility of such systems and also note that there exist other potential options.

Some Features of Multiplexed Pixel Devices

Pixelated devices such as CCD-strip seek to provide timing information for high spatial resolution events on the pixel side. While the coincidence pairing is possible in this scheme, the FRT of the CCD devices imposes a deadtime on the system which is concerning for

practical use. The deadtime duty cycle is naively

$$D_{dead} = \frac{\text{FRT}}{\text{FRT} + \tau_{exposure}}, \tag{4.3}$$

where $\tau_{exposure}$ is the time the system spends in exposure per readout. The deadtime duty cycle is concerning in the sense that it will establish the throughput of electron tracks out of the system. More concerning in the case of CCD-strip, it may not be possible to recover time stamps on the backside of the device due to clock coupling through the bulk of the device to the preamplifiers. As the duty cycle approaches one, there is a concern that tracks would occur at the wrong location in the array and may or may not be readout of the system in that frame. The serialization of the readout can cause time stamp mismatch. Clocking could prevent some tracks from being time stamped. This is naive because it is conceptually possible to readout charge events between successive clocking events. If one can achieve readout between clock injections then the D_{dead} is related to the duty cycle of the clocking scheme. During clock charge injection, at least in CCD-strip, event timing would be lost because the amplifiers rail during clocking at full depletion.

These readout considerations are present specifically for CCD-strip and would vary by the technology and multiplexing scheme employed. At least for the CCD case, we note that the FRT$\sim$1s/MPxl. Other devices, such as Full Column Parallel CCDs [35], could reduce this rate by slightly more than the number of columns in the device.

Some Features of SOI Active Pixel Devices

Active pixel devices have been proposed for ETCI. Active pixel devices populate each pixel with a charge sensitive amplifier. Active pixel schemes contrast the multiplexed approach as they attempt to simply increase electronics density to handle problems resulting from channel density. Many different types of active pixel efforts are ongoing, however active pixels can differ in the data provided by the choice in circuit architecture. For example, active pixels can supply simple binary output based on thresholds, charge collected or possibly charge over time. Ideally, each of the active pixel schemes has some timing information but in general the range can vary a great deal depending on the architecture/implementation. The challenge in dense front-ends is heavily related to related to physical transistor size, process capabilities and general impedance control (specifically parasitic capacitance). Greater number of elements also pose interconnect issues.

Technologies like Silicon On Insulator (SOI) are attractive as a way to produce pixelated circuits independent of the contact and bulk technology. Low resistivity, Complementary Metal-Oxide Semiconductor (CMOS) circuits can be fabricated on an insulator substrate, which can be connected to a high resistivity bulk that has contact implants implemented. Typically the insulator layer for devices such as SOI Pixel Detector Project (SOIPIX) use a buried insulator region which is implemented by a very high doping of oxygen in several layers. High applied temperature and an annealing process produce uniformity in these insulator layers. Contact with the bulk can be applied while transistors are being implemented.

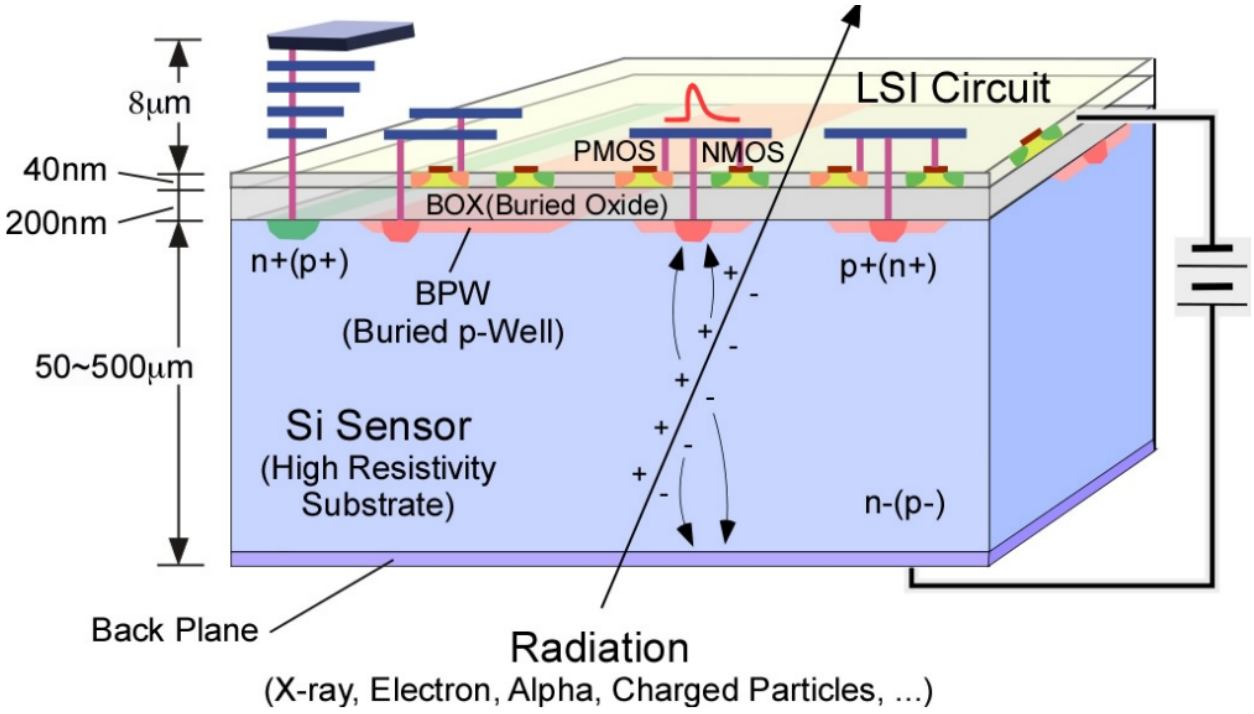

Figure 4.37: SOI active pixel sensor, figure reproduced from [2].

SOI processes for other use cases typically use the oxide layer and inactive substrate layer as mechanical support for a very thin layer of transistors.

Current versions of active pixels still rely on some level of multiplexing or data reduction schemes. SOIPIX for example can region select pixels around a triggered event. Fast timing is supplied via a logical OR of the entire pixel array. Upon triggering the location can be found by a search of the triggered states along the row and columns. Region select allows the charge to be read out in rectangular selections. This architecture has the advantage that the time delay between trigger and readout is 10 s of microseconds. It has the disadvantage that the pixel integration period is not constant and that one has to do pixel bias current subtraction in a second witness period for the region of interest. Thus one incurs a factor of 2 in readout time due to the bias current subtraction.

In the current implementation of SOI systems, pixel sizes are large compared to electron tracking in SNAP CCDs. Pixel sizes are currently on the order of 20-50 μm. Additionally, SOI devices range in thicknesses of 300-500 μm and at the moment would most likely need to be cooled to Peltier temperatures to achieve ETCI systems. There are plans to develop smaller pixels for SOI by stacking SOI layers to generate the necessary front end electronics while decreasing footprint/pixel area [2].

While SOIPIX does offer prompt timing, the drift of charge is not observed over time. Rather, the integral charge is collected in the pixel array, which implies that the scheme is limited to 2D projections of the electron track charge. One would possibly rely on the estimates of dE/dx for the out of plane angle, or new techniques would need to be developed.

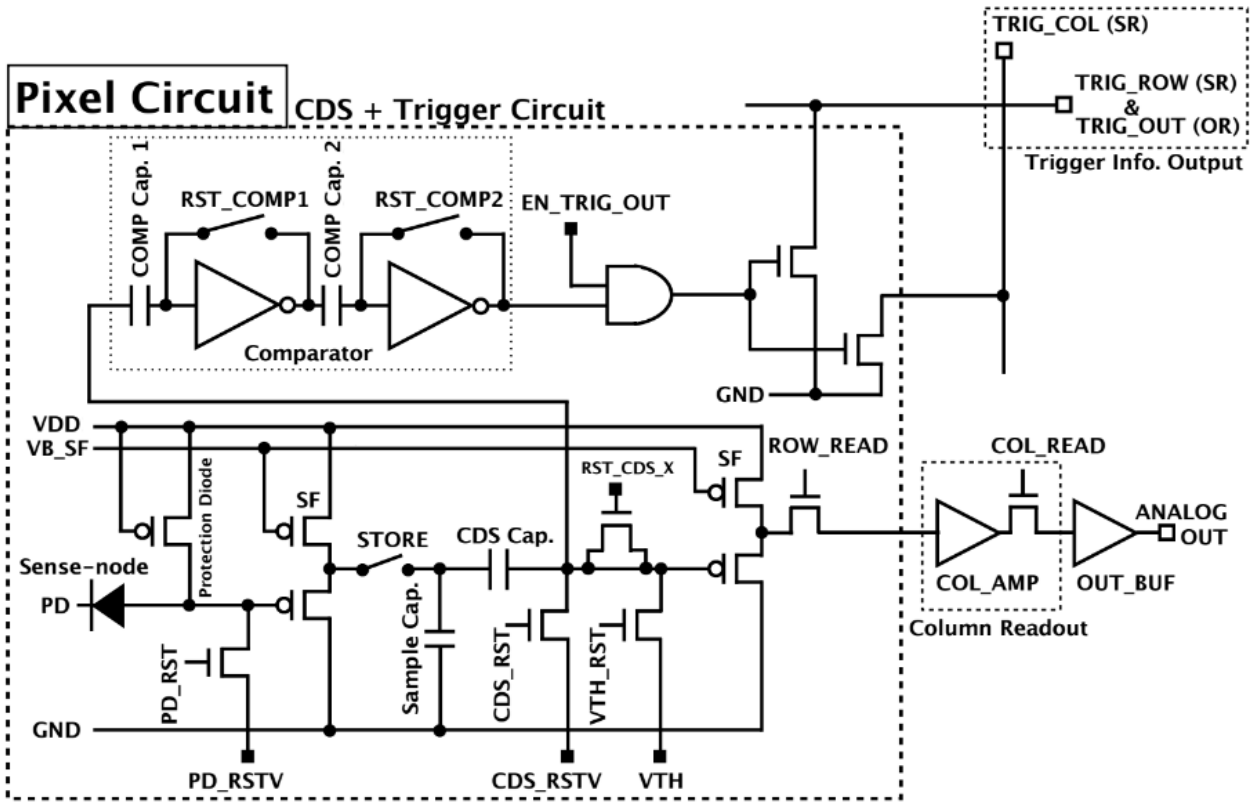

Figure 4.38: The active pixel circuitry in the XRPIX2B[54]. The pixel here provides a trigger scheme based on simple thresholding of the collected charge. A source follower gain stage provides the first amplification. Threshold crossing triggers the STORE signal to capture the device state at the time of the trigger. Charge is held until readout. The pixel can be discovered by looking at the trigger states of the columns and rows.

Conceptually, the estimate for the out of plane angle could be improved with data from the drifting charge toward the pixel plane.

Nuclear Scattering

Regardless of the electron tracking scheme, the detection of these events relies on the estimation of the Compton scattering vertex and the initial electron momentum. In the pursuit of electron tracking nuclear scattering can limit ionization signal in many materials. These events allow the electron trajectory to be changed without liberation of charge in the detector. Rutherford scattering of the electron occurs in materials with a Z^2 scaling of the cross section. Due to the momentum balance with the nucleus there is very little, if any charge deposited in these types of electron scatters, however the trajectory changes immensely. The

Property	Value in Si	Value in Diamond
Density (g/cm^3)	2.30	3.53
Bandgap (eV)	1.11	5.5
w (eV/pair)	3.65	14.3
Fano	0.115	0.08
Perm. Coef.	11.7	5.7
μ_h (cm^2/Vs)	480	1200
μ_e (cm^2/Vs)	1350	1800
Compton Scattering Dominate Region (MeV)	0.060-16	0.030-28

Table 4.3: Properties of Si and diamond semiconductors.

backscattering cross section (scattering greater than 90 degrees) [14]

$$\sigma(\theta > \pi/2) = \pi Z^2 \left(\frac{e^2}{m_o c^2}\right)^2 \left(\frac{1-\beta^2}{\beta^4}\right) \tag{4.4}$$

can be approximated as $\frac{Z^2}{9}$ barns/nucleus for an electron when its kinetic energy is equal to its rest mass energy [14]. The scaling of the ionization scattering cross section in the atom is linear with Z, or the number of electrons in the atom. Care should be taken when including high Z materials in electron trackers to boost photon cross section as the initial track is generally low total energy deposition and the range over which it represents the Compton kinematics is small. As the nuclear scattering cross section increases in magnitude the electron will contain less information about the Compton scattering process and will deposit energy after the initial trajectory has been lost.

We note that diamond is likely one of the best electron tracking materials capable of near room temperature. This is due to high density and low Z. In other electron tracking systems, one trades photon efficiency and electron leakage for resolution of the initial electron track. This is especially true for Compton systems, since low Z materials have the broadest range of Compton dominant cross section. Photoelectric absorption does not dominate until 30 keV in diamond and pair production does not dominate until 28 MeV. Of course, many practical considerations exist between the conception and the realization of diamond electron tracks. These are not trivial and possess many of the same problems previously discussed with pixelated systems. Additionally, we note that the SNAP CCDs represent a long dedication in development and benefit greatly from decades of materials knowledge.

Some properties comparing these two materials are shown in Table 4.3. There are many benefits to diamond detectors, however the energy resolution does degrade slightly. The higher bandgap does offer the possibility of room temperature operation, however this would depend on specific device properties. Comparing theoretical energy resolution $\Delta E_{Diamond}/\Delta E_{Si} \sim 1.65$. As Figure 4.40 points out the overall length corresponding to the Compton kinematics is about a factor of 2 greater with 1/2 the signal per unit length.

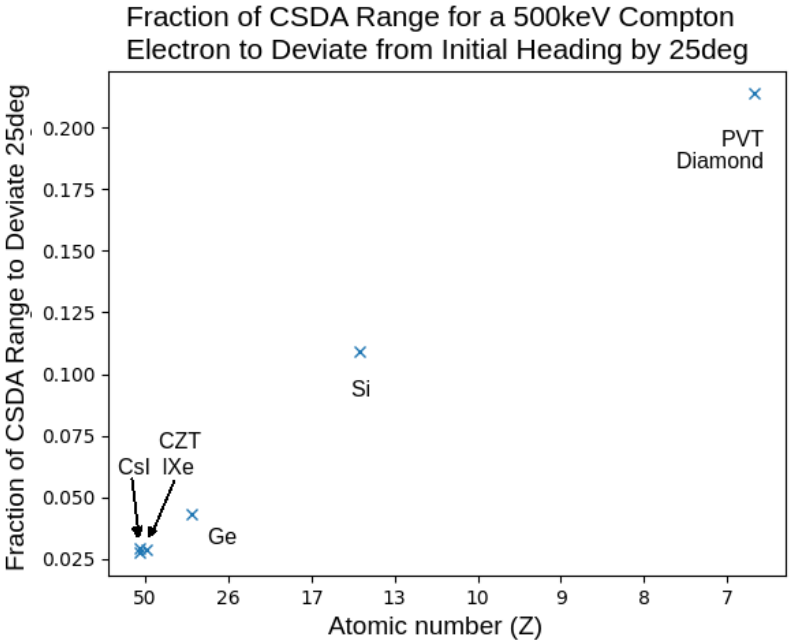

Figure 4.39: A simulation of 500 keV electron tracks in different materials. The electrons are emitted and the distance from their origin is recorded when their trajectory deviates more than 25 deg from their initial heading. The means are recorded for many events and are normalized by the CSDA range of 500 keV electrons in that material. The horizontal axis is scaled as 1/Z, but labeled in atomic number. The linear trend corresponds to the 1/Z tradeoff between electron multiple scattering and nuclear scattering. At high Z the range over which the Compton electron retains kinematic information is severely reduced due to nuclear scattering. Diamond detectors would be of interest due to their low Z and relatively high density. For example, the CSDA range for 500 keV electrons in silicon is about 943 μm while the CSDA range for diamond the range is about 566 μm. The range over which electrons will deviate by 25 deg is 103 μm in Si and 116μm in diamond. The increase in density in diamond does not hinder tracking.

To conclude we note that the nuclear scattering limit applies to all designs which consider using electron topology for tracking. Some material choices are decided for other physics based reasons, and the use of higher Z materials is not precluded in electron trackers. We simply emphasize nuclear versus ionization scattering as an important parameter in design of an electron tracker as it determines the amount of vertex information that can be measured through electronic excitation.

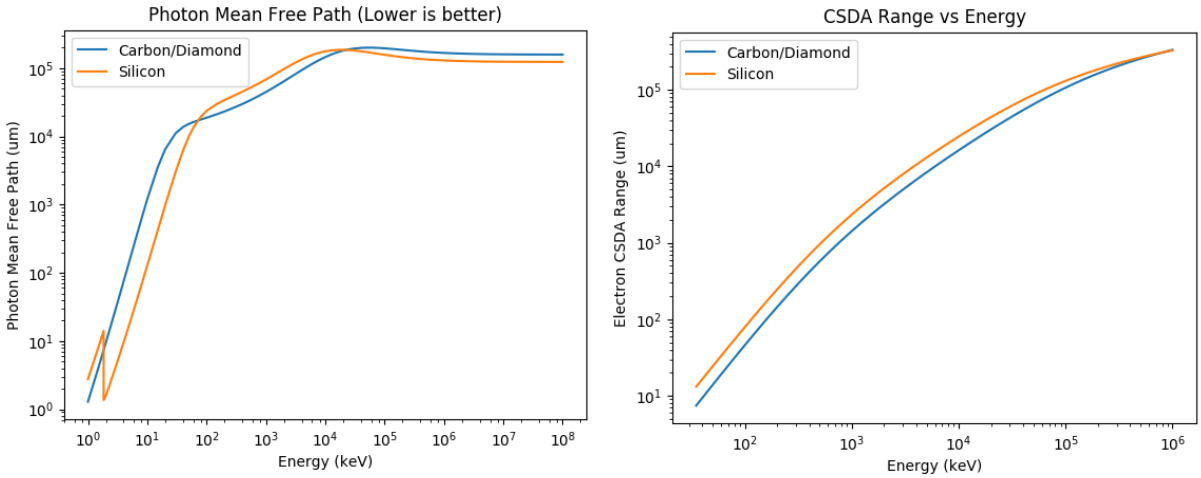

Figure 4.40: (Left) The photon mean free path in Si and diamond [6]. Over the range of interest (10-1000 keV) the photon interaction cross section is about a factor of 2 larger in diamond than Si for most of the relevant Compton scattering range. (Right) Electron CSDA ranges are also about a factor of 2 lower in diamond than Si [5]. Due to a ∼2 factor increase in dE/dX and a factor of ∼4 difference in the bandgap there is an effective decrease in signal per length by a factor of 2 for diamond. However, Figure 4.39 shows there is about a factor of 2 increase in track length which corresponds to Compton kinematics.

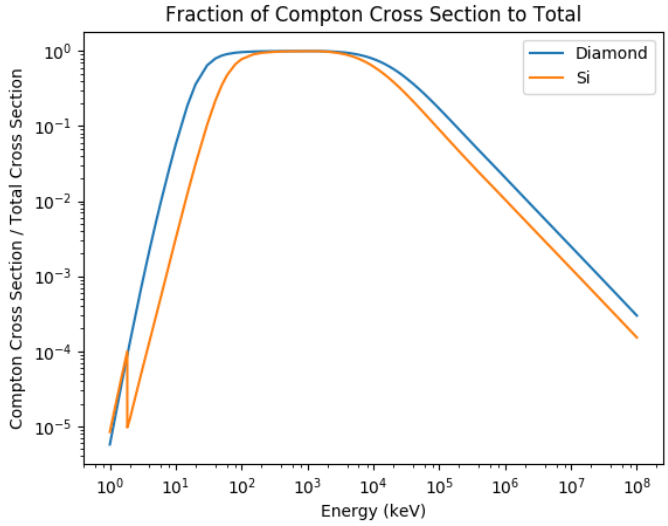

Figure 4.41: The Compton cross section compared to the total for two materials. Here we see that the low Z enhances the viable Compton region but only marginally [6].

Chapter 5

Advancements with Simple Detectors and Contextual Sensing

Given the relatively high cost and complexity of Compton imager detector development, it is interesting to consider ways to reduce the necessary detector performance requirements to achieve Gamma-Ray Mapping. One potential avenue to reduce the detector complexity is through contextual sensing and data fusion. Contextual sensing provides a way to generate information about the measurement environment, and data fusion is the combination of contextual data with radiation data. This can enable, for example, Proximity Imaging modes of operation with simple, monolithic radiation detectors to produce Proximity Mapping systems. Proximity Mapping at 100 m-1 km resolution has been demonstrated, as in Figure 5.1. Data for Figure 5.1 was collected by NNSA via aerial survey of the FDNPPA just after the reactors volatilized their radioactive inventory, dispersing it over the Japanese countryside. The sensors used were monolithic NaI bars with synced GPS. Despite the lack of high spatial resolution, energy resolution or sophisticated reconstruction, the data provided one of the most complete and immediate evaluations of the extent of the accident. These data were indispensable in early risk management of the FDNPPA, as evacuation orders and policy decisions relied heavily on the quick delivery of these systems and the resulting data products. Later this data was crucial in the estimation of excess risk to people exposed during evacuation. In retrospective analysis, the radiation dose was not one of the dominant risks to people, as the World Health Organization (WHO) notes [41]

> The present results suggest that the increases in the incidence of human disease attributable to the additional radiation exposure from the Fukushima Dai-ichi NPP accident are likely to remain below detectable levels[1].

[1]While the increased cancer risk is not large, the additional risk is nonzero. The increased absolute risk to the Japanese public for leukemia, thyroid cancer, female breast cancer and combined solid cancers was also calculated by the WHO. These estimates represent the *maximums* from all populations affected by the Dai-ichi power plant disaster. All of these were small in absolute risk, where almost all relative increases were contained conservatively below 7%. However, the low incidence rate of thyroid cancer, especially among

This is an important null result which relied heavily on time-sensitive Gamma-Ray Mapping.

In this section, we present techniques to enhance the utility of monolithic detectors with contextual sensors for meter scale mapping. Data fusion, aggregation and the possibility for autonomous measurements provide substantial gain over the current methods employed.

5.1 Contextual Sensing and Autonomous Vehicles

Advancements in sensors, computational elements, computational efficiency, software and collaboration have aided the rapid developments in computer science. Software has especially seen a large boost through the open-source paradigm [11]. Open-source allows authors to publish useful tools and have their rights protected as they choose. Large scale collaborations have been promoted through the availability of source code and through new source code management tools such as Git [53]. Rapid integration of many software tools is made possible through the efforts of the open-source community, as they supply the "software infrastructure" for many projects. While hardware and sensor development has yet to see this kind of expansion, data fusion has seen large growth.

Gamma-Ray Mapping fundamentally relies on the mapping and pose estimates provided by contextual sensors. Positional estimates of systems in complex environments opens up the possibility for many types of proximity and complex imaging schemes. Scene data collected from contextual sensors can be fairly sparse and simple or dense and rich. Simple scene information could be GPS based while more complicated data sets could feature full scene reconstruction. Both are presented in this section, and we note the limits and merits of each.

GPS limits for meter scale mapping

A Global Positioning System (GPS) typically provides location estimates in 3 dimensions through the receipt of 4 or more GPS distinct satellite signals. In consumer grade GPS with a single antenna, a typical limit of position resolution is 1-3m [55]. Differential GPS can obtain higher resolution and provide more robust heading. Differential GPS that is wrapped into an Inertial Navigation System (INS) can provide centimeter resolution on position estimates [58]. However, all GPS solutions suffer from the canyon or "urban canyon" problem [9]. This constrains the use of GPS to outdoor environments and limits the use in certain environments.

Figure 5.2 presents count rate mapping measurements from an area inside the FDNPPA plume. The area is known as a calibration area because it has a relatively uniform ^{137,134}Cs distribution, except for a prominent hotspot. The hotspot is located at a low culvert which connects two fields at the road intersection. The surface of the road is much higher than

children, pushes the conservative relative increase to 70%. The absolute risk puts this in perspective: lifetime risk of thyroid cancer for Japanese females is 0.75%, however a female infant exposed to the highest doses of all infants after the Fukushima Dai-ichi disaster would have an absolute lifetime risk of almost 1.5% of developing thyroid cancer [41].

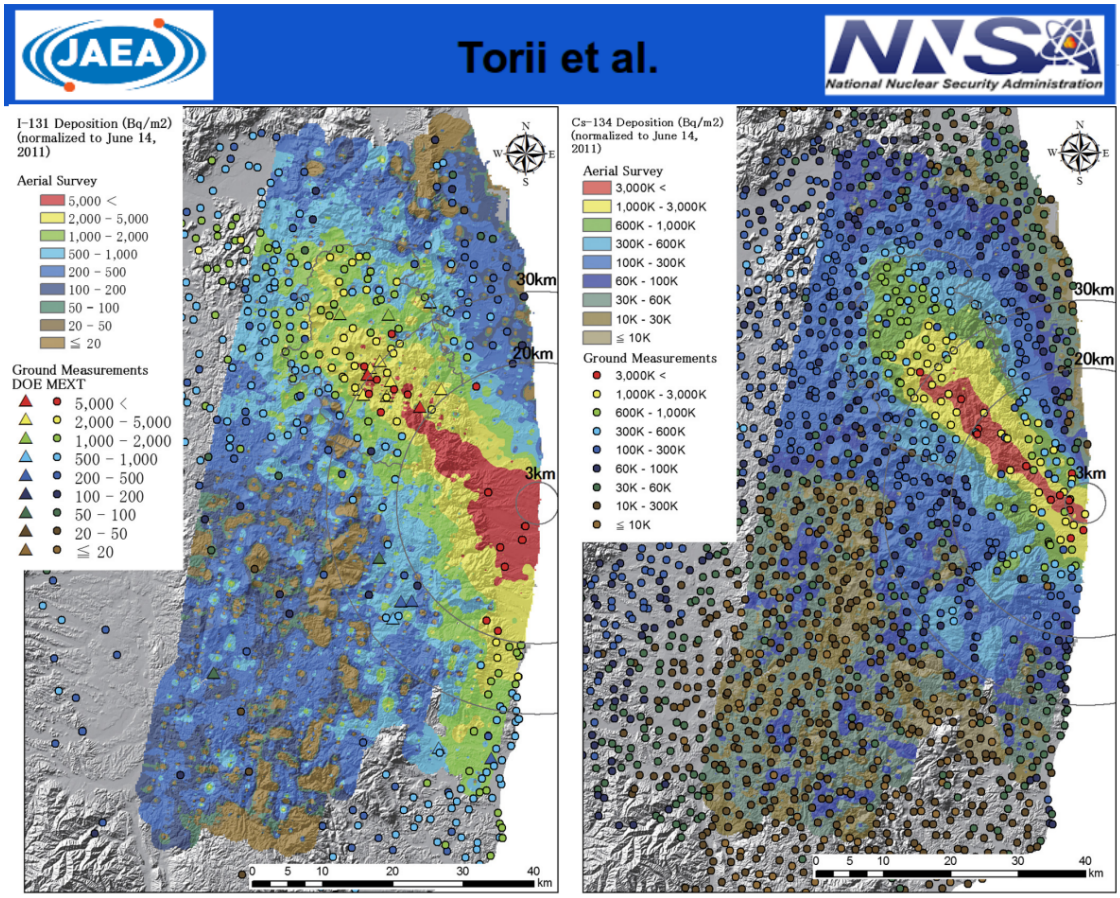

Figure 5.1: (Left) ^{131}I surface contamination map of the affected areas near the Fukushima Dai-ichi power plant just after the FDNPPA. (Right) ^{134}Cs surface contamination map. Maps like these assisted in dose calculations for received dose during the evacuation. This scenario represents a 2D Gamma-Ray Proximity Mapping application in which monolithic NaI was used along with GPS to show the spatial distribution of radioisotopes of interest. The data was acquired by taking aerial surveys of the areas and Proximity Imaging. Provided high energy resolution the ^{131}I and percent level lines in ^{134,137}Cs lines would be resolvable but were not in this case. Despite not being able to fully resolve the two, peak overlap calculations allowed for estimates of ^{131}I to be calculated. The concentrations estimated from the fly over are shown as the heat map with sample points represented as dots on the same color scale. Sample points were taken by hand to compare with the contamination maps. Figure is reproduced from [52].

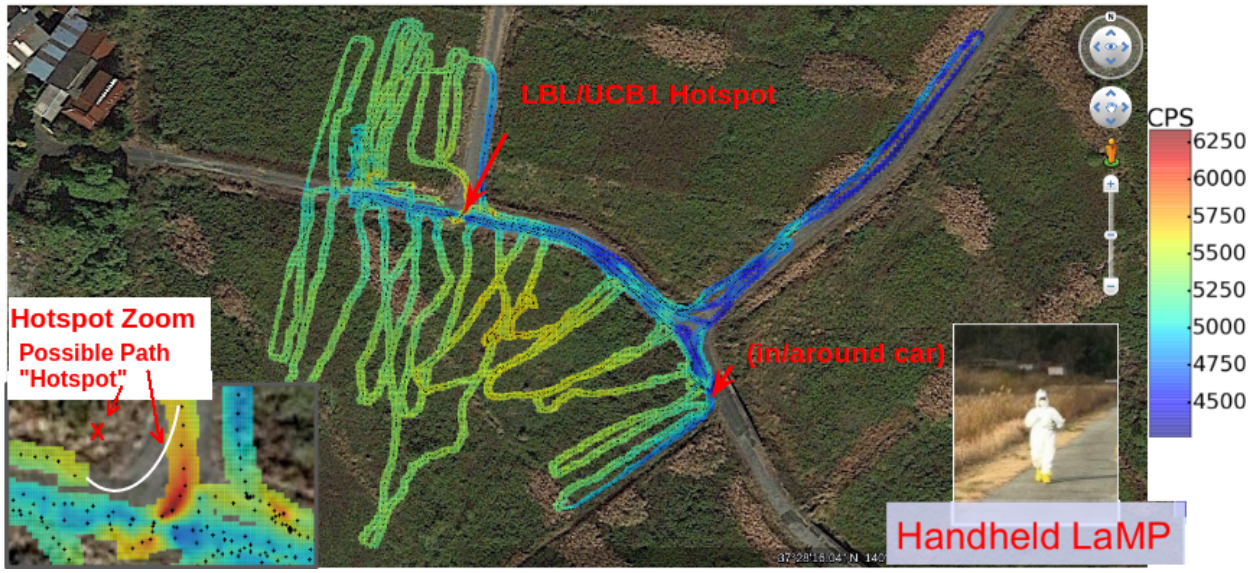

Figure 5.2: 2D grid interpolated from walking data from handheld radiation detector system with GPS for localization. CsI scintillators are used as simple counters here. The system is carried at waist height. The scene includes high reeds in the fields and clear paths on the roads. The right inset shows a photograph of the measurement technique. To the left a zoom of the hotspot. Here we suspect that the simple hotspot is a culvert just on the intersection elbow. However, the GPS path does not match the path walked. Thus there are regions of very intense count rate and areas with low count rate intersecting each other. This measurement is crucially dependent on the location of the system, however the GPS allows path deviations much greater than expected. This creates data that looks non-physical. Contamination is ^{134,137}Cs in the Fukushima plume. Dose rates in this area varied from 0.5 μSv/hr to 15 μSv/hr. Namie Town, Japan Dec 2015.

the fields, which are flood irrigated. General features of the scene are the relatively cold road surface, which is washed by heavy rainfall in the winter and spring. The fields do very little water drainage, and washout of FDNPPA products is not as prominent, except in the low culvert. GPS provides the location of the system. The detectors employed here are commercially available CsI scintillators which are 2 Kromek Sigma50s [32]. These detectors have an active volume of 65 cm^3.

General features can be observed which include the relatively cold roadways due to isotope washout. The fields tend to show larger amounts of contamination due to water stagnation and thus deposition. The hotspot should correspond to a drainage culvert, however the lack of resolution places the system in a location significantly off of the reported maximum. A grid is used to interpolate points off the track that are closer than 3m. These features are useful, however we would like errors in the track like those observed are not acceptable in complex environments where source distributions are not well known or need to be localized to specific objects.

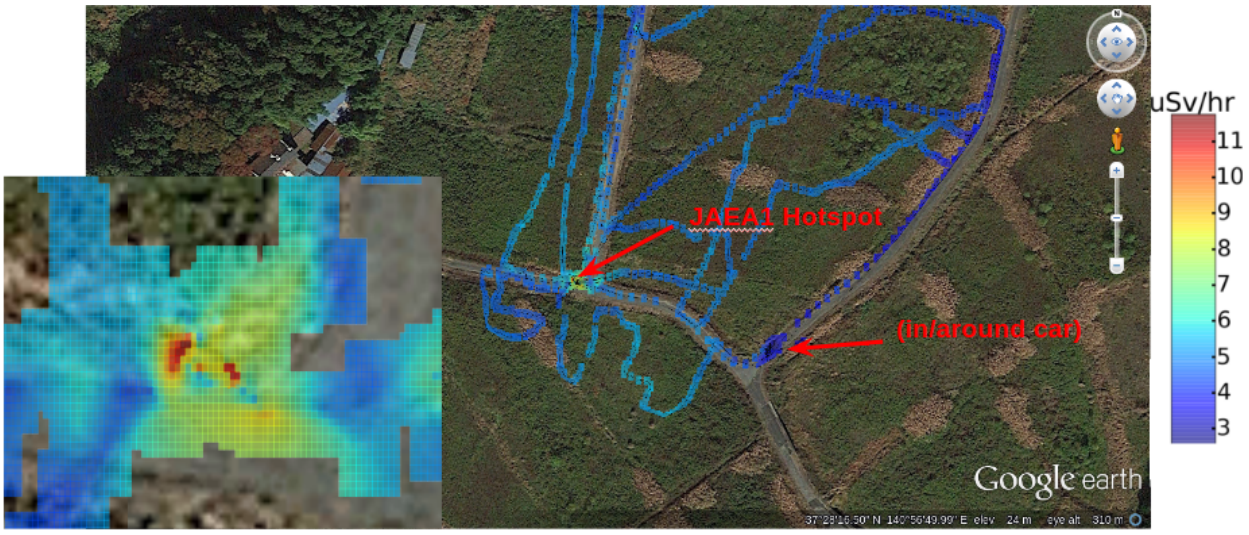

Figure 5.3: An experimental system used by the JAEA attached to a conventional tablet with a small Si diode sensor for dose rate estimation. The system produces measurements at a rate of about 0.5Hz. The location of the hotspot is replicated better in this data, however there is a good bit of fragmentation in the hotspot which is difficult to interpret. The fragmentation could be from sampling irregularities (different measurement heights, directional sensitivity, etc.) or could be related to the actual source. The measurements are of the same area shown in Figure 5.3. Namie Town, JP Dec 2015.

Figure 5.2 and Figure 5.3 show varying degrees of success and failure in the ability to localize a hotspot in a relatively simple scene. However, they both lack sufficient data to provide confidence about the source distribution on the meter scale. The GPS resolution of Figure 5.2 shows the nonphysical intersection of very high count rate with very low count rate areas, possibly pointing to GPS limited information in this measurement. Figure 5.2 shows additional limits of GPS. Here the hotspot is correctly located but is fragmented. Here it is not clear if the fragmentations are a result of GPS resolution or measurement inconsistencies. Measurement inconsistencies can be conscious or unconscious actions by the operator. A conscious bias in the measurement is that the hotspot was very well sampled in this case, while other areas were not surveyed as intensely. Additionally, there may be measurement behaviors such as inspection of certain locations of the hotspot by placing the dose-rate meter very close to the ground, which would impact the overall shape of the hotspot. Variations in distance from the ground are in general a concern, and are both of the conscious and unconscious variety. In the end, GPS does not allow for these inconsistencies to be detected or corrected. Even for this relatively simple case, this produces results that are questionable and need more inspection to discover the true meter scale distribution of radioisotopes.

GPS has been demonstrated to be a useful tool when the resolution of interest for radioisotope mapping is much greater than the GPS resolution. On the meter scale, GPS does

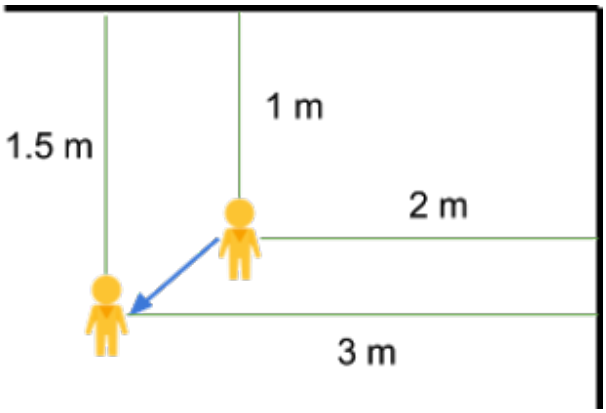

Figure 5.4: The SLAM problem as posed in the public release of Cartographer. The object of SLAM is to construct the walls and also find the position and orientation of the person relative to the first location [30]. Certain SLAM techniques provide absolute scale, as depicted.

not provide sufficient data and cannot recover measurement inconsistencies. SLAM provides a potential solution for the meter scale, providing centimeter resolution sensors for mapping technologies.

Simultaneous Localization and Mapping (SLAM)

SLAM technologies provide generation of a scene map while also providing a solution to position, orientation and/or velocity through the map. Mapping can occur in 2D or 3D, however 3D is preferred since distance modulations are so fundamental to the signal modulation at the meter scale.

3D mapping requires some way to generate scenes while making measurements. Ideally, a mapping solution would not require a pregenerated scan or map of the area and could be taken in an adhoc or flexible way. Fundamentally, SLAM relies on distance measurements of objects. Many sensors provide the ability to perform this kind of reconstruction, however not all are capable equally. In particular, a solution that is applicable for indoor and outdoor environments is preferable. LIDAR SLAM is such a solution, which provides low error distance measurements typically referred to as a scan. The Velodyne LIDAR sensor is an Avalanche Photodiode (APD) based detection system with 16 individual IR laser beams that perform time-of-flight measurement on the beam returns. The sensor has a viable range of about 100 m and can report the time-of-flight for the most intense return.

Reconstruction of the 3D scene is based on LIDAR scan-matching, a process where from scan-to-scan the orientation and location are estimated. The technique utilized in this work is based on Iterative Closest Point (ICP), a method that minimizes the difference between points seen in one scan and the next scan. The minimization discovers the 6 parameter x,y,z location and the pitch, yaw and roll of the system.

The SLAM engine used for this work was Google Cartographer [30]. This implements ICP for SLAM which we integrate for backprojection and imaging of radiation in 3D. Cartographer by default produces 2D floor maps, although the 3D data is available for export. Initially this export was done in post-processing. This solution allows us to make maps in many different kinds of environments quickly with live feedback to discover failure modes.

An example of our walking measurements is presented in Figure 5.5. The figure represents the 3D map generated by Cartographer from walking a portable LIDAR system through the scene. Figure 5.5 shows the result of our SLAM output extracted from Google Cartographer in post-processing. Not shown is our trajectory through the scene, however this data is available.

In this section we have introduced the LIDAR SLAM technique with a 3D map extracted from Google Cartographer. The output from a walking measurement was shown, however many measurement areas of interest are not accessible to humans or by walking. An example of such areas being the dense underbrush areas of the Japanese forest or even the Fukushima Dai-ici Nuclear Power Plant site. The former has accessibility issues while the latter has dose rate concerns. In the next section, we introduce an UAS to alleviate some of these concerns.

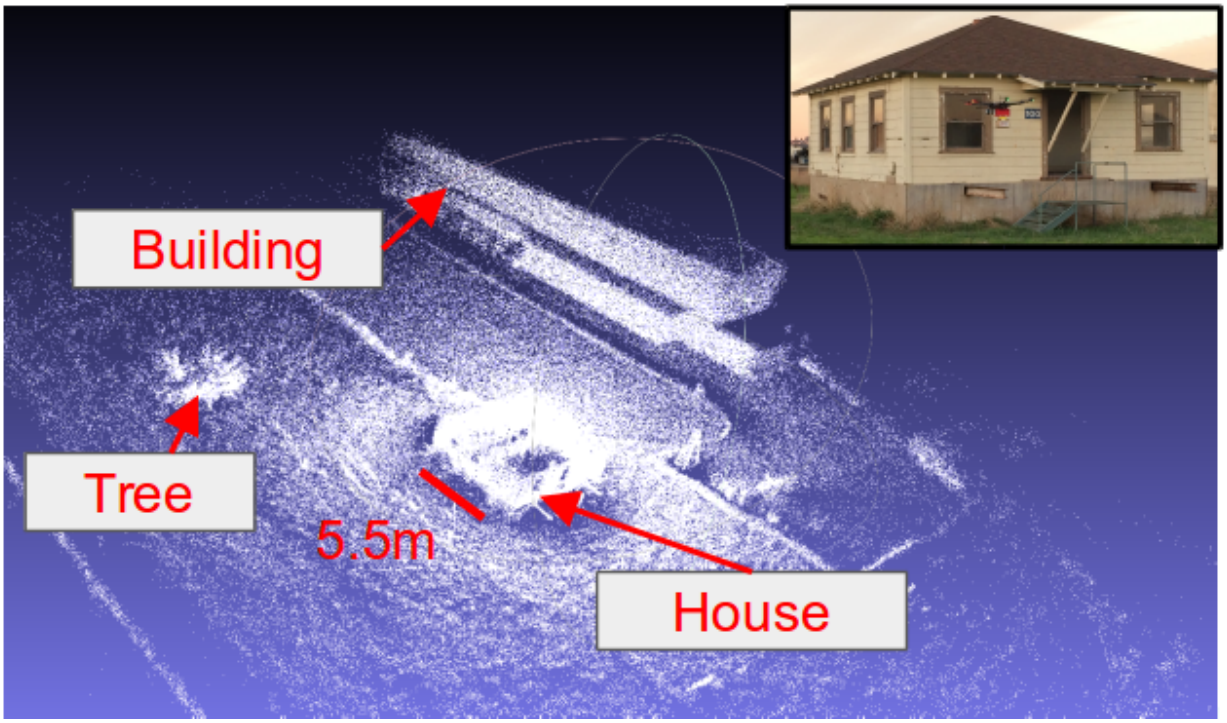

Figure 5.5: A SLAM result of an unoccupied house at the University of California Berkeley at Richmond Field Station. The inset is a photograph of the frontside of the house. The perspective of the photograph is toward the arrow point from the house label.

Unmanned Aerial System (UAS)

Autonomous vehicles have the ability to remove human risk in measurement scenarios, provide more robust mapping techniques and have the potential to make use of aggregated and regressed data in near realtime or realtime scenarios. Integration of small, powerful computer and onboard sensor suites makes these platforms especially attractive. Rich data streams make datasets which are much richer and multifaceted in use.

Specifically, we make use of a commercial UAS which is the Matrice 600. This UAS has long flight times of about 20 min with a payload of about 4 kg. Tracking of the UAS is done through an onboard GPS and IMU. These sensors integrate via a Universal Asynchronous Receiver/Transmitter (UART) bus.

Drone regulations at the current time are very restrictive in almost all areas except for private use [16]. There is a considerable amount of effort which we have placed into attempting to do flights and to meet the current requirements. This is largely due to the fact that the rules are quite new and many different regulations are in place that look similar but are very different. For example, Certificates of Waiver or Authorization (COA) use to require a private pilots license in order to operate drones commercially. The risks and challenges have been reassessed and the Federal Aviation Administration (FAA) has instituted Part 107 [15] as a way to lower the barrier-to-entry. This allows UAS operators to take a 2 hour exam on relevant parts of pilot regulation to become certified commercially. DOE however promotes their own set of policies above the FAA and adds an extra layer of uncertainty due to a lack of experience with drones. Thus, flight and measurement campaigns are limited and difficult. The University of California at the Richmond Field Station (RFS) has provided a great space for drone flights and was crucial for this work.

Localization and Mapping Platform (LAMP)

LAMP is data collection and analysis platform for different detectors and contextual sensors. The system consists of an onboard computer, IMU/GPS, global shutter camera, LIDAR and power distribution. Sensors are implemented as nodes within the open-source Robot Operating System (ROS). Within the ROS paradigm, sensors can be publishers or subscribers with the loopback interface abstracting the way in which data can be shared between nodes. Figure 5.7 displays the different sensor nodes implemented. Data can be analyzed online or saved as it is collected as ROS bags. This kind of integration allows for rapid prototyping, development and debugging of sensor nodes. The package in flight configuration has Kromek Sigma50s attached (Figure 5.6). These constitute a volume of radiation detector which is about 130 cm^3 of CsI scintillator. These are not an insignificant part of the system cost as Figure 5.9 shows in the cost distribution pie chart. Figure 5.9 details the system information at a high level. Here we attempted to integrate as much sensor mass in the system since there is a tradeoff in flight time with weight. Flexibility in implementation allows us to strike a compromise in many of the system parameters for search and localization tasks. On

the far right of Figure 5.9 There is an approximate flight time, total system mass, power consumption and battery lifetime listed for reference.

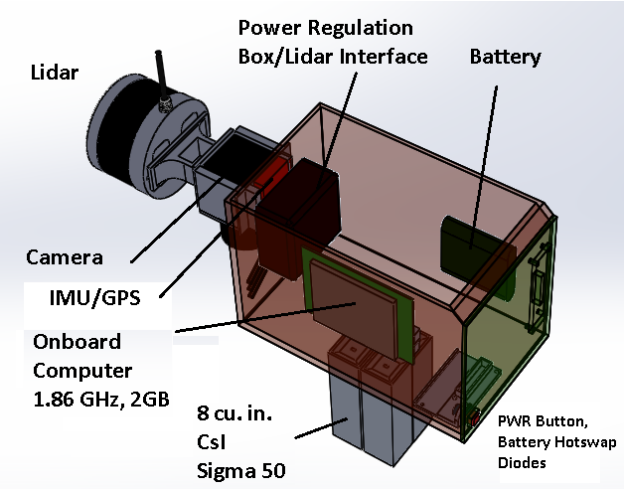

Figure 5.6: LAMP system with attached Kromek Sigma50s.

5.2 Proximity Mapping via 3D Backprojection

Proximity Mapping attempts to take advantage of source modulation due to movement of the detector system through a scene. Mapping requires that a SLAM solution is available and that radiation detector data are taken in the same measurement. Similar to the 2D mapping case, the use of monolithic detectors limits the amount of information about the interactions observed from gamma-ray interactions. However, unlike the 2D case, source intensity can be backprojected through the distance measurements and pose estimates from SLAM. Additionally, one can incorporate system asymmetries or sensitivities that improve the resulting data quality.

In order to demonstrate the concept of Proximity Mapping on a mobile SLAM system we constructed the Localization and Mapping Platform (LAMP) system. This was specifically implemented with two different kinds of CsI scintillator detector platforms, the Kromek D3S [31] and the Sigma50 [32]. The LAMP system provides flexibility in order to evaluate different detector types on a common platform.

Point Cloud Constrained Backprojection

The SLAM result is a 3D point cloud models resulting from the many LIDAR scans over the detector trajectory through a scene. The points represent objects which are opaque to IR beams that the LIDAR uses for time-of-flight distance measurements. Given that sources are constrained to IR opaque objects we compute the backprojection of data according to

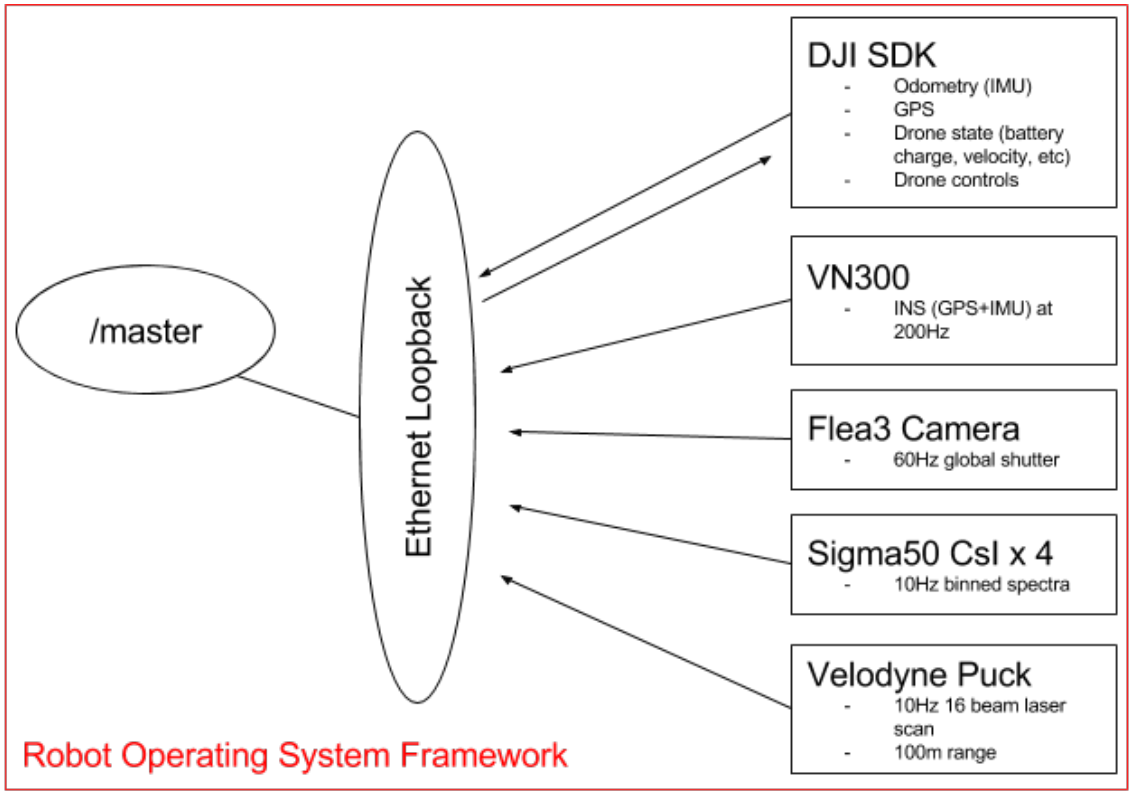

Figure 5.7: Software node graph. The sensor nodes feed the master node. Collection of all sensors operates in an adhoc fashion, where the addition or removal of an individual sensor node does not impact the system function. This allows for LAMP to provide swapping of hardware components with relative minimal effort. Here we see that each node provides data to the master node via the loopback interface. This is convenient for serialization as data packets are queued in the ethernet buffer with arrival time stamps. The master then addresses the receipt of those data packets from a FIFO buffer and can optionally save or process those elements. Additionally, nodes can connect with each other in the same way, in a naturally multithreaded fashion using TCP protocols.

Figure 5.8: LAMP system attached to the UAS. Data collection in this version has minimal feedback provided by the flight controller which can show a HDMI feed of current parameters.

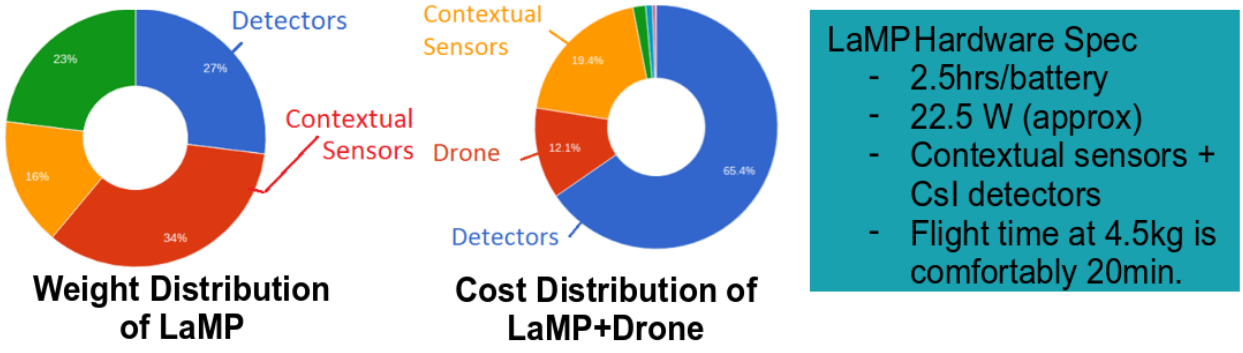

Figure 5.9: Specifications of the LAMP system when attached to the drone. By design the weight is mostly attributable to the sensors since increased payload weight decreases flight time. The cost distribution shows that LAMP is over 65 percent detector cost. Flight times, weights and power consumption are listed as well.

$B_{ij} = \frac{C_i}{4\pi R_{ij}^2}$ for each detector SLAM estimate where C_i represents the counts in each detector at position i to each point in the cloud j. The sum over i produces the backprojection, on points in the point cloud in this case. If one does not require the measurement trajectory to be tightly controlled, then points do not equally share information about the measured scene. This can be viewed abstractly as a sampling problem and is a fundamentally related to Proximity Mapping. The adhoc nature of many measurement scenarios implies that removing sampling problems is of value to reduce the number of technical constraints required to produce a result. One facet of the sampling problem is that points close to the system during the measurement produce disproportionately high estimated flux. Differences in dwell time for different locations can also bias flux estimates. Bias for these two cases is dependent on the measurement conditions, but can be partially removed by simply keeping a separate sensitivity map in each point of the point cloud computed as $S_{ij} = \frac{\Delta t_i}{4\pi R_{ij}^2}$ where Δt is the measurement time at position i. The measurement result is therefore

$$M_j = B_j / S_j, \tag{5.1}$$

where M_j is proportional to the estimated flux at each point in the 3D model. However, sensitivity of this form does not exactly solve the many problems present in reconstruction in the data. One problem is that conceivably the counts measured by the system C_i is due to a source at an unknown distance, intensity and distribution.

The sensitivity correction as presented tends to average the maximum and minimum of counts measured at each location for points that are very far away from the path measured. That is, for model points j sufficiently far from all measurement i, R_{ij} would almost be constant. In reality, the system range should be much more limited since it fundamentally relies on distance modulation, and modulation cannot occur for points far away. Another problem with sensor range is related to strong sources at a distance. These sources could contribute counts, but not be observed due to their range. For example, sources would follow $R \sim \sqrt{\phi/C}$ where ϕ, R is the source emission rate and distance from the detector. Lack of distance modulation would also be apparent in this case. For dense media attenuation effects could be incorporated in the sensitivity to reduce some range effects, however ultimately this is an open question. A solution could be to phrase the problem as a criterion for uncertainty in measured results. A possible measure is the amount of distance modulation a model point has seen. Rudimentary sensitivity based cuts are the current stand-in, which try to capture these range effects. These are arbitrary, and possibly specific to our scene but represent what is believed to be the actual range of the system. These do not affect the computation, only the plotting, and are only used as a way to communicate the range of validity of the sensor. This relatively simple technique leads to the results in Figure 5.11 from a walking measurement with the system. The detectors used were worn on a belt detached from the system in order to provide angular modulation. Here we see the detector path through the scene on a point cloud that is cut based on sensitivity. This cut is applied based on the assumption that model points with low sensitivity occur mainly in the perimeter of Figure 5.5. Two distributions become apparent when histogramming the sensitivity in this

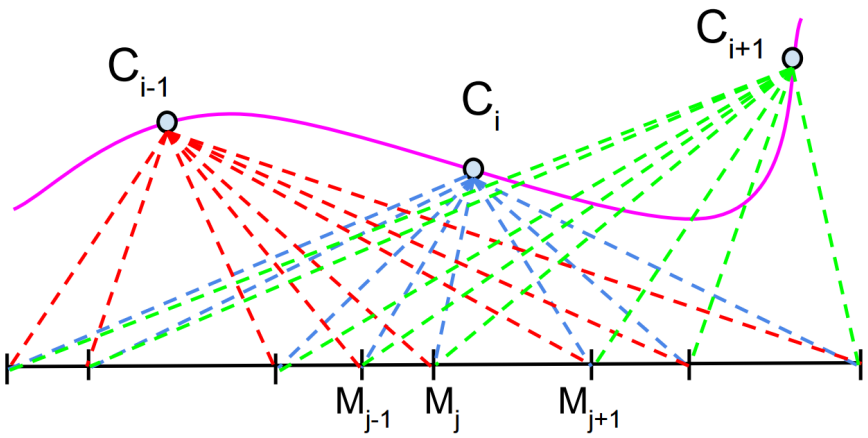

Figure 5.10: The backprojection problem. The trajectory of the detector is seen in magenta with points along the path which represent the SLAM solution for the system position. The black segmented line represents the simple scene model onto which flux estimates are projected. Each estimate of the flux M_j at the model points integrates signal from every point along the detector path. The goal is to discover a source or a distribution along the model. Sensitivity tries to remove bias toward model points which receive unequal estimates due to variations in speed and distance of approach.

case, and the cut is made on the points which form the higher sensitivity portion of the map. The backprojection occurs on all points, however those which reported low sensitivity are colored deep blue. Figure 5.11 shows a result that is interesting because the highest intensity is actually observed on a door. Here two problems exist: the readout rate of the detectors was too low (set at 1sec) and the angular response of the detectors was not accounted for. A 2D angular response was simulated in a Monte Carlo N-Particle (MCNP) calculation [44] and is plotted in Figure 5.12. The result is incorporated with the backprojection

$$\tilde{B}_{ij} = A(\hat{\mathbf{h}}_j, \hat{R}_{ij})\, B_{ij}, \tag{5.2}$$

$$\tilde{S}_{ij} = A(\hat{\mathbf{h}}_j, \hat{R}_{ij})\, S_{ij}, \tag{5.3}$$

where A is the simulated detector response function. A takes arguments $\hat{\mathbf{h}}_j$, the current heading, and the ray R_{ij}, which connects the measurement i to model point j. The function in Figure 5.12 is a 2D projection plotted in the plane of the belt the detectors are worn on. A maps the cloud point of interest into the detector frame and computes an interpolated value for the normalized angular intensity for that point.

The angular response was taken into account for generating Figure 5.2 which moves intensity from the door onto the wall near the sources. At close distances the offset between the SLAM solution and the detectors should be taken into account. In this configuration, the offset was about 10 cm from the center of the detector configuration. The readout rate

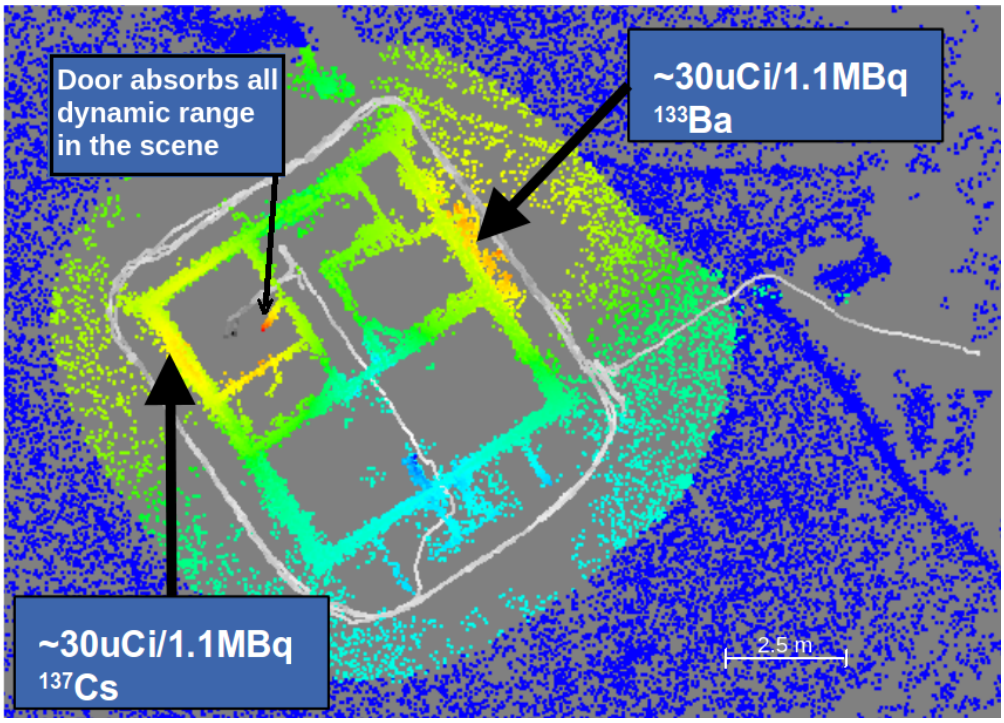

Figure 5.11: Walking data result from around a house at the University of California Berkeley Global Campus (also known as the Richmond Field Station). Paths inside and outside the house provide localization of the ^{137}Cs and ^{134}Ba source based on proximity backprojection on the point cloud. The area is cut based on the bimodal sensitivity distribution observed in the scene, around 8s/m^2. The path walked is shown in white to black in count rate intensity. Model points are colored from blue to red in backprojected counts. Areas that are deep blue are those model points beyond the estimated sensor range. The estimate of the sensor range is based on the bimodal distribution of sensitivity in the scene. The cut was applied at 8 m/s^2, after the backprojection was performed. Here we see that most of the dynamic range is absorbed by the door just inside the room containing the ^{137}Cs source.

of the detectors should not be set so low and is a defect that we are modifying in the future versions of this system.

In addition to walking scenarios, we demonstrated the ability to produce images from flight data with the drone. Figure 5.2 shows a measurement where we attempted to 0.5 mCi ^{133}Ba source which is positioned within the window of a vacant house at the University of California. Left in Figure 5.2 is the sensitivity corrected backprojection without the detector angular response. This figure has source intensity below the drone near the true source location but not on the wall of the house. The sensitivity cut of 8 s/m^2 was applied to this figure, and was seen to be a little too aggressive where a portion of the back wall is plotted deep blue. This is because the drone flew too quickly and too far away from the source to include this region. If the sensitivity cuts were altered or if more data had been collected this region would be included in the false color map.

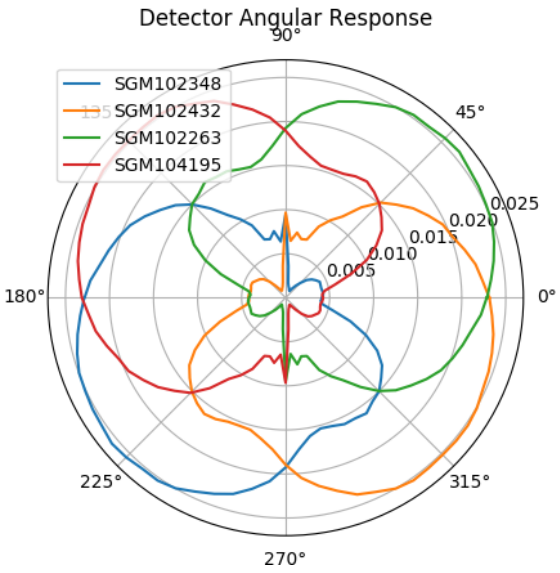

Figure 5.12: Asymmetric detector response for the different angles of gamma-ray incidence simulated in MCNP for the D3S configuration. The D3Ss are worn around the belt of an operator with some signal modulation due to the attenuation of signal through the operator and some from the finite distance between detectors. The normalized response shows the probability that a photon was incident on the system from a specific angle, given that a count was detected.

The right pane Figure 5.2 is backprojected according to Equation 5.2 and place sensitivity cuts at the same place as in the walking data at 8 s/m^2. Here there is a dark blue inclusion in the colormap where the drone flew rather quickly and farther away from the house. This is due to an aggressive sensitivity cut, which removes a portion of the house from the scene. If more data were collected or the sensitivity cut was expanded, this region would not have been cut. The results show that when doing proximity imaging, one benefits greatly from the detector response.

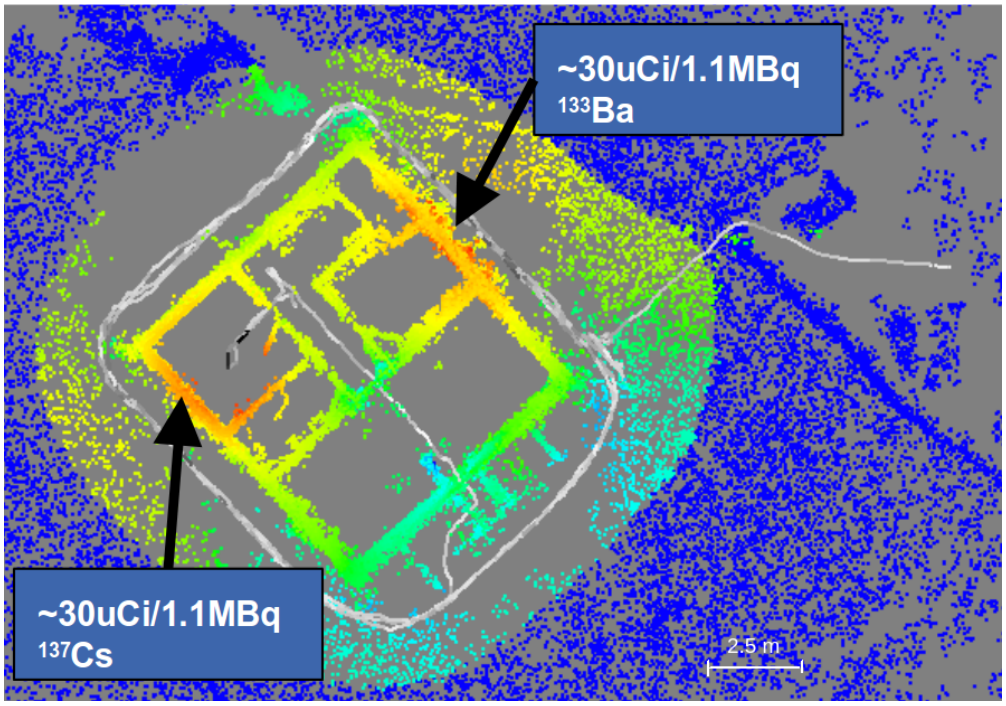

Figure 5.13: Walking data result, same as Figure 5.11 but the angular response of the detector has been incorporated in the backprojection. Here we see that the source intensity is redistributed to the walls and the localization of the ^{133}Ba is slightly better.

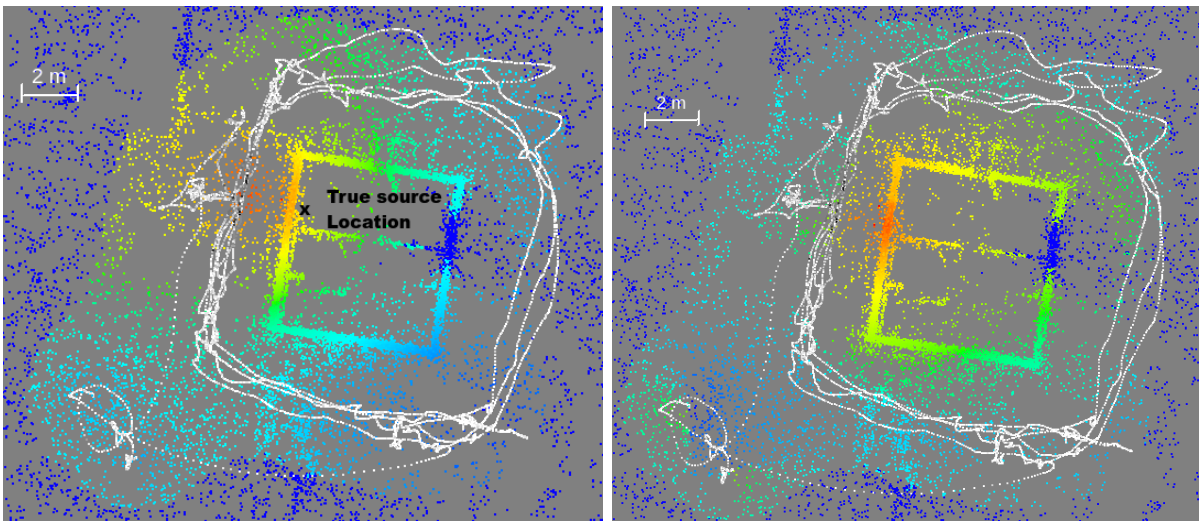

Figure 5.14: (Left) LAMP system attached to UAS system to detect a 0.5 mCi ^{133}Ba source within a house at the University of California. The detector path is shown in white while the backprojected radiation data is shown in linear intensity from blue to red. Here we can see that the system incorrectly places intensity of the source on the ground near the window where the source is located. This is due to the observation of increased count rate without inclusion of anisotropies of the detector response. Due to this points on the ground are attributed more signal than is appropriate. (Right) The detector response is taken into account for the Kromek Sigma50s by simulation of the response in the close-pack configuration. Here the wall is correctly illuminated but the source position was not captured by the LIDAR. Overall, the localization is fairly decent. Additionally, there is a deep blue region that is being cut out of the house by the sensitivity threshold, this is due to the fact that we did not spend enough time or get close enough to the back of the house as the other areas we surveyed. Again the sensitivity cuts are somewhat arbitrary, the discovery of a better representation is future work. The entire measurement lasted about 5 min.

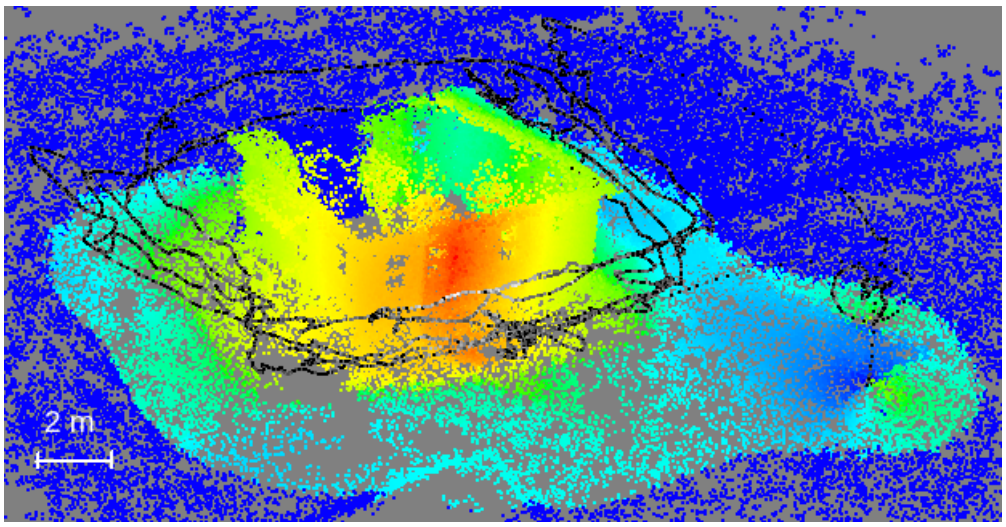

Figure 5.15: A 3D view of the house with the radiation image overlayed. The path of the drone is plotted in linear intensity from black to grey. Overall the directional response is helpful but does not reduce the source to a point. In future detector implementations it will be necessary to make sure that detector responses encode all 3D space, rather than the almost completely 2D modulations that the packing configuration of Figure 5.6 shows.

5.3 Future Directions with Autonomous Systems

The use of UAS for autonomous mapping could be more robust and data rich than current mapping efforts on the meter scale. While the demonstrations we have done are compelling, there is still much work to be done in the direction of autonomous mapping. There are technical problems outside of the field of radiation detection such as sensor development, algorithms for SLAM, object detection/avoidance, data sufficiency built in privacy/security and Artificial Intelligence (AI). AI is very broad in the current definition and implies either basic pattern recognition or very complex synergy due to the different data and algorithm inputs.

The tasks that are in the realm of radiation detection, which are somewhat near-term, are related to the inclusion of more complex imaging reconstruction techniques such as MLEM. The backprojections shown here are informative about the data collected, however do not really describe the distribution that we seek to map. These distributions represent the least amount of information that can be gleaned from the data from LAMP. Inclusion of MLEM in the proper context would attempt to provide better estimates of the distributions. The localization based on the point cloud is also very limited. If we observe gamma-ray emitters from closed objects we would not discover the true distribution, but rather simply a flux emitting surface. Voxelized MLEM could provide better estimates of simple source scenarios. In this work we have assumed that sources can only occupy objects that are observed during our measurement by the LIDAR. This constrains LAMP solutions to 2D projections and does not allow sources to appear inside volumes. For example, enclosed surfaces containing radiation sources would only have model points corresponding to the volume surface. Volumetric imaging has been explored in depth by [3] and would be of interest for future development. Material identification will be important for all nontrivial voxelized spaces.

Harder and longer-term tasks in radiation detection are related in some ways specially to data sufficiency. This is again a very broad subject in consideration of the arbitrary scenarios that might be present in radiation mapping. Data sufficiency would at least partially seek to answer:

- How much time or spatial sampling should be done over a given scene to state a certain level of confidence in the mapped measurement result?
- Given a mapped area, to what level of confidence is there no unidentified source of a given size?
- How uncertain is a particular area that has been mapped?/How much more investigation should be done in order to state confidence in a mapped distribution?

Providing algorithms to the data sufficiency questions is not simple, however these would allow autonomous systems to make decisions about scenes in order to map appropriately. It is likely that the answers to these questions will involve other sensors which provide material

property estimates. At the current state of our research, we simply provide these estimates based on the observed scene and the distribution of sensitivities.

Chapter 6

Summary

In this work, we have explored Gamma-Ray Mapping in the context of very complex ETCI detectors as well as the relatively simple scintillating spectrometers augmented with contextual sensors. The evolution of Gamma-Ray Mapping has followed technology developments in semiconductor physics and in the availability of supplemental sensors. Fundamentally, Gamma-Ray Imaging has evolved into Gamma-Ray Mapping applications because of these developments. Drivers for change have been the available data that sensors provide and the ability to simultaneously localize the system while mapping. Gamma-Ray Mapping stands to do change the way radiation measurements are done, for localization of point sources and distributions. The rich datasets that are produced which are multifaceted in use. We continue to explore their usefulness in autonomous systems.

Specifically, we point out the utility of Gamma-Ray Mapping in environmental decontamination efforts, such as those that are currently ongoing at the FDNPPA site and Japanese countryside. The flexibility of the LAMP, being able to host many different detector technologies, is a excellent demonstration platform for different kinds of Gamma-Ray Imagers. The technology developments necessary for ETCI continues as a pursuit of the limits of kinematic information in Compton Imaging. Provided significant and nontrivial improvements, ETCI would be a very attractive Compton Imager to merge in the LAMP system for Gamma-Ray Mapping.

In this chapter, we focus on our efforts to facilitate the growth of Gamma-Ray Mapping and the future possibilities for its continuing evolution.

ETCI

Progress toward Electron Track Compton Imagers (ETCI) has shown that improved physical information about the Compton scattering process can increase the efficiency of detector systems, open new imaging modes and even make progress toward event-by-event gamma-ray momentum calculations. We have presented the benchmarking of simulations in both the energy and spatial domains of the electron tracks produced in CCD based electron trackers. We have noted that those simulations provide insights to event types which could improve

data quality by providing the Compton electron data down to the 1-10μm scale. Additionally, we have shown how this data allows for the validation of novel imaging modalities. In particular, our benchmarked simulation data helped in the electron only analytic inversion [19] which provides a recovery of both the source location in angular space and the incident photon energy.

A cornerstone of the ETCI work has been in the development of CCD-Strip. The recognition of problems associated with CCD based electron tracking and a proposed fix were discussed and investigated. A batch of CCD-Strip devices were fabricated and tested in the LBNL engineering test stand. Additionally, we constructed and demonstrated the newly fabricated devices in a custom test stand. The DALSA control wafers to first to produce electron tracks was characterized. The first electron tracks from CCD-Strip were also observed in our setup. Strip-pixel registration by use of a small LED pulse of light showed good alignment of the strips. Registration of this kind would be useful in future characterizations. The test stand allowed us to reduce the leakage current in CCD-Strip by a factor of 1000. This reduction removed large transients on strips of approximately 3-5 MeV of equivalent charge, but ultimately left the system at about 400 keV-RMS-ENC per strip. The strip operation is yet to be demonstrated, and we have proposed system modifications to ameliorate noise issues on the strips.

We recognize that many other technologies have become available since CCD-Strip was proposed and fabricated. Active pixel technologies widely vary in relevant parameter spaces and the increased channel density will provide much work in the future.

However, we also see that simulations can very much inform the design of these new electron tracking systems. Interestingly, the nuclear scatter limit is of vital importance to electron trackers. Simulation results show that for a large number of materials the fraction of energy going to electronic excitation early in the electron track is proportional to 1/Z. Thus electron trackers using high Z materials must be careful to monitor the amount of signal per channel otherwise the early electron track information may not be recoverable. We also identified diamond as perhaps one of the best electron tracking materials for recovery of the initial electron trajectory.

LAMP

The Localization and Mapping Platform (LAMP) has shown that there is utility in coupling contextual sensors to augment relatively simple commercial radiation detectors. These observations are of vital importance as they represent the lower end of cost and complexity for Gamma-Ray Mapping. We have shown that meter-scale mapping really benefits from high resolution position tracking and that GPS methods are often not sufficient.

We designed and demonstrated the use of LAMP for proximity imaging with two different detector sets in handheld and UAS operation. Of critical importance is the detector characterization, which improves the localization of point sources significantly in our cases. Notably, we are missing MLEM implementations for our work and note that this could benefit our data greatly. This represents one of the many tasks in future work.

Mapping complex distributions was not discussed in this work although it is ultimately a goal of many of our systems. We are pursuing these efforts in the future. Specifically, FDNPPA decontamination and decommissioning present many challenges which LAMP could help to address, and LAMP could be customized to fit those applications. High count rate, embedded and extended source distributions, and the possibility for incorporation of autonomous vehicles present many interesting challenges and opportunities, and the FDNPPA clean up has need for useful solutions.

Ultimately, LAMP will serve as a demonstration platform integrating many different kinds of sensors and a variety of radiation detectors. Integration of more complex imaging detectors that are light enough for flight is of interest. Platforms of this kind are incredibly useful for fair comparison and differential improvements. These also form a base layer similar to the computer abstraction layer in Computer Science, where algorithmic improvements can be demonstrated and implemented. This is key to the future of research, especially in fields where hardware is expensive, unique or difficult to integrate. Lowering the barrier to entry allows algorithms to be developed at a much higher speed and the implementations can be carried forward in a usable and modifiable form.

Larger Context and Future Outlook

The technologies we have presented fit in the larger picture as particularly well suited solutions to Gamma-Ray Mapping for astrophysical distributions and to nuclear contamination. For the case of astrophysical mapping, advanced Compton Imagers can provide more information about the spectrum of gamma-rays emitted from distant objects. ETCI Imagers could eventually improve the sensitivity or range of the insights that these instruments provide. Additionally, the eventual realization of ETCI systems could augment LAMP to provide better use of incident gamma-ray flux.

In the specific case of contamination mapping, we noted that these advancements could be significant improvements over handheld dose-rate measurements in Fukushima Dai-ichi during decontamination and decommissioning. As we have presented, the current tool of choice is labor intensive and requires human operators (Figure 1.4). Future Gamma-Ray Mapping technology developments could improve the localization of contamination, the discovery and verification of suspected hotspots. The records that LAMP keeps are also potentially useful as maps of areas that have not been re-entered by humans for some time. Inclusion of UAS and AI in future robotic systems could remove human risk from the measurement planning scenario. Development of robotic systems with these capabilities will become important for the Fukushima Dai-ichi decommissioning projections. The Japanese Ministry of Economy, Trade and Industry (METI) has released estimates of 2-8 trillion yen (18-70 billion USD). The projection has quadrupled since 2013 [40]. Ultimately, education of the public of the benefits and risks associated with nuclear technologies needs large investment from society and good educators; technology investment is not equivalent. The widening scope of decontamination efforts provides a substantial challenge for people doing the work and stakeholders, decisions that are made could better and benefit from Gamma-Ray Mapping.

Bibliography

[1] S. Agostinelli, J. Allison, K. Amako, J. Apostolakis, H. Araujo, P. Arce, M. Asai, D. Axen, S. Banerjee, G. Barrand, F. Behner, L. Bellagamba, J. Boudreau, L. Broglia, A. Brunengo, H. Burkhardt, S. Chauvie, J. Chuma, R. Chytracek, G. Cooperman, G. Cosmo, P. Degtyarenko, A. Dell'Acqua, G. Depaola, D. Dietrich, R. Enami, A. Feliciello, C. Ferguson, H. Fesefeldt, G. Folger, F. Foppiano, A. Forti, S. Garelli, S. Giani, R. Giannitrapani, D. Gibin, J.J. Gmez Cadenas, I. Gonzlez, G. Gracia Abril, G. Greeniaus, W. Greiner, V. Grichine, A. Grossheim, S. Guatelli, P. Gumplinger, R. Hamatsu, K. Hashimoto, H. Hasui, A. Heikkinen, A. Howard, V. Ivanchenko, A. Johnson, F.W. Jones, J. Kallenbach, N. Kanaya, M. Kawabata, Y. Kawabata, M. Kawaguti, S. Kelner, P. Kent, A. Kimura, T. Kodama, R. Kokoulin, M. Kossov, H. Kurashige, E. Lamanna, T. Lampn, V. Lara, V. Lefebure, F. Lei, M. Liendl, W. Lockman, F. Longo, S. Magni, M. Maire, E. Medernach, K. Minamimoto, P. Mora de Freitas, Y. Morita, K. Murakami, M. Nagamatu, R. Nartallo, P. Nieminen, T. Nishimura, K. Ohtsubo, M. Okamura, S. O'Neale, Y. Oohata, K. Paech, J. Perl, A. Pfeiffer, M.G. Pia, F. Ranjard, A. Rybin, S. Sadilov, E. Di Salvo, G. Santin, T. Sasaki, N. Savvas, Y. Sawada, S. Scherer, S. Sei, V. Sirotenko, D. Smith, N. Starkov, H. Stoecker, J. Sulkimo, M. Takahata, S. Tanaka, E. Tcherniaev, E. Safai Tehrani, M. Tropeano, P. Truscott, H. Uno, L. Urban, P. Urban, M. Verderi, A. Walkden, W. Wander, H. Weber, J.P. Wellisch, T. Wenaus, D.C. Williams, D. Wright, T. Yamada, H. Yoshida, and D. Zschiesche. Geant4a simulation toolkit. *Nuclear Instruments and Methods in Physics Research Section A: Accelerators, Spectrometers, Detectors and Associated Equipment*, 506(3):250 – 303, 2003.

[2] Y. Arai, T. Miyoshi, Y. Unno, T. Tsuboyama, S. Terada, Y. Ikegami, R. Ichimiya, T. Kohriki, K. Tauchi, Y. Ikemoto, Y. Fujita, T. Uchida, K. Hara, H. Miyake, M. Kochiyama, T. Sega, K. Hanagaki, M. Hirose, J. Uchida, Y. Onuki, Y. Horii, H. Yamamoto, T. Tsuru, H. Matsumoto, S.G. Ryu, R. Takashima, A. Takeda, H. Ikeda, D. Kobayashi, T. Wada, H. Nagata, T. Hatsui, T. Kudo, A. Taketani, T. Kameshima, T. Hirono, M. Yabashi, Y. Furukawa, M. Battaglia, P. Denes, C. Vu, D. Contarato, P. Giubilato, T.S. Kim, M. Ohno, K. Fukuda, I. Kurachi, M. Okihara, N. Kuriyama, and M. Motoyoshi. Development of soi pixel process technology. *Nuclear Instruments and Methods in Physics Research Section A: Accelerators, Spectrometers, Detectors and Associated Equipment*, 636(1):S31 – S36, 2011. 7th International Hiroshima Symposium on the Development and Application of Semiconductor Tracking Detectors.

[3] Ross Barnowski, Andrew Haefner, Lucian Mihailescu, and Kai Vetter. Scene data fusion: Real-time standoff volumetric gamma-ray imaging. *Nuclear Instruments and Methods in Physics Research Section A: Accelerators, Spectrometers, Detectors and Associated Equipment*, 800:65 – 69, 2015.

[4] P. J. Barton, D. Chivers, C. S. Tindall, S. E. Holland, T. E. Hansen, and K. Vetter. Fabrication of a hybrid silicon ccd-strip detector for electron tracking based compton imager, 2010. IEEE Nuclear Science Symposium.

[5] M.J. Berger, J.S. Coursey, M.A. Zucker, and J. Chang. Estar, pstar, and astar: Computer programs for calculating stopping-power and range tables for electrons, protons, and helium ions (version 1.2.3). `http://physics.nist.gov/Star`. National Institute of Standards and Technology, Gaithersburg, MD., 2005. Accessed: 2017-7-28.

[6] M.J. Berger, J.H. Hubbell, S.M. Seltzer, J. Chang, J.S. Coursey, R. Sukumar, D.S. Zucker, and K. Olsen. Xcom: Photon cross section database (version 1.5). `http://physics.nist.gov/xcom`, 2010. Accessed: 2017-7-28.

[7] N. Roe C. Bebek. *4k x 2k and 4k x 4k CCD Users Manual*. Lawrence Berkeley Lab, 2011.

[8] J.-L. Chiu, S.E. Boggs, H.-K. Chang, J.A. Tomsick, A. Zoglauer, M. Amman, Y.-H. Chang, Y. Chou, P. Jean, C. Kierans, C.-H. Lin, A. Lowell, J.-R. Shang, C.-H. Tseng, P. von Ballmoos, and C.-Y. Yang. The upcoming balloon campaign of the compton spectrometer and imager (cosi). *Nuclear Instruments and Methods in Physics Research Section A: Accelerators, Spectrometers, Detectors and Associated Equipment*, 784:359 – 363, 2015. Symposium on Radiation Measurements and Applications 2014 (SORMA XV).

[9] Youjing Cui and Shuzhi Sam Ge. Autonomous vehicle positioning with gps in urban canyon environments. *IEEE Transactions on Robotics and Automation*, 19(1):15–25, Feb 2003.

[10] P Denes, D Doering, HA Padmore, J-P Walder, and J Weizeorick. A fast, direct x-ray detection charge-coupled device. *Review of Scientific Instruments*, 80(8):083302, 2009.

[11] Chris DiBona, Sam Ockman, and Mark Stone. *Open sources. [electronic resource] : voices from the open source revolution.* Beijing ; Sebastopol, CA : O'Reilly, c1999, 1999.

[12] R Diehl, C Dupraz, K Bennett, H Bloemen, W Hermsen, J Knoedlseder, G Lichti, D Morris, J Ryan, V Schoenfelder, et al. Comptel observations of galactic^ 26^ al emission. *Astronomy and Astrophysics*, 298:445, 1995.

[13] TR England and BF Rider. Evaluation and compilation of fission product yields. *ENDF-349, LA-UR-94-3106, Los Alamos National Laboratory*, 1994.

[14] Robley Evans. *The Atomic Nucleus*. McGraw Hill Book Company, Inc., New York, NY, USA, 1955.

[15] FAA. 14 cfr part 107. https://www.ecfr.gov/cgi-bin/text-idx?SID=e331c2fe611df1717386d29eee38b000&mc=true&node=pt14.2.107&rgn=div5. Accessed:2017-7-25.

[16] FAA. Certificates of waiver or authorization (coa). https://www.faa.gov/about/office_org/headquarters_offices/ato/service_units/systemops/aaim/organizations/uas/coa/. Accessed:2017-7-25.

[17] L. Fabris, N.W. Madden, and H. Yaver. A fast, compact solution for low noise charge preamplifiers1. *Nuclear Instruments and Methods in Physics Research Section A: Accelerators, Spectrometers, Detectors and Associated Equipment*, 424(23):545 – 551, 1999.

[18] The Geant4 Low Energy Electromagnetic Physics Working Group. https://twiki.cern.ch/twiki/bin/view/Geant4/LoweMigratedLivermore, 2014. Accessed: 2017-8-1.

[19] A Haefner, D Gunter, B Plimley, R Pavlovsky, and K Vetter. Gamma-ray momentum reconstruction from compton electron trajectories by filtered back-projection. *Applied Physics Letters*, 105(18):184101, 2014.

[20] Andrew Haefner, Ross Barnowski, Paul Luke, Mark Amman, and Kai Vetter. Handheld real-time volumetric 3-d gamma-ray imaging. *Nuclear Instruments and Methods in Physics Research Section A: Accelerators, Spectrometers, Detectors and Associated Equipment*, 857:42 – 49, 2017.

[21] S. E. Holland, C. J. Bebek, K. S. Dawson, J. H. Emes, M. H. Fabricius, J. A. Fairfield, D. E. Groom, A. Karcher, W. F. Kolbe, N. P. Palaio, N. A. Roe, and G. Wang. High-voltage-compatable, fully depleted ccds, 2006.

[22] Stephen E Holland, Chris J Bebek, Kyle S Dawson, JH Emes, Max H Fabricius, Jessaym A Fairfield, Don E Groom, A Karcher, William F Kolbe, Nick P Palaio, et al. High-voltage-compatible, fully depleted ccds. In *Proc. SPIE*, volume 6276, page 62760B, 2006.

[23] Steve Holland. Fabrication of detectors and transistors on high-resistivity silicon. *Nuclear Instruments and Methods in Physics Research Section A: Accelerators, Spectrometers, Detectors and Associated Equipment*, 275(3):537–541, 1989.

[24] Steve Holland. Fully depleted thick ccds. http://www.slac.stanford.edu/econf/C0604032/talks/snic_holland.pdf, 2006. Accessed:2017-7-25.

[25] Steve Holland and Paul Barton. Ccd-strip screening at lbnl test stand. Private Communication.

[26] P. Horowitz and W. Hill. *The Art of Electronics*. Cambridge University Press, New York, NY, USA, 1989.

[27] S. B. Howell. *Handbook of CCD Astronomy*. Cambridge University Press, April 2000.

[28] Chenming Calvin Hu. *Modern Semiconductor Devices for Integrated Circuits*. Pearson, 2009.

[29] Ming-Huey A Huang, Mark Amman, Mark E Bandstra, Eric Bellm, Steven E Boggs, Jason D Bowen, Hsiang-Kuang Chang, Yuan-Hann Chang, Shueng-Jung Chiang, Jeng-Lun Chiu, et al. The nuclear compton telescope (nct): a status report after 2009 balloon flight. *Proceedings of 31st ICRC*, 2009.

[30] Google Inc. Introducing cartographer. `https://opensource.googleblog.com/2016/10/introducing-cartographer.html`. Accessed: 2017-5-12.

[31] Kromek Inc. D3s. `http://www.kromek.com/index.php/link-3/d3s`. Accessed:2017-7-25.

[32] Kromek Inc. Sigma-50 and sigma-25. `http://www.kromek.com/index.php/products/applications/research/sigma`. Accessed:2017-7-25.

[33] James Janesick, Tom Elliott, Stewart Collins, Taher Daud, Dave Campbell, Arsham Dingizian, and Gordon Garmire. Ccd advances for x-ray scientific measurements in 1985. *Proc. SPIE*, 0597:364–380, 1986.

[34] J.R. Janesick. *Scientific Charge-coupled Devices*. Press Monograph Series. Society of Photo Optical, 2001.

[35] F. Januschek, I. Klackova, N. Andresen, P. Denes, S. Hauf, J. Joseph, M. Kuster, and C. Tindall. Performance of the LBNL FastCCD for the European XFEL. *ArXiv e-prints*, December 2016.

[36] Claude A. Klein. Bandgap dependence and related features of radiation ionization energies in semiconductors. *Journal of Applied Physics*, 39(4):2029–2038, 1968.

[37] Glenn F Knoll. *Radiation detection and measurement*. John Wiley & Sons, 2010.

[38] Nobelprize.org. The nobel prize in physics 2009. `https://www.nobelprize.org/nobel_prizes/physics/laureates/2009/`. Accessed: 2017-5-8.

[39] Nobelprize.org. The nobel prize in physics 2011. `https://www.nobelprize.org/nobel_prizes/physics/laureates/2011/`. Accessed: 2017-5-8.

[40] Y Obayashi and K Hamada. Japan nearly doubles fukushima disaster-related cost to 188 billion dollars. *Reuters*, 2016. Accessed: 2017-5-12.

[41] World Health Organization et al. *Health risk assessment from the nuclear accident after the 2011 Great East Japan earthquake and tsunami, based on a preliminary dose estimation*. World Health Organization, 2013.

[42] G. G. Pavlov and J. A. Nousek. Charge diffusion in CCD X-ray detectors. *Nuclear Instruments and Methods in Physics Research A*, 428:348–366, June 1999.

[43] B. C. Plimley. *Electron Trajectory Reconstruction for Advanced Compton Imaging of Gamma Rays*. PhD thesis, University of California, Berkeley, 2014.

[44] B. Quiter. Mcnp simulation of d3s detector angular response. Private Communication, 2016.

[45] Veljko Radeka. Low-noise techniques in detectors. *Annual Review of Nuclear and Particle Science*, 38(1):217–277, 1988.

[46] S. Ramo. Currents induced by electron motion. *Proceedings of the IRE*, 27(9):584–585, Sept 1939.

[47] N.A. Roe, C.J. Bebek, K.S. Dawson, J.H. Emes, M.H. Fabricius, J.A. Fairfield, D.E. Groom, S.E. Holland, A. Karcher, W.F. Kolbe, N.P. Palaio, and G. Wang. Radiation-tolerant, red-sensitive ccds for dark energy investigations. *Nuclear Instruments and Methods in Physics Research Section A: Accelerators, Spectrometers, Detectors and Associated Equipment*, 572(1):526 – 527, 2007. Frontier Detectors for Frontier Physics.

[48] Albert Y. Shih, Robert P. Lin, Gordon J. Hurford, Nicole A. Duncan, Pascal Saint-Hilaire, Hazel M. Bain, Steven E. Boggs, Andreas C. Zoglauer, David M. Smith, Hiroyasu Tajima, Mark S. Amman, and Tadayuki Takahashi. The gamma-ray imager/polarimeter for solar flares (grips), 2012.

[49] SINTEF. Sintef ccd-strip internal report. Private Communication.

[50] Helmuth Spieler. *Semiconductor detector systems*, volume 12. Oxford university press, 2005.

[51] Hui Tian and Abbas El Gamal. Analysis of 1/f noise in cmos aps. In *Electronic Imaging*, pages 168–176. International Society for Optics and Photonics, 2000.

[52] Tatsuo Torii, Takeshi Sugita, Colin Okada, Michael Reed, and Daniel J Blumenthal. Enhanced analysis methods to derive the spatial distribution of 131i deposition on the ground by airborne surveys at an early stage after the fukushima daiichi nuclear power plant accident, 2013.

[53] Linus Torvalds, Junio Hamano, and many others. git –fast-version-control. https://git-scm.com/, Original release: 2005-4-7. Accessed:2017-7-25.

[54] T. Tsuru, H. Matsumura, A. Takeda, T. Tanaka, S. Nakashima, Y. Arai, K. Mori, R. Takenaka, Y. Nishioka, T. Kohmura, T. Hatsui, T. Kameshima, K. Ozaki, Y. Kohmura, T. Wagai, D. Takei, S. Kawahito, K. Kagawa, K. Yasutomi, and H. Kamehama. Development and performance of Kyoto's x-ray astronomical SOI pixel (SOIPIX) sensor. In *Space Telescopes and Instrumentation 2014: Ultraviolet to Gamma Ray*, volume 9144 of , page 914412, aug 2014.

[55] US Air Force United States Government. Gps accuracy. `http://www.gps.gov/systems/gps/performance/accuracy/`. Accessed:2017-5-12.

[56] J Valentine. Labzy nanomca. `http://www.labzy.com/index.html`. Accessed: 2017-5-8.

[57] J. D. Valentine, B. D. Rooney, and J. Li. The light yield nonproportionality component of scintillator energy resolution. *IEEE Transactions on Nuclear Science*, 45(3):512–517, Jun 1998.

[58] VectorNav. Vectornav300 specifications. `http://www.vectornav.com/products/vn-300/specifications`. Accessed:2017-5-12.

[59] K. Vetter, M. Burks, C. Cork, M. Cunningham, D. Chivers, E. Hull, T. Krings, H. Manini, L. Mihailescu, K. Nelson, D. Protic, J. Valentine, and D. Wright. High-sensitivity compton imaging with position-sensitive si and ge detectors. *Nuclear Instruments and Methods in Physics Research Section A: Accelerators, Spectrometers, Detectors and Associated Equipment*, 579(1):363 – 366, 2007. Proceedings of the 11th Symposium on Radiation Measurements and Applications.

[60] K. Vetter, D. Chivers, B. Plimley, A. Coffer, T. Aucott, and Q. Looker. First demonstration of electron-tracking based compton imaging in solid-state detectors. *Nuclear Instruments and Methods in Physics Research Section A: Accelerators, Spectrometers, Detectors and Associated Equipment*, 652(1):599 – 601, 2011. Symposium on Radiation Measurements and Applications SORMA XII 2010.

[61] S. J. Wilderman, N. H. Clinthorne, J. A. Fessler, and W. Les Rogers. List-mode maximum likelihood reconstruction of compton scatter camera images in nuclear medicine. *Nuclear Science Symposium*, 1998.